Università
degli Studi
di Padova

Sede Amministrativa: Università degli Studi di Padova
Dipartimento di Ingegneria Civile, Edile ed Ambientale

SCUOLA DI DOTTORATO DI RICERCA IN:
SCIENZE DELL'INGEGNERIA CIVILE E AMBIENTALE
XXIX CICLO

MATHEMATICAL MODELING OF AVASCULAR TUMOR GROWTH

Direttore della Scuola: Prof. Stefano Lanzoni
Supervisori: Prof. Daniela Boso
Prof. Bernhard Schrefler
Revisori Esterni: Prof. Anna Pandolfi
Prof. Davide Ambrosi

Dottorando: Pietro Mascheroni

This doctoral thesis has been approved as follows:

Prof. Stefano Lanzoni .....
Director of the PhD school

Prof. Daniela Boso .....
Thesis supervisor

Prof. Bernhard Schrefler .....
Thesis supervisor

Pietro Mascheroni .....
PhD candidate

"Human beings do not live forever, Reuven. We live less than the time it takes to blink an eye, if we measure our lives against eternity. So it may be asked what value is there to a human life. There is so much pain in the world. What does it mean to have to suffer so much, if our lives are nothing more than the blink of an eye?... I learned a long time ago, Reuven, that a blink of an eye in itself is nothing; but the eye that blinks, that is something. A span of life is nothing; but the man who lives the span, he is something. He can fill that tiny span with meaning, so its quality is immeasurable though its quantity may be insignificant. A man must fill his life with meaning, meaning is not automatically given to life. It is hard work to fill one's life with meaning- that, I do not think you understand yet. A life filled with meaning is worthy of rest. I want to be worthy of rest when I am no longer here."

Chaim Potok, *The Chosen*, 1967

Abstract

Cancer is an extremely complex disease, both in terms of its causes and consequences to the body. Cancer cells acquire the ability to proliferate without control, invade the surrounding tissues and eventually form metastases. It is becoming increasingly clear that a description of tumors that is uniquely based on molecular biology is not enough to understand thoroughly this illness. Quantitative sciences, such as physics, mathematics and engineering, can provide a valuable contribution to this field, suggesting new ways to examine the growth of the tumor and to investigate its interaction with the neighboring environment. In this dissertation, we deal with mathematical models for avascular tumor growth. We evaluate the effects of physiological parameters on tumor development, with a particular focus on the mechanical response of the tissue.

We start from tumor spheroids, an effective three-dimensional cell culture, to investigate the first stages of tumor growth. These cell aggregates reproduce the nutrient and proliferation gradients found in the early stages of cancer and can be grown with a strict control of their environmental conditions. The equations of the model are derived in the framework of porous media theory, and constitutive relations for the mass transfer terms and the mechanical stress are formulated on the basis of experimental observations. The growth curves of the model are compared to the experimental data, with good agreement for the different experimental settings. A new mathematical law regulating the inhibitory effect of mechanical compression on cancer cell proliferation is also presented. Then, we perform a parametric analysis to identify the key parameters that drive the system response. We conclude this part by introducing governing equations for transport and uptake of a chemotherapeutic agent, designed to target cell proliferation. In particular, we investigate the combined effect of compressive stresses and drug action. Interestingly, we find that variation in

tumor spheroid volume, due to the presence of a drug targeting cell proliferation, depends considerably on the compressive stress level of the cell aggregate.

In the second part of the dissertation, we study a constitutive law describing the mechanical response of biological tissues. We introduce this relation in a biphasic model for tumor growth based on the mechanics of fluid-saturated porous media. The internal reorganization of the tissue in response to mechanical and chemical stimuli is described by enforcing the multiplicative decomposition of the deformation gradient tensor associated with the solid phase motion. In this way, we are able to distinguish the contributions of growth, rearrangement of cellular bonds, and elastic distortion, occurring during tumor evolution. Results are presented for a benchmark case and for three biological configurations. We analyze the dependence of tumor development on the mechanical environment, with particular focus on cell reorganization and its role in stress relaxation.

Finally, we conclude with a summary of the results and with a discussion of possible future extensions.

Sommario

Il cancro è una malattia estremamente complessa, sia per quanto riguarda le sue cause che per i suoi effetti sul corpo. Le cellule del cancro acquisiscono la capacità di proliferare senza controllo, invadere i tessuti vicini e infine sviluppare metastasi. Negli ultimi anni sta diventando sempre più chiaro che una descrizione dei tumori basata unicamente sulla biologia molecolare non può essere sufficiente per comprendere interamente la malattia. A questo riguardo, scienze quantitative come la Fisica, la Matematica e l'Ingegneria, possono fornire un valido contributo, suggerendo nuovi modi per esaminare la crescita di un tumore e studiare la sua interazione con l'ambiente circostante. In questa tesi ci occupiamo di modelli matematici per la crescita avascolare dei tumori. Valutiamo gli effetti dei parametri fisiologici sullo sviluppo del tumore, con un'attenzione particolare alla risposta meccanica del tessuto.

Partiamo dagli sferoidi tumorali, una cultura cellulare tridimensionale, per studiare le prime fasi della crescita tumorale. Questi aggregati cellulari sono in grado di riprodurre i gradienti di nutriente e proliferazione che si ritrovano nei tumori avascolari. Inoltre, possono essere fatti crescere con un controllo molto severo delle condizioni ambientali. Le equazioni del modello sono derivate nell'ambito della teoria dei mezzi porosi dove, per chiudere il problema, definiamo opportune relazioni costitutive al fine di descrivere gli scambi di massa tra i diversi componenti del sistema e la risposta meccanica di quest'ultimo. Tali leggi sono formulate sulla base di osservazioni sperimentali. Le curve di crescita del modello sono quindi confrontate con dati sperimentali, con un buon accordo per le diverse condizioni. Presentiamo, inoltre, una nuova espressione matematica per descrivere gli effetti di inibizione della crescita da parte della compressione meccanica sulle cellule cancerose. In seguito, eseguiamo uno studio parametrico per identificare i parametri chiave che guidano la risposta del sistema. Concludiamo infine questa parte introducendo le equazioni di

governo per il trasporto e il consumo di un agente chemioterapico, studiato per essere efficace sulle cellule proliferanti. In particolare, consideriamo l'effetto combinato di stress meccanici compressivi e di tale farmaco sullo sviluppo del tumore. A questo proposito, i nostri risultati indicano che una variazione di volume degli sferoidi tumorali, a causa dell'azione del farmaco, dipende sensibilmente dal livello di tensione a cui è sottoposto l'aggregato cellulare.

Nella seconda parte di questa trattazione, studiamo una legge costitutiva per descrivere la risposta meccanica di tessuti biologici. Introduciamo questa relazione in un modello bifasico per la crescita tumorale basato sulla meccanica di mezzi porosi saturi. La riorganizzazione interna del tessuto in risposta a stimoli meccanici e chimici è descritta attraverso la decomposizione moltiplicativa del gradiente di deformazione associato con il moto della fase solida del sistema. In questo modo, risulta possibile distinguere i contributi di crescita, riarrangiamento dei legami cellulari e distorsione elastica che prendono luogo durante l'evoluzione del tumore. In seguito, presentiamo risultati per un caso di test e per tre configurazioni di interesse biologico. In particolare, analizziamo la dipendenza dello sviluppo del tumore dal suo ambiente meccanico, con un'attenzione particolare sulla riorganizzazione dei legami tra le cellule e il suo ruolo sul rilassamento degli stress meccanici.

Infine, concludiamo la discussione con un breve riassunto dei risultati ottenuti e un resoconto dei possibili sviluppi.

Contents

List of Figures

List of Tables

Chapter 1

Motivation and thesis layout

1.1 Introduction

Cancer is the name that is currently given to a collection of related diseases. In most of the different types of cancer, some cells in the body start to divide without stopping, and eventually spread into surrounding tissues. In normal tissues, healthy cells grow and divide according to the needs of the organism. When cells grow old or become damaged, they are eliminated, and new cells take their place. However, when cancer develops this carefully controlled process breaks down. As multiple alterations accumulate, old or damaged cells survive when they should die, and new cells form even if they are not needed. These extra cells divide uncontrolled and may result in abnormal masses called tumors. Malignant cancerous tumors can spread into surrounding tissues, displacing the neighboring healthy cells. In addition, as the tumor develops, some cancer cells are able to detach from the original tumor mass and travel to distant organs in the body through the circulation. Eventually, these cancerous cells may form metastases, i. e. new tumors far from the original formation.

Nowadays, cancer figures among the leading causes of mortality worldwide, with approximately 14 million new cases and 8.2 million cancer-related deaths in 2012 [173]. Despite new technological advances and significant efforts (projected national expenditures for cancer care are expected to total nearly $157 billions in 2020 just in the United States [118]), the initial hopes put in the war on cancer have been largely disillusioned. Since the 50's, age-adjusted cancer mortality rates have declined by only 11% [50]. Prevention, screening and treatment success with some cancers have saved millions of lives, but the prognosis for many with metastatic cancer is still as gloomy as it was nearly 50 years ago.

Looking at these premises, researchers from quantitative disciplines such as physicists, mathematicians, and engineers have contributed to cancer research over the

last years [155]. One contribution results from discoveries and technological developments, which have led to advances in medical imaging and radiation therapy for the diagnosis and treatment of tumors. A second important contribution is brought by bio-informatics, providing the tools to handle large datasets of genome sequences, gene expression patterns and cell-signaling networks. Finally, a third contribution has recently gained interest. This direction involves a more quantitative investigation of the physical processes underlying the evolution of a tumor. Mathematical models for tumor growth are part of this contribution, and constitute the framework in which this thesis is set.

The aim of this dissertation is to develop mathematical tools that are able to examine the complex interactions between solid tumors and their host microenvironment. We explore the impact that such tools could have on identifying the factors driving tumor evolution. The theoretical framework is also used to test hypotheses on tumor dynamics, and the ensuing results suggest a series of experiments to validate our conclusions.

In this thesis, we focus on two main aspects related to the growth of a tumor mass. First, we analyze the case of a tumor grown *in vitro*, and then we compare model predictions to experimental results. We extend the modeling framework to include the effects of a chemotherapeutic agent on tumor development, and study the influence of mechanical stress on drug efficacy. After that, we discuss a constitutive relation for the tumor mechanical response, which is able to account for cellular adhesion mechanisms. We model different cases of biological interest, investigating the influence of the tumor external environment.

Among the innovative contributions of this research, we would like to highlight a few results:

- we validate our equations with experimental data from tumor spheroids
- from these experiments, we obtain results that confirm and extend the validity of previous findings reported in literature
- we suggest a new mathematical expression that is able to describe growth inhibition by mechanical compression
- our theoretical results suggest a possible interaction between the tumor and its mechanical environment that could influence tumor treatment with chemotherapeutic agents

- we adapt an existing model for the elasto-visco-plastic response of a tissue to our framework, and investigate the effects of different healthy surrounding tissues on tumor development

1.2 Outline of the thesis

The thesis is organized as displayed in Figure 1.1. Chapter 2 provides an introduction about cancer biology. We discuss the current understanding of cancer initiation and development. At the end of the chapter, we provide a brief review on mathematical modeling in cancer.

Chapter 3 covers the modeling of *in vitro* tumor growth. We report on experiments concerning the evolution of tumor spheroids freely growing in the culture medium and subjected to an external mechanical pressure. We compare the model predictions with the experimental results, and suggest a new constitutive relation that is able to describe the effect of growth inhibition by mechanical stress. Then, we perform a parametric study of the model equations, to evaluate the influence of key parameters on tumor evolution. Finally, we discuss the action of a drug on the spheroid growth curves, and evaluate the possible implications of mechanical stresses on therapy effectiveness.

Chapter 4 deals with the constitutive law for the tumor tissue. We present the main assumptions in our framework and summarize the model equations. Then, we investigate a sample problem to highlight the influence of plastic distortions on the mechanical and fluid dynamic response of the tissue. We conclude the chapter with three benchmarks from cases of biological interest, namely the growth of a spherical tumor in culture medium, embedded in a host tissue, and in the presence of a heterogeneous environment.

Finally, Chapter 5 draws the conclusions of the work and gives some hints for future developments.

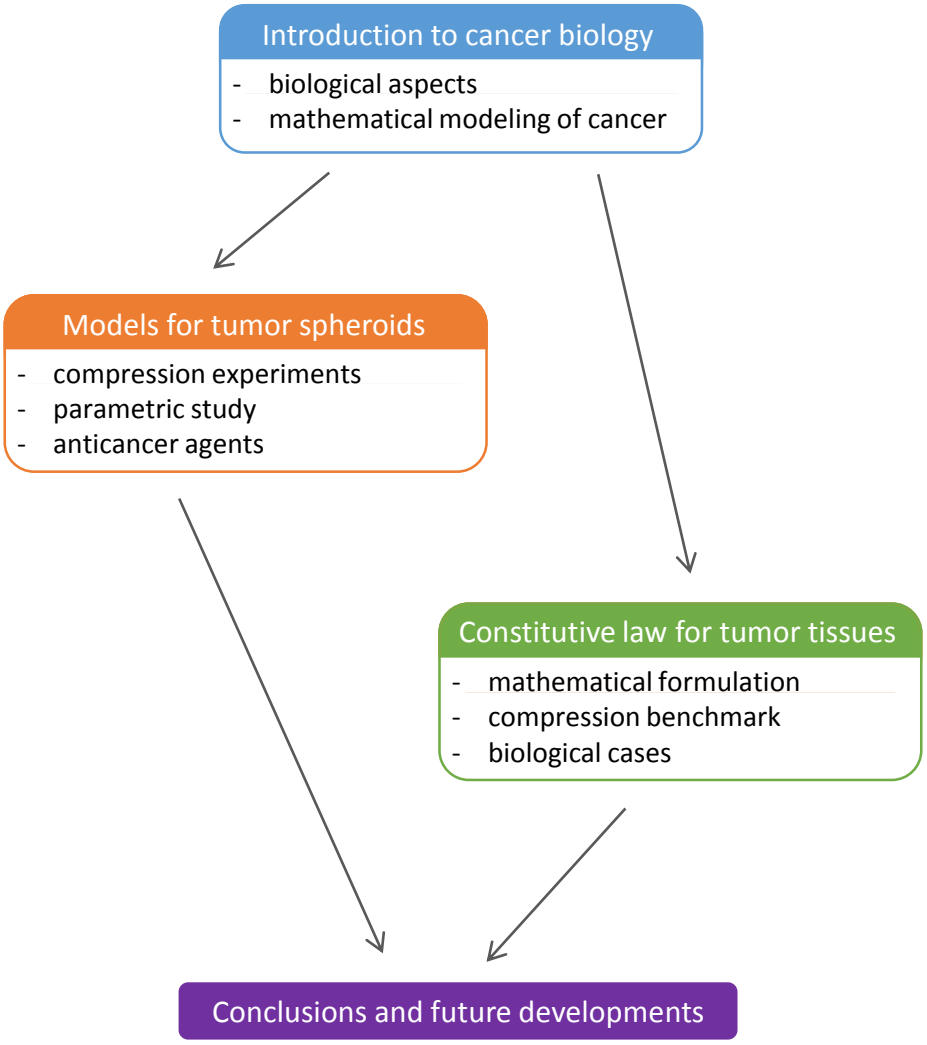

Figure 1.1: Outline of the thesis.

Chapter 2

Introduction to cancer biology

Cancer has been known since the first activities of human societies have been recorded. One of the first evidences dates back to a transcription of a 2500 BC manuscript, containing the teachings of an Egyptian physician. The author describes one of the cases - among different pathological conditions - as a "bulging mass in the breast", cool, hard, dense and spreading insidiously under the skin [154]. In fact, he is giving a vivid description of breast cancer. However, even if the illness is documented in such early years, death by cancer was not so common in the past [100]. One of the main reasons for this is that cancer appears as an aged-related disease. In ancient societies, where a plethora of other illnesses destroyed many lives, people did not live enough to take cancer. Now that infectious diseases have been controlled, the proportion of the population at risk for cancer has increased dramatically. Although cardiovascular diseases are still the main cause of death in the ageing population (at least in developed countries), cancer is a major problem. Nowadays, cancer control, and even more cancer prevention, are main health issues. Nevertheless, cancer research has a wider significance. Almost all multicellular organisms, animals as well as plants, are affected by this illness. Cancer involves mainly alterations in cell proliferation, differentiation and development, so that understanding the processes underlying the disease can help to elucidate the basic mechanisms of life.

The astonishing diversity of the anatomical designs in living beings is allowed by the cellular organization of tissues. Much of this variability can be endorsed to the individual cells: these serve as building blocks for organ and tissue construction, showing great autonomy and adaptability [192]. These features enable the cells to contribute substantially to the maintenance of the whole organism, in terms of wound healing or replacement of worn parts. At the same time, this autonomy poses a serious danger, in that cells may assume roles that are unsuitable for normal tissue functioning. Actually, the information encoded in the genome is subjected to corruption by

different mechanisms, diverting the cells to phenotypes which may show highly abnormal characteristics. Alterations in cell proliferation programs stand among these inappropriate changes. Such alterations, in turn, may lead to large populations of cells that no longer submit to the standard rules of the tissue. As normal cells are carefully programmed to collaborate with their neighbors for the survival of the whole organism, cancer cells appear to be focused on one single task: making more copies of themselves [192].

In his monograph on cancer, published in 1838, Johannes Müller provided a systematic analysis of the microscopic features of benign and malignant human tumors [78]. He attributed cancer to formation of new cells inside a diseased organ, with a potential to spread to other parts of the body. This early results served as a starting point to the forthcoming research, devoted to characterize the tumor cells and identify the differences with their normal counterpart. Nowadays, we have access to a wide array of information concerning cancer cells. Recent technological improvements have provided huge datasets for the genetic sequences in the cancer genome, together with their expressed proteins. The molecular pathways underlying the alterations in tumors are becoming clearer, so that conceptual maps of the cell internal circuitry are being sketched [80]. As our understanding of cancer genetics has improved, new drugs and therapies have been introduced, improving the prognosis for certain treatments. However, many cancers are still difficult to treat and conceptually appealing therapies have proven only marginally effective for patient survival (to this regard, see [141] for a critical review on the contrasting effects in nanotechnology-based therapies). Moreover, some of the questions asked by the early cancer pathologists are still lacking an answer. As cleverly stated in [100], even the most advanced technology in cancer research is not able to provide valuable results if it is not applied properly. That is, now that almost anything seems technically possible, the real issue for researchers is to identify the right questions to ask. As we gain better understanding of cancer and its interactions with the host environment, we realize that cancer is a complex problem that requires due consideration of all the factors to be solved.

In this thesis, we show mathematical and computational tools that are able to analyze the interactions between solid tumors and their host environments. Through these tools, we investigate the effects of such interactions on the development of the tumor mass and we provide some insights into possible treatments.

2.1 From normal cells to cancer

With a strong simplification, we may say that the rebel cells forming a tumor are the result of normal development gone wrong [192]. Even though the organism is endowed with extraordinary safety measures, cancer cells in some way learn to escape them and prosper. Therefore, we begin this dissertation by examining the normal functioning of cells and tissues, providing a small account for the different safeguards. Then, we analyze how a failure in the cellular machinery can lead to cancer.

2.1.1 The structure and function of normal tissues

A *tissue* is a collection of similar cells sharing the same origin that together carry out a specific function. We distinguish between four main tissue groups: the *epithelium* is a tissue composed of specialized cells that line the surfaces of blood vessels and organs throughout the body; the *connective tissue* supports, connects or separates different types of tissues in the body. It contains the extracellular matrix and the fibroblasts entrusted with its remodeling; the muscles in animal bodies are part of the *muscle tissue*; and the *nervous tissue* makes up the bulk of the brain and the nervous system. The term *mesenchyme* refers generally to all supporting tissues collectively (including connective tissue, muscles and bone). On the other hand, the epithelial cells responsible for the functional elements of an organ are termed the *parenchyme*. The specific cells are grouped into organs, which share a standard pattern (see Figure 2.1). There is a layer of epithelium, made of specialized cells performing the actual organ function, supported by a layer of connective tissue - the *stroma*. Blood vessels, nerves and lymphatic vessels pass through the stroma and provide nutrients and nervous control for the specific tissue cells. A thin, semi-permeable *basement membrane* separates the epithelium from the mesenchyme. In normal development there is a controlled mechanism that allows individual organs to reach a fixed size. If a tissue suffers an injury, the surviving cells in most organs start to divide and replace the damaged cells. As soon as it is completed, this process stops and the system returns to an equilibrium (termed *homeostasis*). To maintain this complex structure in homeostasis, the number of each cell type must be carefully controlled, so that cellular proliferation and *apoptosis* (i.e. controlled cell death) are rigorously balanced. When a *somatic* (i.e. non-germline) stem cell senses the loss of a differentiated cell, it divides either symmetrically into two new stem cells or asymmetrically into a stem cell and a progenitor cell. The latter can further divide or differentiate into the desired cell type, which has then to move to the correct

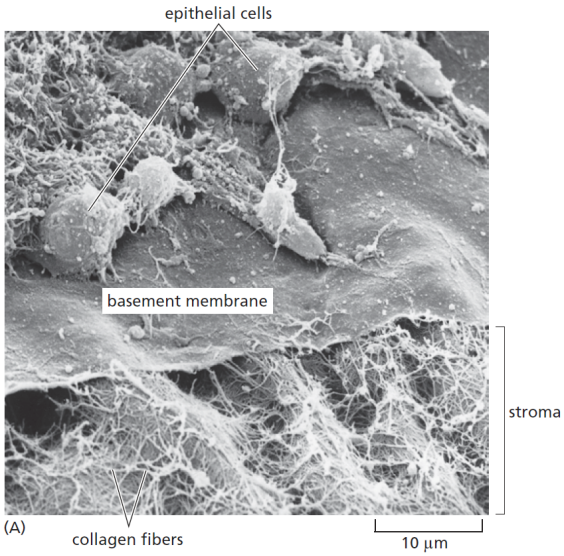

Figure 2.1: Scanning electron micrograph of a chick corneal epithelium. Adapted from [192].

position and assume its function. An involved system of biochemical signals (*growth factors*) regulates this complex process. Cells secrete such factors and their response to them is governed by the activation of certain receptors on the cell surfaces. When the cell surface receptors are engaged, a cascade of biochemical signals activates or deactivates the genes in the cell nucleus. Such environment-mediated changes to gene expression are termed *epigenetic events*. The activated genes then govern the production of proteins within the cell, which in the end are responsible for cell cycle and function. It is becoming clear that the microenvironment influences dramatically gene expression, so that the behavior of a cell is largely determined by its interactions with the extracellular matrix, neighboring cells, and soluble local and systemic cues [135, 2, 16].

2.1.2 The cell cycle

A cell reproduces by performing a highly regimented sequence of events in which eventually duplicates its contents and then divides in two. This cycle of duplication and division, known as the *cell cycle*, is the essential mechanism by which all living things reproduce. Figure 2.2 shows a schematic for the different stages of the cycle. Since many cells require much time to grow and double their mass of proteins and internal structures, most cell cycles have gap phases to allow time for growth. During the first of such gap stages of the cycle, G1, the cell physically grows, synthesizes proteins and builds organelles, and prepares for DNA duplication. In the following

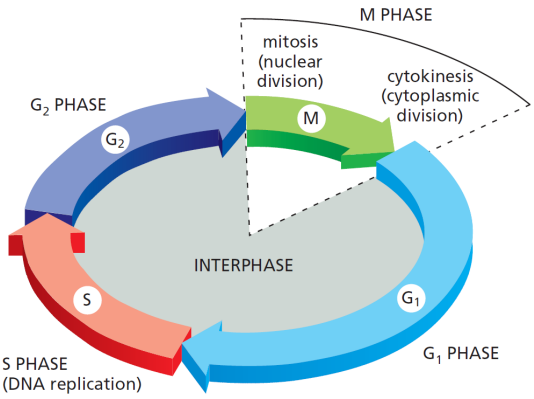

Figure 2.2: The four phases of the cell cycle. Adapted from [2].

synthesis phase, S, the DNA is then copied and in the second gap phase, G2, the cell undertakes the final preparations for DNA division. In the final mitosis phase, M, two copies of the genetic material are separated into two daughter nuclei, and the cytoplasm and organelles are divided into the two newborn cells.

The *cyclin-dependent kinases* (Cdks) are important components of the cell-cycle control system. Their activities rise and fall as the cell progresses through the cycle, leading to cyclical changes in the phosphorylation of intracellular proteins regulating main events of the cell cycle [2]. These changes in Cdk activity are controlled by a vast array of enzymes and other proteins. Among the different regulators, *cyclins* are known to play a key role. Cdks are dependent on cyclins for their activity: Cdk protein kinase activity (i.e. the ability of modifying other proteins by adding phosphate groups to them) is possible only when Cdks are bound to a cyclin. The assembly and activation of cyclin-Cdk complexes at specific stages of the cell cycle results from cyclical changes in cyclin protein levels.

The different stages of the cell cycle are separated by numerous checkpoints. Each of these cellular roadblocks is designed to check for critical errors or malfunctions in the cell. The cell has the opportunity to repair damaged DNA and control the progression through the cycle. One of the most important checkpoints is the restriction point (R) in the late G1 phase, where the cell either commits to division, entering the S-phase, or exits the cycle [144]. Cells that exit the cycle rest in a quiescent state, in a phase of the cycle termed G0. Numerous checkpoints are present as well in the S and G2 phases to control DNA damage and its repair. Since these checkpoints are responsible for controlling cell progression into the cycle, they play a role of paramount importance in cancer initiation and progression. Indeed, the failure

of a checkpoint for DNA damage may lead to increased genetic instability and the following acquisition of cell mutations.

2.1.3 Genes involved in carcinogenesis

Correct interpretation of the growth signals by the cells is fundamental to healthy tissue development. Often, cells receive both growth promoting and inhibiting signals. Their final behavior results from the balance between the contrasting stimuli and the pattern of expressed genes. Genes that are critical for cancer can be grouped into two major classes, according to whether the cancer risk arises from significant or poor activity of the gene product. Genes of the first class, inducing a gain-of-function mutation that can drive a cell towards cancer, are called proto-oncogenes. Their mutant or overexpressed forms are called *oncogenes*. Genes of the second class, in which a loss-of-function mutation can lead to cancer, are called *tumor suppressor genes*. For both the cases, the mutation may drive the cell towards cancer directly, by causing the cell to proliferate when it should not, or indirectly. This second case may happen for mutations that cause *genetic instability*, that is induce high frequency of mutations within the cell genome. In this way, the occurrence of other inherited changes is hastened, stimulating tumor progression. The genes whose alteration results in genomic instability represent a subclass of cancer-critical genes that are sometimes denoted as *genome maintenance genes*. Mutations in oncogenes and tumor suppressor genes can have similar effects in promoting cancer development. Overproduction of a certain signal for cell proliferation, for example, may result from either type of mutation. Interestingly, the techniques that led to the discovery of these two gene categories are quite different. In particular, the mutation of a single copy of a proto-oncogene converting it into an oncogene has a dominant effect on a cell. Thus, an oncogene can be identified by its effect when it is added to the genome of a suitable tester cell. On the other hand, the cancer-causing alleles for the tumor suppressor genes are generally recessive. Often, both copies of the normal gene have to be removed or inactivated before an effect can be recorded. This behavior is schematized in Figure 2.3.

Normal cells can rely on different DNA repair mechanisms to cope with uncontrolled proliferation. Cycle checkpoints can detect errors in DNA replication and halt the process, until the damage is repaired. If repair happens to be impossible, the pathways for cell apoptosis are triggered. Tumor suppressor genes are known to play key roles in these checkpoints, in particular in the one present at the transition

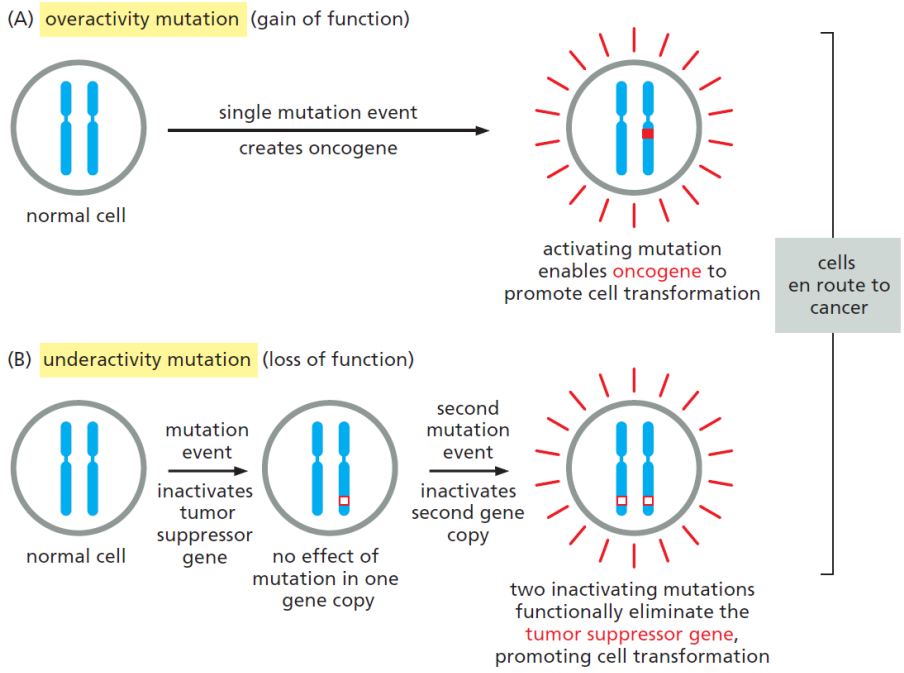

Figure 2.3: Schematics for cancer-critical mutations, falling into dominant and recessive cases. Adapted from [2].

between G2/M phases, right before mitosis. However, these genes can be damaged, leaving the cell more vulnerable and subjected to additional genetic damage.

2.1.4 Possible causes of genetic damage

The genetic material in the cell is susceptible to damage by altering the chemical bonds between the molecules or the molecules themselves. This can occur as a consequence of exposure to chemicals reacting directly with the bases or the backbone of the DNA. Also, high energy radiation interacting with the tissue may generate reactive chemical species harmful to the genetic material. Chemical and physical agents that are able to damage the DNA are generally termed *carcinogens*. One of the first evidences of such substances dates back to 1915, when a Japanese pathologist and his assistant induced tumors on the ears of rabbits using coal tar, demonstrating the carcinogenic properties of the latter [192]. Several components of coal tar were later identified, being common products of combustion. Some of these hydrocarbons were subsequently found in the condensates of cigarette smoke as well.

One of the possible mechanisms of action for carcinogens may be through the production of reactive oxygen species, following their metabolization. Such chemicals can lead to formation of DNA adducts, where the radicals bind to the DNA. These

substances can deform DNA, altering the sequence of the bases in ways that cannot always be repaired. Other DNA damage may be caused by excess energy that can alter the chemical bonds or introduce reactive species. This is the case of UV radiation, which can induce some forms of skin cancer. Other radiations of shorter wavelengths, such as X-rays, can penetrate deeply in the tissue and affect cells in the lower layers. High energy photons damage DNA directly by double-strand DNA breaks or, alternatively, alter the DNA base pairs distorting the DNA structure. A third source of genome damage is given by pathogens. DNA viruses insert their own genetic sequences into the host cells and alter cellular function. Sometimes, the insertion of external sequences can lead to disabling of a tumor suppressor gene or activation of an oncogene. Finally, some deficient genes may just be inherited, rather than obtained from genetic lesions. Inheriting defective tumor suppressor genes may lead, for example, to increased incidence of a particular type of cancer in certain families.

2.1.5 A bit of nomenclature

Cancer cells are characterized by two main features: they reproduce in spite of the normal restraints on cell growth and division, and they invade regions of the organism usually restricted to other cells. An abnormal cell that proliferates out of control will give rise to a *neoplasm*, i.e. a new and abnormal growth. As long as the cells from the neoplasm have not become invasive, the tumor is said to be *benign*. For these types of tumors, removing or destroying the mass is usually enough for a complete cure. A true cancer arises when the tumor becomes *malignant*, that is, when its cell acquire the ability to invade the surrounding tissues. Invasive cancer cells are able to enter the blood and lymphatic vessels, and form secondary tumors called *metastases*. Generally, the more widely the cancer spreads, the harder it becomes to eradicate. In fact, metastases are what kills the patient in general. A classification for different cancers is given traditionally according to the tissue and cell type of origin. For example, *carcinomas* are cancers that arise from epithelial cells. This type of tumor is the most common among human cancers, accounting for about 80% of the cases [2]. Among carcinomas there are tumors arising from the epithelial cell layers of the gastrointestinal tract, as well as the skin, mammary gland, pancreas, liver, lung, ovary, prostate and urinary bladder. The remainder of malignant tumors arise from nonepithelial tissues. The first major class of nonepithelial cancers derive from connective tissues. These tumors, called *sarcomas*, constitute about 1% of the

tumors in the clinic. The second group of nonepithelial cancers arise from cells belonging to blood-forming tissues - *hematopoietic* - including the cells of the immune system. *Leukemias* and *lymphomas* are included in this class. Finally, the third major grouping of nonepithelial tumors arises from cells that form the components of the central and peripheral nervous system. Included here are *gliomas*, *glioblastomas*, *neuroblastomas*, *schwannomas* and *medulloblastomas*. Even if they comprise only 1.3% of all diagnosed cancers, these are responsible for about 2.5% of cancer-related death [192]. Together with the set of names for malignant tumors, there is a related nomenclature for benign ones: for example, an *adenoma* is a benign epithelial tumor with a glandular organization; the corresponding type of malignant tumor is called *adenocarcinoma*. Most cancers have features that reflect their origin. It is the case of *basal-cell carcinoma*, where tumor cells derive from keratinocyte stem cells in the skin and generally continue to synthesize cytokeratin intermediate filaments. Cells from a *melanoma*, instead, originate from pigment cells in the skin and often continue to make pigment granules. Note that cancers originating from different cell types behave generally very differently. Regarding the two previous examples, basal-cell carcinomas are only locally invasive and metastasize rarely. On the other hand, melanomas can become highly malignant and often form metastases.

2.1.6 Some insights into carcinogenesis

Even after the cancer has metastasized, it is usually possible to trace its origin back to a single *primary tumor*, in a specific organ. Primary tumors are thought to derive by cell division from a single cell that initially experienced some heritable change. Afterwards, additional alterations accumulate in some of its descendants, allowing them to outgrow their neighbors. Notably, by the time of its first detection, a typical human cancer will have been developing for already many years, containing a billion cancer cells or more [2]. Strange as it may seem, many lines of evidence suggest that most cancer cells originate from a single aberrant cell. Then, if this is the case, the abnormal cell needs to pass on its abnormality to its progeny, the aberration being heritable. Therefore, development of cancer cell clones has to depend on genetic changes. As previously anticipated, tumor cells contain somatic mutations, that is they display one or more alterations in their DNA sequence that distinguish them from the normal cells surrounding the tumor. Cancers may also be driven by epigenetic changes, i.e. persistent, heritable changes in gene expression that happen without alteration of the DNA sequence. Somatic mutations that alter DNA sequence appear to be frequent in different cancers, and cancer is in this sense a genetic disease.

An estimated 10^{16} cell division occur in a normal human body in the course of a typical lifetime [2]. Even in an environment free of mutagens (agents causing genetic mutations), mutations would occur spontaneously at an estimated rate of about 10^{-6} mutations per gene per cell division. This estimate is due to the existing limitations on the accuracy of DNA replication and repair. Therefore, during a typical lifetime, every single gene has possibly undergone mutation on about 10^{10} separate occasions. Among the resulting mutated cells, a large number will sustain deleterious mutations in genes regulating cell growth and division, which may cause the cells to disobey the normal restrictions on proliferation. Given these estimates, it seems reasonable to ask ourselves why cancer occurs so rarely. A possible explanation is based on the fact that a single gene mutation is not likely enough to convert a healthy cell into a cancerous one. The development of a cancer typically requires a substantial number of independent, rare genetic and epigenetic alterations to occur in the lineage deriving from a single cell. The observed incidence of cancer as a function of age is a clear indication of this behavior. In fact, for most types of cancers the incidence rises steeply with age, as it would be expected if cancer was caused by a progressive accumulation of a set of mutations in a single lineage of cells. These indirect arguments have now been confirmed by sequencing of the genomes of tumor cells from cancer patients and characterizing the mutations that they contain. The progressive accumulation of mutations in a number of different genes helps to explain the phenomenon of *tumor progression*, in which an initial mild disorder of cell behavior evolves gradually into an actual cancer (see Figure 2.4 describing cancer progression in the uterine cervix). Thus, tumor progression involves a large element of chance and usually takes many years. At each stage of progression, some individual cell acquires an additional mutation or epigenetic change that, said with the language of natural selection, provides a selective advantage over its neighbors. The new abilities gained by the cell may ease its thriving in the tumor environment, which is usually characterized by harsh conditions (such as low levels of oxygen or poor nutrient concentrations). The offspring of the best-adapted cells continue to divide, eventually giving rise to the dominant clones in the growing mass. Since new mutations arise continuously within the tumor mass, different subclones may gain advantage and predominate. These may be overtaken in turn and outgrown by their own sub-subclones. The increasing genetic diversity encountered in cancer progression is one of the main factors that makes treatment difficult.

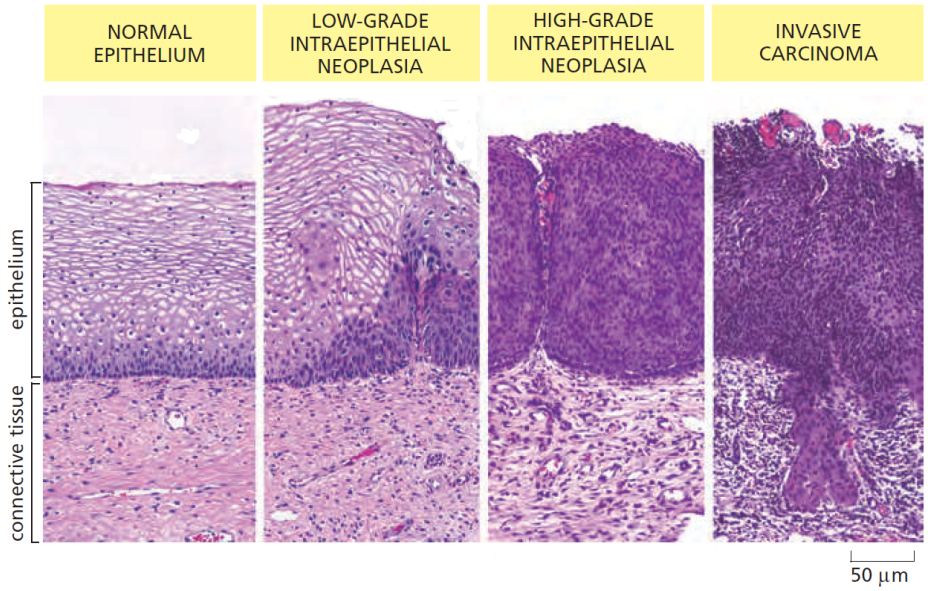

Figure 2.4: Stages of progression in the development of cancer of the epithelium of the uterine cervix. Adapted from [2].

2.1.7 Distinctive traits of cancer cells

A large cell population number creates the opportunity for mutations to occur, but the driving force for cancer development resides in the selective advantages possessed by the abnormal cells. A mutation or epigenetic change can confer a significant advantage by increasing the rate at which a cell clone proliferates or by enabling it to continue proliferating despite the controlling signals. Cancer cells grown in culture typically display a transformed phenotype, showing an altered shape, motility, and response to growth factors. Contrary to normal cells, which do not divide unless attached firmly to the substrate, transformed cells often divide even if held in suspension. Moreover, normal cells are inhibited from moving and duplicating when the culture reaches confluence - i.e. cells reach a high density. Instead, transformed cells continuously move and divide even after confluence, piling up in layers in the culture dish. What is observed in culture gives a hint of the possible misbehaviors happening in a tumor growing into a host tissue. However, cancer cells in the body show additional features that mark them out even more from normal cells.

In general, when sufficient oxygen is present, normal tissue cells fully oxydize almost all the carbon in the glucose they uptake to obtain CO_2, subsequently lost as a waste product by the body. Growing tumors need lots of nutrients to obtain the building blocks for new macromolecules. Indeed, most tumors have a metabolism which is more similar to the one of a growing embryo, than to that of an adult tissue.

In particular, tumor cells consume glucose greedily, importing this substance from the blood at a rate much higher than neighboring normal cells. Only a small fraction of this imported glucose is used for ATP production by oxidative phosphorylation. Instead, a significant quantity of lactate is produced, with many of the remaining carbon atoms derived from glucose that are diverted for use as raw materials needed by the growing tumor cells. This tendency for exaggerated glucose consumption and altered energy metabolism observed in cancer cells is called the *Warburg effect*, from Otto Warburg observation in 1924 [188]. Remarkably, the abnormally high glucose uptake allows to image tumors selectively by whole-body scans (employing techniques such as PET and using suitable contrast agents), providing a way to monitor cancer progression.

As mentioned in the previous sections, powerful safety mechanisms guard against the troubles caused by deranged cells. Some of these mechanisms operate to halt cell proliferation, leading eventually to apoptosis. Cancer cells require additional mutations to elude these defenses against cellular misconduct. Such mutations drive the cell into an abnormal state, unbalancing metabolic processes and production of cell components. To thrive, cancer cells must accumulate mutations that disable the normal safeguard mechanisms, which would otherwise induce such cells to commit suicide. Note that, even if cancer cells fail to undergo apoptosis, this does not mean that they rarely die. In fact, the interior of large solid tumors is characterized by massive cell death. This results from extremely difficult living conditions, with severe competition among cancer cells for nutrients. Typically, cells die due to necrosis, allowing the tumor to grow only if the cell birth rate outpaces the death one. According to this explanation, tumor double in size over a timescale that can be much slower than the doubling time for cell proliferation.

Most of normal human cells display a limit to the number of times they can divide when stimulated to proliferate in culture. After a certain number of population doublings, they stop dividing. This internal counting mechanism is termed *replicative cell senescence* and it generally depends on progressive shortening of the telomeres - a telomere is a region of repetitive nucleotide sequences at each end of a chromosome [80]. The replication of telomere DNA during the S phase depends on the enzyme telomerase, which maintains a special telomeric sequence protecting chromosome ends from deterioration. Since many proliferating human cells are deficient in telomerase, their telomeres shorten with every division, their protective action deteriorates, and a DNA damage signal is eventually created. The altered chromosome ends can trigger a permanent cell-cycle arrest, causing a normal cell to die. Remarkably, cancers cells

are able to avoid replicative senescence in different ways. They can keep telomerase active as they proliferate, so that their telomeres do not shorten; otherwise, they can evolve alternate mechanisms for elongating their chromosome ends. Regardless of the strategy adopted, the striking result is that the deranged cells continue proliferation under conditions in which normal cells would instead stop.

2.2 The stages of solid tumor growth

Once a tumor has established an outpost in the host tissue, it starts a stage of rapid growth and becomes an *in situ* cancer. Further development of a solid tumor is generally divided into three main phases, namely the (i) avascular, (ii) vascular, and (iii) metastatic stages.

2.2.1 Avascular solid tumor growth

Said quite simply, avascular tumor growth is the growth of tumors in the absence of blood vessels. As the tumor grows from a small cluster of initial cancer cells, it interacts with the external environment of the host tissue. It mechanically displaces and compresses the surrounding tissues, including the existing vasculature and lymphatics. The tumor degrades and remodels the extracellular matrix (ECM) both biomechanically - by inducing strains in the matrix - and biochemically. This second form of chemical remodeling is usually performed by the secretion of matrix degrading enzymes (MDEs) such as matrix metalloproteinases (MMPs) [17]. MMPs degrade the ECM that, in turn, can release ECM-associated growth factors that further fuel tumor growth [80]. Moreover, ECM degradation by MDEs increases the tumor ability to expand into the surrounding tissues, both by reducing the mechanical stiffness of the matrix and by providing additional space for the growing mass [116]. Tissue invasion results from the dual contribution of proliferation-induced pressure and proteolytic degradation of the surrounding tissues. Such expansion forces sheets, or fingers, of tumor cells along lines of least mechanical resistance in the neighboring regions [100]. Notably, there is supporting evidence that the tumor may induce epigenetic changes in the adjacent stromal cells, fostering development of the cancer [80, 54]. Even the action of cells from the immune system is affected by the presence of the tumor. The immune cells operate in conflicting ways: tumor-antagonizing and tumor promoting immune cells can be found, in different proportions, in many neoplastic lesions [44, 80].

In this early stage of cancer, the tumor has not yet established its own vascular network. Thus, it must rely upon the host tissue for delivery of required substances - such as oxygen, glucose or growth factors - via diffusion from the surrounding vascularized tissues. Nutrients enter the tumor and are uptaken by proliferating cancer cells. In particular, oxygen diffuses over distances of the order of 100-200 μm into tissue, before dropping to levels insufficient for cellular metabolism [29]. When the tumor radius exceeds this diffusion limit, oxygen can no longer reach the tumor interior, and only cells at the tumor border still experience an adequate oxygen supply. An hypoxic region is formed in the tumor center, contributing to the selection of more aggressive cancer cells. At this stage, rapid cell proliferation in the outer regions is still able to increase the overall tumor volume. However, as the tumor mass expands, the size of the hypoxic regions increases and oxygen levels continue to drop in the center. If the oxygen concentration drops to critically low levels, then hypoxic cells start to die by *necrosis*. During this process, the contents of the cell - organelles and biological chemicals - are released into the microenvironment and are slowly degraded over time. The cellular water content eventually escapes through the interstitial space in the tumor, together with degraded cellular material that is subsequently removed by immune cells. The tumor starts to lose volume and, as the size of the necrotic core grows, the rate of volume gain from proliferation eventually balances with the rate of volume loss by necrosis. After some time, this leads to a steady tumor size, with a characteristic diameter of about 1-2 mm.

2.2.2 Vascular tumor growth

The second stage of cancer development can be interpreted as a consequence to the hypoxia and nutrient deprivation encountered during avascular tumor growth. The ultimate response is *tumor angiogenesis*, a process in which the tumor induces endothelial cells (ECs) to form a new vasculature, supplying the cancer cells with the nutrients necessary for their proliferation. Actually, the observation that angiogenesis occurs around tumors was made nearly 100 years ago, and the hypothesis that tumors produce a diffusible angiogenic substance was put forward in 1968 [29].

Nowadays, it is known that hypoxia is able to trigger a number of biological changes in most animal cells [194]. Hypoxia inducible-factors (HIFs) are present within cells regardless of oxygen levels. However, under normoxic conditions, HIF-1α (a member of the HIF family) results to be inactivated. On the contrary, when stabilized by hypoxic conditions, HIF-1α upregulates several genes to promote survival

in low-oxygen conditions. In particular, genes that increase cellular motility are activated, and at the same time cells start to secrete tumor angiogenic growth factors (TAFs), such as the vascular endothelial growth factor (VEGF) [29]. TAFs diffuse outward from the hypoxic regions of the tumor and eventually reach the neighboring blood vessels.

Healthy blood vessels are composed of tightly connected ECs, surrounded by a basement membrane and other supporting cells - such as smooth muscle cells and pericytes [102]. When the TAF gradient is detected by the ECs, they begin to secrete matrix degrading enzymes that are able to break down the basement membrane and the ECM. This allows the ECs to migrate from the original blood vessel towards the TAF source in the tumor. The first migrating ECs are termed *sprout tips* and, immediately behind them, other ECs start to divide and migrate. Eventually, they align and form tubes of polarized ECs, surrounding a vascular lumen. These events are represented schematically in Figure 2.5. The new vessels then link with the old

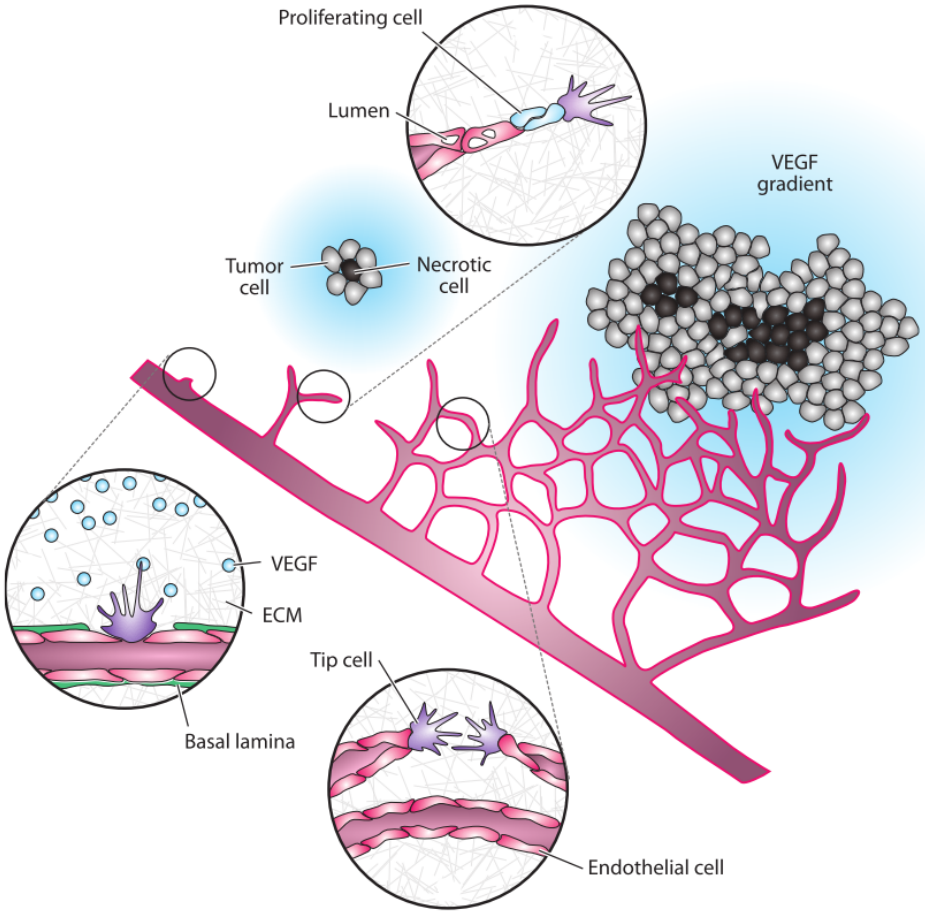

Figure 2.5: Tumor-induced sprouting angiogenesis. Adapted from [102].

ones and form a network of loops during a process called *anastomosis*. The resulting neovasculature provides the tumor with a direct supply of oxygen and other nutrients. Note that the final vasculature architecture is actually determined by the balance of pro- and anti-angiogenic growth factors (competing in the so called *angiogenic switch*), as well as by the mechanical stresses arising in the tumor and in the new blood vessels [91].

Nourished by this new vascular network, cancer cells begin a stage of rapid proliferation. However, even if critical for further tumor development, the tumor angiogenic network is far from being efficient. Due to their pathological nature, tumor blood vessels are often leaky, displaying large gaps between ECs. The newly formed vessels are tortuous and the regular branching patterns observed in healthy tissues are almost lost. In addition, the basement membrane outside the vessels may not be fully formed and some of the newly born vessel walls may be composed of a mosaic of tumor cells and ECs [89, 29, 92]. The resulting inefficiency hinders fluid flow and drug delivery in tumors. Eventually, it gives rise to harsh conditions that select even more malignant clones of cancer cells.

2.2.3 Tissue invasion and metastasis

Cancer cells spread and multiply at new sites in the body through a process called *metastasis*. This aspect is what causes most of cancer related deaths, however it also remains the least understood. Indeed, it is estimated that metastasis accounts for 90% of deaths from cancer [2]. After it had spread throughout the body, a cancer becomes almost impossible to eradicate by surgery or radiation. Remarkably, metastasis itself is a multistep process, which is often referred to as the *invasion-metastasis cascade* [80]. During this stage of tumor development, cancer cells invade local tissues and vessels, move through the circulation, leave the vessels, and then establish new cellular colonies at sites far from the primary tumor (Figure 2.6). Each of these events is a complex process, in which most of the underlying mechanisms are still not clear. Cancer cells are able to build metastases after escaping the constraints that keep normal cells in their proper places. Malignant tumors are indeed characterized by a certain degree of invasiveness, showing disorganized patters of growth and irregular borders, with extensions into the surrounding tissues. Although the molecular changes underlying this invasive behavior are still not understood, it is clear that invasiveness requires a disruption of the mechanisms keeping cells tethered to their proper neighbors and to the ECM. Moreover, it is becoming increasingly apparent

that a crosstalk between the cancer cells and the tumor stroma is involved in acquiring the capabilities needed for invasion. Malignant phenotypes do not seem to arise in a strictly cell-autonomous manner, and their occurrence cannot be understood solely by the analysis of tumor cell genomes.

For carcinomas, the cellular tendency to move away from the original site resembles the *epithelial-mesenchymal transition* (EMT), occurring in some epithelial tissues during normal development. By co-opting a process involved in various steps of embryonic morphogenesis and wound healing, carcinoma cells can concomitantly acquire multiple features enabling invasion. The second step of metastasis, that is the establishment of colonies in distant organs, begins with cell entry into the circulation. To accomplish this, invasive cancer cells have to cross the walls of blood or lymphatic vessels. The latter, displaying larger radii and more deformable walls than blood vessels, allow cancer cells to enter in small clumps. Then, such clumps may become trapped in lymph nodes, giving rise to lymphnode metastases. Cancer cells entering blood vessels, instead, seem to do so singly. Modern techniques for sorting cells according to their surface properties are able, in some cases, to detect these *circulating tumor cells* (CTCs) in samples of blood from cancer patients [77]. This task is extremely difficult, since CTCs are only a minute fraction of the total blood-cell

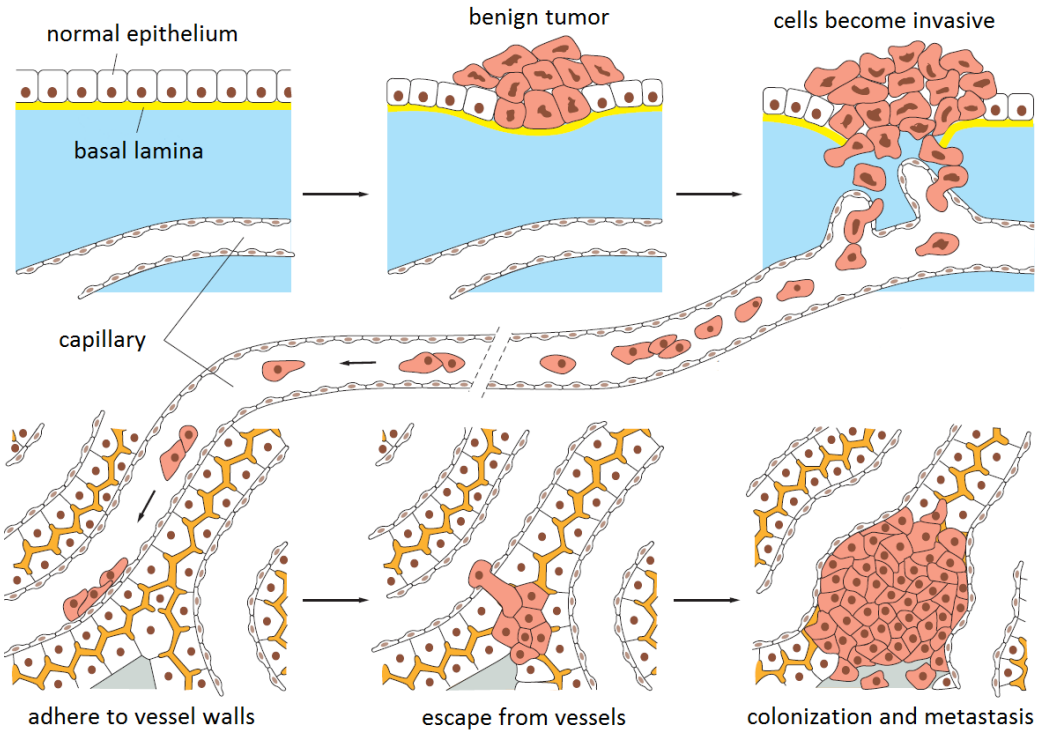

Figure 2.6: Steps in the invasion-metastasis cascade. Adapted from [2].

population. Only a small proportion of the cancer cells that enter circulation succeed in making its exit, settling in new sites. Very few cells manage to survive and proliferate in the foreign environment, starting metastases. Experiments have shown that fewer than one in thousands, perhaps one in millions, are successful in this sequence of events [2]. Note that the migrating cells may fail to survive in the alien environment, or they may only thrive for a short period - forming a *micrometastasis* - before dying out. Moreover, many cancers are discovered before forming metastatic colonies and can be cured by removing the primary tumor. However, an undetected micrometastasis can remain dormant for many years before revealing its presence by forming a secondary tumor, long after the primary tumor has been removed.

To conclude this section, it is interesting to note that without the proper tumor-host interaction, the destination microenvironment will not support the newly arrived cancer cells and the following formation of metastases. In 1889 Stephen Paget, an English surgeon, noticed that mechanical forces alone could not account for the metastatic dissemination of a tumor [139]. Later work showed that, while CTCs are found in the vasculature of multiple organs, only certain sites develop metastatic tumor deposits. As reviewed in [142], some clinical findings in cancer patients show that solid tumors have a propensity to set home preferentially to distinct organs, as it is seen in metastasis of melanoma to the lung and brain. The metastatic cells behave like seeds from certain plants, which thrive exclusively in distinct favorable ecosystems - an idea which is known as the *seed and soil hypothesis*. Even though mechanical forces are employed in delivering the tumor cells to secondary sites, successful colonization is strongly dependent on a receptive microenvironment. Indeed, recent evidences show that this distant microenvironment is arranged prior to cancer cell arrival, creating a "landing site" for future metastatic growth. This modified microenvironment in a distant host tissue is sometimes referred to as the *pre-metastatic niche*. Remarkably, the existence of such a primed environment implies that metastases to a particular organ are not a random occurrence, but rather an already determined event.

2.3 Mathematical models for cancer

As shown in the previous sections, cancer understanding is made difficult by a wide set of problems. The involved spatial and temporal scales span from the biochemistry of DNA mutation to grown tumors. Consequently, several mathematical modeling approaches have been used to investigate these problems. Here we discuss a brief history of mathematical models for cancer developed over the past years. For an

extended discussion, we refer the reader to the reviews in [14, 10, 153, 33, 158, 24, 164, 3].

In general, statistical techniques can be applied to experimental data to reveal correlations between observable phenomena. Then, it is necessary to postulate hypotheses to establish the reasons underlying these correlations, stating which physical processes are involved and how they interact [24]. Biological experiments for testing these hypotheses may be extremely time-consuming, expensive, or even impossible with the current technologies. In such cases, mathematical modeling can play an intermediate role, providing an independent check for the consistency of the hypotheses. If a model derived from such hypotheses is not able to reproduce the observed phenomena, then the original statements have to be modified before carrying on the work. Moreover, mathematical models can improve the design of experiments by highlighting which measurements are required to test a particular theory, or whether supplementary information can be obtained by collecting additional data. Finally, the parameters that feed the equations in the models can be varied over a large set, providing a thorough characterization of the system. These ideas are summarized in Figure 2.7, where the different stages involved in the formulation of the mathematical model are represented. Actually, mathematical modeling is an iterative process and

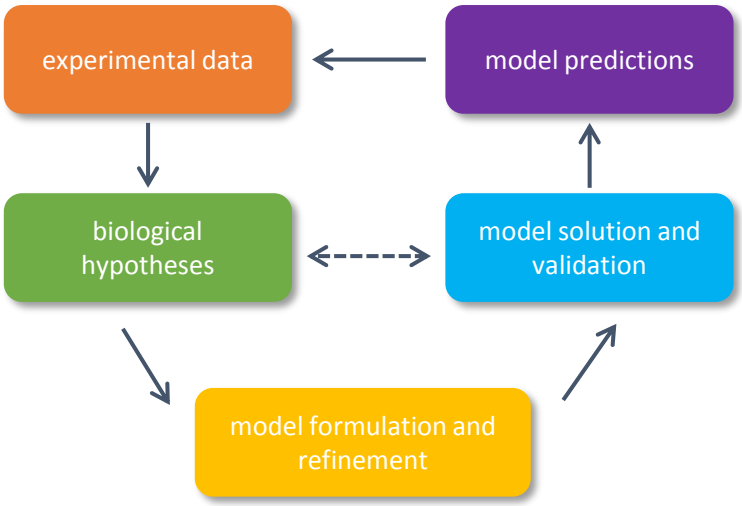

Figure 2.7: Different stages involved in mathematical modeling. Adapted from [24].

the success of its predictions relies on a continuous collaboration between experimentalists and theoreticians.

2.3.1 Models for avascular tumor growth

One of the earliest models for cancer initiation was developed by Armitage and Doll in 1954 [11]. The model is derived by the analysis of cancer mortality statistics, comparing different cancer types. The theory states that the age distribution of a cancer is proportional to a power of age, with an exponent related to the number of changes needed for cancer progression. Although the theory provides an excellent description for cancers of the colon, stomach and pancreas, it fails to describe some of the others. In addition, the authors' findings do not provide a mechanistic insight into the functional changes responsible for the disease progression.

By the analysis of similar incidence statistics for retinoblastoma, Knudson proposed that only two changes (or "hits") are needed to cause the disease [101]. Therefore, for children with familial retinoblastoma that are born with the first hit only another mutation is required, increasing the chances of developing the tumor. Notably, the identification of the RB1 tumor suppressor gene in 1987 confirmed this two-hit hypothesis.

Among the earliest spatio-temporal models for avascular tumor growth, Greenspan describes how the size and structure of a spherical tumor change when different hypotheses on cell viability and proliferation are considered [73]. According to the hypotheses that were used in this work and in similar ones, the tumor is assumed to remain radially symmetric for all the discussion. Cell proliferation is regulated by a single, diffusible growth factor that is supplied externally, such as oxygen. Growth inhibiting factors can be produced internally and affect the mitotic rate of the cells. Notably, the distribution of a growth factor in the tumor regulates its local dynamics, with expansion occurring when cell growth exceeds death and regression in the opposite case. The integration of these contributions over tumor volume leads to an equation similar to the following one:

$$\frac{dR}{dt} = \frac{1}{R^2} \int_{r=0}^{R} F(c) r^2 \, dr,$$

relating the time evolution of the tumor radius $R(t)$ to $c(t)$, the concentration of growth factor in the spheroid. Here, $F(c)$ models the influence of the growth factor on the net cell growth rate at each point of the spherical tumor. If c represents a nutrient, for example, F can be thought to increase as c increases, and it will possibly reach the maximum value for a large value of c. Then, the spatial distribution of c is determined by the solution of the following diffusion equation:

$$\frac{\partial c}{\partial t} = \frac{D}{r^2} \frac{\partial}{\partial r} \left(r^2 \frac{\partial c}{\partial r} \right) - g(c, R),$$

where D represents the diffusion coefficient of the growth factor, and g describes its local rate of consumption. This latter function is specific for the growth factor used and might depend on the proliferation state of the cells. Threshold values of the growth factor can delineate regions of cell proliferation, quiescence or necrosis. Then, the resulting distribution of cell populations can be compared with tumor histologies. Interestingly, models of this form show good qualitative - and sometimes also quantitative - agreement with experimental data. Typically, these models predict an evolution of the tumor radius that is exponential with time for the first days, when the concentration of the growth factor is high over the whole domain. After that, a transient linear phase follows and finally the tumor reaches an equilibrium size at which the rates of cell growth and death balance. Asymptotic techniques can be applied for some physically relevant conditions, leading to analytical solutions. These can be used to evaluate physical quantities of interest, such as the growth speed, in terms of model parameters [189].

Due to the many simplifications, these early models have limited applicability. In particular, the presence of a unique cell population is limiting, since the stochastic appearance of different cell clones cannot be investigated. At the same time, cell metabolism is controlled by a single diffusible species, whereas multiple metabolites are actually involved. Extensions and modifications of these original models became numerous during later years (see the reviews in [146, 10, 158] for a detailed account). Significant developments include relaxing the hypothesis of radial symmetry and the inclusion of different cell populations within the tumor. For example, in a subsequent paper Greenspan used classical perturbation theory to predict how the boundary of an invasive tumor develops, departing from spherical symmetry [74]. Cristini and coworkers, on the other hand, employed sophisticated numerical methods to solve a nonlinear system of equations and relate the irregular boundaries of the tumor to key parameters of the model [41]. Interestingly, their findings show that highly vascularized tumors remain compact in shape while growing, whereas those with limited availability of nutrients tend to develop invasive protrusions, eventually leading to tumor fragmentation.

Mechanical aspects were incorporated at later times, starting with equations for cell movements depending on a cellular "pressure". In the model of Greenspan [74], for example, the cell culture is regarded as an incompressible fluid composed of cells and cellular debris in which a distribution of sources and sinks is present (given by cell proliferation and necrosis, respectively). Cell movement is due to pressure gradients arising from the boundary of the tumor, where nutrient and pressure levels are high,

towards the tumor center, where the nutrient and pressure levels are low. In addition, surface tension or cell-cell adhesion are assumed to maintain a compact tumor shape, countering the expansive forces due to growth. Remarkably, the analysis of the equations show that the strength of cellular adhesion influences tumor morphology. In particular, strong adhesion yields radially symmetric tumors, whereas weak adhesion leads to irregular tumor boundaries.

Several authors have developed biomechanical models where the tumor is considered as a mixture of interacting components [21, 23, 58, 195]. Usually, the model is composed of two main phases: tumor cells and interstitial fluid. Some of these multiphase models are based on porous media theory. Generally, in this kind of models different balance equations regulate the exchange of mass and momentum among the constituents [26, 159, 32, 6, 167, 8]. Since the mathematical models developed in this dissertation belong to this second group, we discuss below some examples from these categories.

In [195], the authors develop and simulate a diffuse interface continuum model for multispecies tumor growth. The model is able to account for adhesive forces among the cell species, introducing an adhesion energy from continuum thermodynamics. Using an efficient numerical scheme, the authors are able to solve the equations for the different cell populations and the substrate components. They present simulations for unstable avascular tumor growth in two and three dimensions. Interestingly, the tumors at the end of the simulations display complex shapes, dependent on different cell adhesions.

In [6], Ambrosi and Preziosi report on a mathematical model for tumor growth that accounts for adhesion mechanisms between tumor cells. The ECM is described as an elastic compressible material, while the constitutive relationship between the stresses and the strains within the cellular constituents is obtained via a multiplicative decomposition of the deformation gradient tensor. This decomposition results in the splitting of the total deformation into a growth, a plastic and an elastic part. On the basis of biological considerations, a yield condition on the cellular mechanical stresses is postulated, separating the elastic and dissipative regimes. Finally, numerical tests display how mechanical stress is able to influence tumor growth, and where it is able to generate cellular reorganization.

Sciumè and coworkers [167] present a multiphase model for avascular tumor growth based on porous media mechanics. They describe the tumor as composed by the ECM, which constitutes the solid skeleton of the porous material, tumor cells, healthy cells and interstitial fluid. Also, tumor cells are divided into proliferating and necrotic,

whereas a nutrient is transported into the interstitial fluid. The model is able to account for different interfacial tensions between cells and interstitial fluid, and distinct mechanisms for cell-ECM adhesion. They study three different cases, namely the growth of a tumor spheroid, an avascular tumor embedded in a host tissue, and a tumor cord model. When host cells are present, the relative difference in adhesion to the ECM between the former and tumor cells drives tumor infiltration. Subsequently, the model has been extended to account for different interfacial tensions between tumor cells, healthy cells and interstitial fluid [165], for a deformable ECM [166], and for the presence of TAF and ECs to model angiogenesis [160].

In [8], the authors develop a mathematical model for avascular tumor growth in the brain. The tumor grows in a three dimensional setting, where the domains for the gray and white matter and the cerebrospinal fluid are constructed from magnetic resonance images. The tumor and the host tissue are modeled as biphasic porous materials, and the effects of radiotherapy are also incorporated in the modeling framework. They observe that the different mechanical properties and the spatial configuration of the tissues surrounding the tumor affect its growth, resulting in strong spatial variation of cellular proliferation and significant deformations of the host tissues.

Models like those presented above are termed continuum models, since they describe how cell populations change without distinguishing between individual cells. In continuum models, the tumors are considered as continuous masses containing a small number of different cell populations, usually neglecting subcellular phenomena. This kind of models is suited for cases where the number of cells in the system is very large, but it should be avoided when describing small clusters of cells, such as metastases. When the number of cells is small, it is possible to use discrete models that view the tumor as a collection of interacting cells. Each cell has assigned its set of parameters and behavioral rules, allowing to study tumor invasion and emergence of clonal subpopulations. The parameters governing cell behavior can be chosen using measurable biological and physical quantities, such as the cell duplication times or their membrane deformation in response to mechanical loading [130, 182, 3].

For example, Quaranta and coworkers [152] use cellular automata models to investigate the influence of the microenvironment, in particular the oxygen concentration, on the development of a tumor. They show that for low oxygen levels the tumor diverges from its initial phenotype and exhibits a large diversity in population, with aggressive phenotypes becoming dominant.

Another example is given in the work by Kim and colleagues [97]. They develop a hybrid model in which a continuum approach is used in regions with high cell density,

whereas a discrete description is used for regions with a small number of cells. In this way, the authors are able to analyze the effects of cellcell adhesion and variable growth rates at the cellular level, even by maintaining some features of the continuum description.

Recently, in [9] the authors integrate biological and computational approaches to derive a hybrid cellular automata model for bone metastases arising from prostate cancer. The model is able to account for the key players in disease progression, reproducing the steps of invasion from prostate to bone. Notably, the temporal evolution of the metastases is highlighted, and the application of clinically relevant therapies to the computational model illustrates the potential of this approach in the clinic.

2.3.2 Models for tumor angiogenesis

One of the first mathematical models for tumor angiogenesis was developed in 1985 by Balding and McElwain [12]. In this work, the authors present a simple model for tumor angiogenesis to describe a set of experiments in which tumor cells stimulate the migration of new blood vessels in the rabbit cornea. The model considers a generic TAF, as well as capillary tips and vessels. Following their notation, we denote by c the TAF concentration, and by ρ and n the capillary and tip densities, respectively. They assume that the TAF, produced by the tumor cells, diffuses towards neighboring vessels. In one dimension, with x representing the distance from the vasculature to the tumor center, these assumptions lead to the following equation for c:

$$\frac{\partial c}{\partial t} = D_{\mathrm{c}} \frac{\partial^2 c}{\partial t^2},$$

where D_{c} denotes the TAF diffusion coefficient. Capillary tips are assumed to emanate from existing vessels and tips at a rate that increases with the TAF levels. Moreover, the tips move by chemotaxis along spatial gradients of TAF and form anastomoses. Combining these effects, the authors derive this equation for the tip density:

$$\frac{\partial n}{\partial t} = -\frac{\partial}{\partial x}\left(n\chi \frac{\partial c}{\partial x}\right) + \alpha_0 c\rho - \beta_2 n\rho,$$

where χ is the chemotaxis coefficient, α_0 is the rate of appearance of new tips, and β_2 is a death term for tips due to anastomosis. The capillary density is assumed to increase only by tips movement so that:

$$\frac{\partial \rho}{\partial t} = -\chi n \frac{\partial c}{\partial x} - \gamma_1 \rho,$$

where γ_1 is a death term for capillaries. Numerical simulations of this model and its extension [25] are able to reproduce several distinctive features of angiogenesis, such as the peak in capillary density tips preceding a peak in the density of capillaries. Interestingly, by altering the key parameters, the models have been used to compare different tumor treatments. For example, by reducing the chemotaxis coefficient it is possible to mimic the effect of a therapy that blocks EC chemotaxis. Alternatively, adding a reaction term in the TAF equation can describe the effect of a particular drug. Other models, based on similar equations, have been extended to include the growth of the tumor during angiogenesis and the intake of nutrients from the new vessels [140]. More detailed models have been developed by Levine et al. [109, 110], taking into account more cell populations, chemical factors and their related receptors. In particular, they include specific pro- and anti-angiogenic factors, together with the interactions between the ECs lining the blood vessels and other cell types, such as pericytes and macrophages.

Some of the following models have focused on the extension of the problem to two and three dimensions (see, for example, [138]). Indeed, one dimensional models are not able to account for the morphology of the vascular network, which plays a major role in the delivery of the nutrients to the growing tumor. In addition, the remodeling of the vessels and the effects of the blood flow on the evolving vasculature have been usually neglected. To meet these requirements, a new class of hybrid models has been developed. In general, these include reaction-diffusion equations for nutrient transport and consumption (in a continuum approach), coupled to cellular automata describing the interactions between normal and tumor cells (in a discrete framework).

For example, Stokes and Lauffenburger [176] couple a probabilistic equation describing the movement of ECs to a continuum distribution of TAF. Their results show that vessels grow directed to the TAF source (i.e. the tumor) only if a chemotactic response of the ECs is enabled. Moreover, a level of random motion is necessary in the equations for EC movement, to produce vessel anastomosis and capillary loop formation. Interestingly, the authors report that the predicted vessel extension rate and network structure are quantitatively consistent with experimental observations of *in vivo* angiogenesis. They suggest that the rate of vessel outgrowth is strongly dictated by the EC migration rate. Therefore, *in vitro* migration assays, where this migration rate can be carefully quantified, may constitute an useful tool for pre-screening of possible tumor angiogenesis treatments. This result is noteworthy, since it highlights the importance of mathematical modeling as a bridge between *in vitro* and *in vivo* experiments.

In another work, McDougall and colleagues present a model describing the vessel network response to perfusion-related haemodynamic forces [123]. In contrast to previous models where the effects of blood flow were neglected or evaluated a posteriori, the blood perfusion generated by this approach has a direct impact during capillary growth, inducing radial adaptations and network remodeling. A parametric study is performed to test the influence of model parameters, and the delivery of a chemotherapeutic drug is investigated. Notably, the model is used to identify possible therapeutic targets that could improve tumor treatment.

As a last example we consider the work in Frieboes and coworkers [61], where the authors extend the diffuse interface model in [195] (previously mentioned for nonlinear solid tumor growth). There are several extensions, including the tracking of multiple viable cell species, the onset and aging of discrete tumor vessels, and the incorporation of individual cell movements using a hybrid continuum-discrete approach. It is shown that the module describing tumor growth is characterized by a morphological instability. Depending on the conditions of the microenvironment, this instability can lead to tumor invasion via individual cells. This intrinsic feature of the tumor growth module is then enriched by the coupling with the vascular network, which undergoes continuous remodeling. Blood vessels can shut down if subjected to a sufficiently high cellular pressure, given by extensive proliferation. This phenomenon affects the intake of nutrients dramatically, leading to hypoxic regions which in turn trigger a higher release of angiogenic regulators.

Finally, note that this field of cancer modeling is currently very active and several models are missing from this brief account. We refer the interested reader to the reviews in [33, 162] for an extended report on the subject.

2.3.3 Models for cancer treatment

Mathematical models constitute a powerful tool to dissect the mechanisms regulating tumor growth. Moreover, mathematical modeling can contribute to the rational design of optimal treatment protocols, involving surgery, chemotherapy and radiotherapy. They can even aid the development of new therapies, suggesting strategies for the cure (see the recent reviews in [45, 124]).

In 1988, Jain and Baxter [90] develop a continuum model to identify the causes of poor drug distribution in vascular tumors. They find that the irregular blood flow, arising in the angiogenic vascular network, hinders significantly the delivery of a therapeutic agent. Moreover, it is shown that high interstitial fluid pressure in the tumor interstitium plays a similar role, by reducing the extravasation of molecules and

driving fluid radially outward from the tumor. These predictions have been verified experimentally [19] and, remarkably, have stimulated the development of vascular normalization therapies.

In the same period, several contributions towards mathematical modeling of cancer treatment response were brought forward. In particular, Norton and Simon [137] study the growth kinetics of tumors during chemotherapy, finding that the tumor grows following a sigmoidal curve. Starting from model results, they argue that a certain class of tumors may require intensive treatment to achieve beneficial response. This prediction was validated later, in a trial with patients affected by breast cancer [39]. Coldman and Goldie [40] presented a stochastic model for chemotherapy of tumors in 1986. The authors derive probabilistic equations for the cell dynamics, studying cell resistance to therapy. They introduce a treatment with two drugs and show how the model can be used to make deductions on the best scheduling therapy. Remarkably, these early works have inspired several researchers to investigate optimum administration schedules for various situations. For example, in [36] the authors develop an evolutionary mathematical model incorporating data from cell cultures. They investigate sensitive and resistant cancer cell dynamics under different treatment schedules. The model predicts alternative therapeutic strategies that could prolong the clinical benefit of current drugs against the resistant cells, delaying the development of resistance.

Other approaches have focused on the response to radiotherapy using the linear-quadratic law, an empirical formula that relates the proportion of cells that survive exposure to a dose of radiation. For instance, Wheldon and colleagues [193] derive an extension of this formula for radiation treatment schedules. In particular, they extend the linear-quadratic model to account for exponential regrowth of the tumor between treatments. Using analytical calculations, the authors are able to derive expressions for the interval between treatments and the optimal radiation dose that should be applied to maximize tumor cell death. Other mathematical studies of radiation treatments have also included the effects of hypoxia [196], more complex growth laws [122] and cellular heterogeneity [99]. An interesting approach is presented in [156]. Here the authors incorporate the linear-quadratic law into a continuum model of glioma cell density, describing cell invasion, proliferation and death due to therapy. Using *in vivo* radiation dose schedules as a reference, the authors investigate the spatio-temporal delivery of radiation dose, treatment response and recovery time for different treatment schemes. Then, a recent study [106] used a mathematical model for glioblastoma treatment response. The authors investigate the effects of

cell differentiation on therapy outcomes. They find that enrichment in a resistant stem-like cancer cell population could prolong survival by increasing the time to disease recurrence. Their strategy was also validated with a randomized mouse trial, showing significant improved survival in the optimized schedule group. As a last example, Stiehl and colleagues [174] derive a mathematical model for patient survival in acute myeloid leukemia. Model results support the evidence that proliferation and self-renewal rates of leukemia stem-like cells have greater impact on the disease course than the same rates in leukemia progenitor cells. By using patient-derived data, it is possible to estimate prognostic factors that otherwise cannot be measured directly.

2.4 Conclusions

It is becoming increasingly clear that cancer is not a typical illness, whose causes can be easily identified. Rather, it appears as a non-deterministic disease, which does not progress as a fixed succession of specific mutations in some genes. There are many molecular routes that lead to clinically identical cancers [125], and the final development of the illness is driven by a multitude of factors, ranging from the tumor microenvironmental details to ageing and lifestyle.

Like other phenomena occurring in living beings, a fundamental understanding of cancer cannot arise from the bare characterization of all its components [125]. Actually, there is a need for a wider perspective than molecular biology alone would be able to offer. This new angle of view may benefit from cross-disciplinary collaborations between physicists, cancer biologists, mathematicians and engineers [155]. Theoretical and computational tools developed inside the framework of the physical sciences can be used to disentangle the complex interactions underlying cancer progression. Among these tools, mathematical models provide a valuable test bench for verifying hypotheses, identifying key biological mechanisms, and optimizing experimental protocols.

To date, most of the mathematical models that have been developed are focused on a qualitative description of the phenomena they are addressing. Many approaches are still descriptive, as detailed data on specific quantities of interest are missing. In fact, as the predictive ability of a model strongly depends on its proper parameterization, it is essential to obtain accurate parameter estimates from *in vitro* or *in vivo* systems or clinical trials [3]. This kind of information is still poor and a closer collaboration between experimental researchers and theoreticians is highly encouraged. The successful integration of these different approaches is crucial for the understanding of

the complexities underlying cancer and, we hope, to devise effective strategies for a cure.

In conclusion, there still might be a long way to go for finding effective treatments for cancer, with great efforts and even some disillusions. However, the opportunity to improve patients' quality of life makes it a journey that it is worth to take.

Chapter 3

Predicting the growth and drug response of tumor spheroids

3.1 A model for multicellular spheroids

3.1.1 Introduction

Cancer is a complex disease involving primarily uncontrolled cell proliferation and migration to distant regions of the body [113]. From the second half of the last century the scientific community has become more and more aware of the difficulties that arise when treating this illness. Nowadays it is clear that a combined effort from all the physical sciences is necessary to advance our understanding of the disease and promote the discovery of new cures [125, 106]. The pioneering works of Greenspan and coworkers [73, 74] paved the way for the development of mathematical models that could investigate the basic principles underlying cancer progression and predict the outcome of therapies. Most continuum models, as the one presented in this work, deal with the avascular phase of tumor growth. During this stage of cancer progression, a small cluster of cancer cells arise in a healthy tissue due to mutations that alter their biochemical pathways. This small region of abnormal cells grows at the expense of the host counterpart, nourished by oxygen and nutrients that diffuse from the vasculature nearby [89, 70]. At a certain point the external nutrients are not enough to sustain the expansion of the growing mass, leading to the formation of cell proliferation gradients starting from the outer regions of the tumor. As time passes by, cancer cells at the center of the tumor experience severe hypoxia and critical conditions that lead to the

Section 3.1 of this chapter is based upon the work in: Mascheroni P, Stigliano C, Carfagna M, Boso D P, Preziosi L, Decuzzi P, Schrefler B A (2016), "Predicting the growth of glioblastoma multiforme spheroids using a multiphase porous media model", *Biomechanics and Modeling in Mechanobiology*, 15(5), 1215-1228.

death and consequent necrosis of some of them. Finally a steady state arises, where cell proliferation at the tumor border balances cell death at the tumor center [55]. The subsequent stage of cancer progression is termed the vascular phase, where tumor cells recruit new blood vessels from the host vasculature through tumor angiogenesis. In this second stage the cancer resumes its previous growth and eventually enters the last stage of the illness, the metastatic phase, where malignant cells evade the tumor area to form metastases at distant regions of the body. Since the study of the first stage can be performed in a more controlled experimental setting, a large set of literature is devoted to the analysis of avascular tumor growth *in vitro*. Experiments are usually carried out on tumor spheroids, three dimensional aggregates of cancer cells that grow in an approximately spherical shape [181, 96, 185, 127]. The investigations on tumor spheroids allow evaluating the extent of the gradients of nutrients and cell proliferation and, more recently, the action of a mechanical stress exerted on the cell aggregates. Helmlinger and coworkers [83] grow tumor spheroids in gels with varying stiffness, and report a decrease in proliferation for stiffer gels. Another example of spheroids grown in gels with varying stiffness is found in [93]. There, cell proliferation and motility are investigated for different concentrations of collagen in the gel matrix. In that work, a positive correlation between increasing concentrations of collagen and cell invasion is reported, followed by an opposite effect on the growth of the spheroids. The original work of Helmlinger is extended in [35], where the authors perform similar experiments and introduce new tools to quantify spheroid deformation and variations in cell proliferation and apoptosis. Another set of experiments is presented in [47], where tumor spheroids are subjected to asymmetric stress fields by the use of microstructured substrates. Finally, Montel and Delarue in two subsequent papers [128, 46] apply mechanical forces on the surface of tumor spheroids through the osmotic effect of Dextran solutions with different concentrations. All these studies report a decrease of tumor cell proliferation as a consequence of the applied stress, even though they are carried out via different experimental configurations.

The earliest continuum models applied to spheroid growth focus on the dependence of cell proliferation on nutrients and other biochemical factors, as reported in the comprehensive reviews of [148, 114]. They are based on mass balance laws for cells and advection-reaction-diffusion equations for nutrient evolution. Later models include more components and the mechanical interaction between them. For these cases, which are usually defined in the framework of mixture theory or porous media theory, momentum balance equations and constitutive relations are needed for describing the mechanical response of each component [5, 148, 51, 67]. Among the first, [32, 64]

incorporated the effect of mechanical stress on cell proliferation obtaining results matching experimental observations. There followed several papers, in which this example of mechanotransduction is investigated with similar approaches [98, 37, 38, 131].

This work arises as an extension of the modeling framework presented in [167]. The model is specialized to tumor spheroids and the solution procedure is simplified, as all the new equations are formulated in spatial coordinates with no need of a reference configuration. A set of experiments is carried out on spheroid cultures to validate the equations. The comparison with the experiments is performed both with spheroids growing freely in the culture medium and subjected to increasing mechanical loads, giving in each case a good match. The experiments suggested the presence of a master curve, a common growth curve underlying the spheroid growth dynamics. Finally, a new constitutive relation is proposed to describe the inhibitory effect of the stress on cell proliferation, with a better performance in terms of matching the experimental results when compared to the existing laws in literature. The remainder of the work is organized as follows. Section 3.1.2 introduces the mathematical framework, based on the Thermodynamically Constrained Averaging Theory (TCAT), and the differences with the original model. In the last part of that section, the equations are specialized to the case of tumor spheroids. Section 3.1.3 presents the experimental setup for the two culturing conditions. Finally, results from the simulations are presented in Section 3.1.4 and the discussion follows in Section 3.1.5.

3.1.2 Mathematical model

This mathematical model is developed in the framework of porous media theory, and the governing equations are derived through the TCAT [71, 72]. We start by defining the problem in terms of microscopic relations amongst the constituents. The TCAT approach is used to transform these microscopic laws into mathematically and physically consistent macroscale relationships, which describe the tumor at the tissue scale. By doing so, the complexity due to the high spatial variability at the microscale is overcome and equations for average quantities describing the tumor behavior are formulated directly. The closed form of the problem is finally obtained by introducing constitutive relations into the macroscale conservation equations. Detailed information about the mathematical model and its derivation are found in previous works of our research group [167, 165, 166]. Here we describe the behavior of the following constituents, or phases: (i) the tumor cells (TCs), which partition into living (LTCs) and necrotic (NTCs) cells, and (ii) the interstitial fluid (IF) (Figure 3.1). The ex-

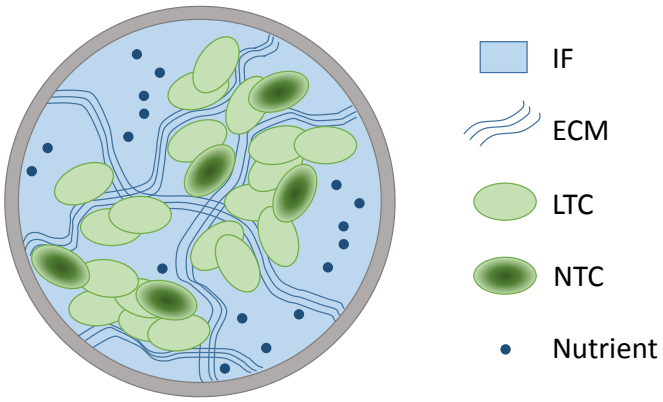

Figure 3.1: Constituents of the biphasic system.

tracellular matrix (ECM) is considered together with the tumor cells and the union of the two entities constitutes the solid skeleton of the tumor. The interstitial fluid phase flows through the pores of this solid matrix, carrying nutrients, growth factors and waste products. Cell proliferation is related to nutrient concentration, whereby cells stop to proliferate and, after some time, undergo necrosis and lysis, if subjected to low levels of nutrients or high levels of mechanical stress. In the following equations, the superscripts "t" and "f" will denote the union of the tumor cells and ECM and the interstitial fluid, respectively.

3.1.2.1 Governing equations

The solid portion of the tumor is modeled as a porous solid with porosity ε^{f}, and its volume fraction is defined as $\varepsilon^{\mathrm{t}} = 1 - \varepsilon^{\mathrm{f}}$. Hence, the interstitial fluid occupies the rest of the volume and the sum of all the volume fractions has to be unity:

$$\varepsilon^{\mathrm{t}} + \varepsilon^{\mathrm{f}} = 1. \tag{3.1}$$

We write the governing equations for the tumor volume fraction (ε^{t}), the interstitial fluid pressure (p^{f}), the nutrient mass fraction (ω^{ox}) and the necrotic mass fraction (ω^{Nt}). These equations are obtained from the general form of the mass and momentum balance equations of phases and species, according to the TCAT derivation.

The mass balance equations for the phases are written as:

$$\partial_t \left(\varepsilon^{\mathrm{t}}\rho^{\mathrm{t}}\right) + \operatorname{div}\left(\varepsilon^{\mathrm{t}}\rho^{\mathrm{t}}\boldsymbol{v}^{\mathrm{t}}\right) - \Gamma_{\mathrm{gr}}^{\mathrm{f}\to\mathrm{t}} + \Gamma_{\mathrm{ly}}^{\mathrm{t}\to\mathrm{f}} = 0, \tag{3.2}$$

$$\partial_t \left(\varepsilon^{\mathrm{f}}\rho^{\mathrm{f}}\right) + \operatorname{div}\left(\varepsilon^{\mathrm{f}}\rho^{\mathrm{f}}\boldsymbol{v}^{\mathrm{f}}\right) + \Gamma_{\mathrm{gr}}^{\mathrm{f}\to\mathrm{t}} - \Gamma_{\mathrm{ly}}^{\mathrm{t}\to\mathrm{f}} = 0, \tag{3.3}$$

where ρ^{α} is the density and $\boldsymbol{v}^{\alpha}$ the velocity of phase α ($\alpha = \mathrm{t}, \mathrm{f}$). The terms $\Gamma_{\mathrm{gr}}^{\mathrm{f}\to\mathrm{t}}$ and $\Gamma_{\mathrm{ly}}^{\mathrm{t}\to\mathrm{f}}$ account for the inter-phase exchange of mass related to cell growth and cell lysis, respectively. The solid tumor phase is composed of two subpopulations, namely necrotic and living cells. The necrotic portion is described by the mass fraction ω^{Nt}, so that the mass fraction of living cells is $\omega^{\mathrm{Lt}} = 1 - \omega^{\mathrm{Nt}}$. We assume that there is no diffusion for the necrotic and living species, and that necrotic cells exchange mass with the interstitial fluid through the lysis term. The mass fraction of necrotic tumor cells (ω^{Nt}) and living tumor cells (ω^{Lt}) are thus given by:

$$\partial_t \left(\varepsilon^{\mathrm{t}}\rho^{\mathrm{t}}\omega^{\mathrm{Nt}}\right) + \operatorname{div}\left(\varepsilon^{\mathrm{t}}\rho^{\mathrm{t}}\omega^{\mathrm{Nt}}\boldsymbol{v}^{\mathrm{t}}\right) - \varepsilon^{\mathrm{t}} r^{\mathrm{Nt}} + \Gamma_{\mathrm{ly}}^{\mathrm{t}\to\mathrm{f}} = 0, \tag{3.4}$$

$$\partial_t \left(\varepsilon^{\mathrm{t}}\rho^{\mathrm{t}}\omega^{\mathrm{Lt}}\right) + \operatorname{div}\left(\varepsilon^{\mathrm{t}}\rho^{\mathrm{t}}\omega^{\mathrm{Lt}}\boldsymbol{v}^{\mathrm{t}}\right) + \varepsilon^{\mathrm{t}} r^{\mathrm{Nt}} - \Gamma_{\mathrm{gr}}^{\mathrm{f}\to\mathrm{t}} = 0, \tag{3.5}$$

where r^{Nt} represents an intra-phase exchange term accounting for the rate of death of living tumor cells.

The evolution of the mass fraction of oxygen (ω^{ox}), the unique nutrient considered here, follows the equation:

$$\partial_t \left(\varepsilon^{\mathrm{f}}\rho^{\mathrm{f}}\omega^{\mathrm{ox}}\right) + \operatorname{div}\left(\varepsilon^{\mathrm{f}}\rho^{\mathrm{f}}\omega^{\mathrm{ox}}\boldsymbol{v}^{\mathrm{f}}\right) - \operatorname{div}\left(\varepsilon^{\mathrm{f}}\rho^{\mathrm{f}} D^{\mathrm{ox}} \operatorname{grad}\omega^{\mathrm{ox}}\right) + \Gamma_{\mathrm{ox}}^{\mathrm{ox}\to\mathrm{t}} = 0, \tag{3.6}$$

where D^{ox} is the diffusion coefficient of oxygen in the extracellular space and $\Gamma_{\mathrm{ox}}^{\mathrm{ox}\to\mathrm{t}}$ is a mass exchange term accounting for nutrient consumption by tumor cells metabolism and growth. Note that the mass exchange term $\Gamma_{\mathrm{ox}}^{\mathrm{ox}\to\mathrm{t}}$ in equation (3.6) is included in the reaction term $\Gamma_{\mathrm{gr}}^{\mathrm{f}\to\mathrm{t}}$ of equations (3.2) and (3.3), since this quantity is related to the exchange of mass and nutrients between the two phases (for more details see [167] and the references therein).

Following porous media theory [111, 143], the mechanical stress exerted on the solid phase is described through the effective stress tensor $\boldsymbol{\sigma}_{\mathrm{eff}}^{\mathrm{t}}$, given by:

$$\boldsymbol{\sigma}_{\mathrm{eff}}^{\mathrm{t}} = \boldsymbol{\sigma}_{\mathrm{tot}} + \alpha_{\mathrm{B}} p^{\mathrm{f}} \boldsymbol{I}, \tag{3.7}$$

where $\boldsymbol{I}$ is the unit tensor, $\boldsymbol{\sigma}_{\mathrm{tot}}$ is the total stress tensor, p^{f} is the fluid pressure in the interstitial fluid and α_{B} is Biot's coefficient defined by:

$$\alpha_{\mathrm{B}} = 1 - \frac{K}{K_{\mathrm{T}}}, \tag{3.8}$$

with K bulk modulus of the unsaturated skeleton and K_{T} bulk modulus of the solid phase. Then, we can state the linear momentum balance law for the tissue as [111]:

$$\operatorname{div}\boldsymbol{\sigma}_{\mathrm{tot}} = \operatorname{div}\left(\boldsymbol{\sigma}^{\mathrm{t}}_{\mathrm{eff}} - \alpha_{\mathrm{B}} p^{\mathrm{f}} \boldsymbol{I}\right) = 0. \tag{3.9}$$

The relative velocity of the interstitial fluid phase is given by a Darcy type equation obtained by TCAT [72]:

$$\varepsilon^{\mathrm{f}}\left(\boldsymbol{v}^{\mathrm{f}} - \boldsymbol{v}^{\mathrm{t}}\right) = -\frac{k}{\mu^{\mathrm{f}}}\operatorname{grad} p^{\mathrm{f}}, \tag{3.10}$$

where k is the intrinsic permeability of the solid matrix and μ^{f} is the dynamic viscosity of the interstitial fluid. The equations of state for the phases can be approximated as [163]:

$$\frac{1}{\rho^{\mathrm{f}}}\frac{\partial \rho^{\mathrm{f}}}{\partial p^{\mathrm{f}}} = \frac{1}{K_{\mathrm{L}}}, \tag{3.11}$$

$$\frac{1}{\rho^{\mathrm{t}}}\frac{\partial \rho^{\mathrm{t}}}{\partial\left(\langle \boldsymbol{n}_{\mathrm{t}} \cdot \boldsymbol{\sigma}_{\mathrm{t}} \cdot \boldsymbol{n}_{\mathrm{t}} \rangle\right)} \simeq \frac{1}{\rho^{\mathrm{t}}}\frac{\partial \rho^{\mathrm{t}}}{\partial p^{\mathrm{f}}} = \frac{1}{K_{\mathrm{T}}}. \tag{3.12}$$

Here $1/K_{\mathrm{L}}$ and $1/K_{\mathrm{T}}$ are the liquid and solid compressibility, respectively, and the quantity $\langle \boldsymbol{n}_{\mathrm{t}} \cdot \boldsymbol{\sigma}_{\mathrm{t}} \cdot \boldsymbol{n}_{\mathrm{t}} \rangle$ is the normal stress at the solid surface averaged over the solid surface [163]. Considering (3.11)-(3.12), equation (3.2) can be written as:

$$\frac{\partial \varepsilon^{\mathrm{t}}}{\partial t} + \frac{\varepsilon^{\mathrm{t}}}{K_{\mathrm{T}}}\frac{\partial p^{\mathrm{f}}}{\partial t} + \operatorname{div}\left(\varepsilon^{\mathrm{t}}\boldsymbol{v}^{\mathrm{t}}\right) + \frac{\varepsilon^{\mathrm{t}}}{\rho^{\mathrm{t}}}\boldsymbol{v}^{\mathrm{t}} \cdot \operatorname{grad}\rho^{\mathrm{t}} - \frac{1}{\rho^{\mathrm{t}}}\left(\Gamma^{\mathrm{f}\to\mathrm{t}}_{\mathrm{gr}} - \Gamma^{\mathrm{t}\to\mathrm{f}}_{\mathrm{ly}}\right) = 0. \tag{3.13}$$

Following the same steps for equation (3.3), it is possible to obtain:

$$\frac{\partial \varepsilon^{\mathrm{f}}}{\partial t} + \frac{\varepsilon^{\mathrm{f}}}{K_{\mathrm{L}}}\frac{\partial p^{\mathrm{f}}}{\partial t} + \operatorname{div}\left(\varepsilon^{\mathrm{f}}\boldsymbol{v}^{\mathrm{f}}\right) + \frac{\varepsilon^{\mathrm{f}}}{\rho^{\mathrm{f}}}\boldsymbol{v}^{\mathrm{f}} \cdot \operatorname{grad}\rho^{\mathrm{f}} + \frac{1}{\rho^{\mathrm{f}}}\left(\Gamma^{\mathrm{f}\to\mathrm{t}}_{\mathrm{gr}} - \Gamma^{\mathrm{t}\to\mathrm{f}}_{\mathrm{ly}}\right) = 0. \tag{3.14}$$

Then, summing (3.13) and (3.14) gives:

$$\left(\frac{\varepsilon^{\mathrm{t}}}{K_{\mathrm{T}}} + \frac{\varepsilon^{\mathrm{f}}}{K_{\mathrm{L}}}\right)\frac{\partial p^{\mathrm{f}}}{\partial t} + \operatorname{div}\left(\varepsilon^{\mathrm{t}}\boldsymbol{v}^{\mathrm{t}} + \varepsilon^{\mathrm{f}}\boldsymbol{v}^{\mathrm{f}}\right) - \frac{\rho^{\mathrm{f}} - \rho^{\mathrm{t}}}{\rho^{\mathrm{f}}\rho^{\mathrm{t}}}\left(\Gamma^{\mathrm{f}\to\mathrm{t}}_{\mathrm{gr}} - \Gamma^{\mathrm{t}\to\mathrm{f}}_{\mathrm{ly}}\right) = 0, \tag{3.15}$$

where the gradients of the densities have been neglected and the constraint in (3.1) has been exploited. Substituting (3.1) and (3.10) in (3.15) leads to:

$$\left(\frac{1-\varepsilon^{\mathrm{f}}}{K_{\mathrm{T}}} + \frac{\varepsilon^{\mathrm{f}}}{K_{\mathrm{L}}}\right)\frac{\partial p^{\mathrm{f}}}{\partial t} + \operatorname{div}\boldsymbol{v}^{\mathrm{t}} - \operatorname{div}\left(\frac{k}{\mu^{\mathrm{f}}}\operatorname{grad} p^{\mathrm{f}}\right) - \frac{\rho^{\mathrm{f}} - \rho^{\mathrm{t}}}{\rho^{\mathrm{f}}\rho^{\mathrm{t}}}\left(\Gamma^{\mathrm{f}\to\mathrm{t}}_{\mathrm{gr}} - \Gamma^{\mathrm{t}\to\mathrm{f}}_{\mathrm{ly}}\right) = 0. \tag{3.16}$$

3.1.2.2 Constitutive relation for the stress

In order to close the system of equations it is necessary to define a constitutive relation for the stress in the tumor phase. A series of experiments based on single-cell force spectroscopy [13, 151, 81, 63] suggests the following phenomenological description at the microscale. When cells are well separated from each other, they do not experience any interaction. As soon as the distance between two cells is below a certain threshold they start attracting each other and, once cells are in contact, an adhesive force builds up if they tend to be pulled apart. If the two cells are further pushed together, a repulsive force is observed. This repulsive force tends to high values as cells become more and more packed. Note that, in the context of porous media theory, the volume fraction of tumor cells can be chosen as a surrogate for cell distance. In mathematical terms, this can be written as a pseudo-potential law [23] (see [149] for qualitative analyses on this kind of nonlinear systems) that describes the stress in the tumor tissue:

$$\Sigma\left(\varepsilon^{\mathrm{t}}\right) = \begin{cases} \alpha\left(\varepsilon^{\mathrm{t}} - \varepsilon_0^{\mathrm{t}}\right)^2 \left[\dfrac{1-\varepsilon_{\mathrm{n}}^{\mathrm{t}}}{\left(1-\varepsilon^{\mathrm{t}}\right)^{\beta}} - \dfrac{1}{\left(1-\varepsilon^{\mathrm{t}}\right)^{\beta-1}}\right], & \text{if } \varepsilon^{\mathrm{t}} > \varepsilon_0^{\mathrm{t}} \\ 0, & \text{otherwise} \end{cases} \tag{3.17}$$

A schematic of cell behavior is shown in Figure 3.2, displaying the evolution of Σ for different volume fractions. Note that with this description the ensemble of tumor cells

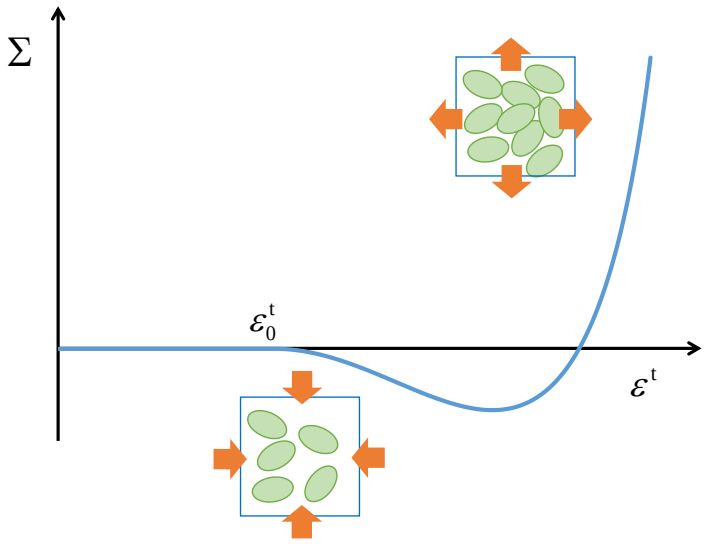

Figure 3.2: Scheme for the stress function Σ. The two insets represent forces acting on the cells for different degrees of tumor volume fractions.

and ECM behaves like an elastic fluid and the effective stress follows the relation:

$$\boldsymbol{\sigma}_{\mathrm{eff}}^{\mathrm{t}} = -\Sigma\left(\varepsilon^{\mathrm{t}}\right)\boldsymbol{I}, \tag{3.18}$$

with Σ defined in (3.17) and positive in compression.

3.1.2.3 Mass transfer relations

The reaction terms in equation (3.2) represent tumor cell growth and lysis, respectively. In particular, the first term is related to cell proliferation and depends on the exchange of mass between the interstitial fluid and the living portion of the tumor. Its form is given by:

$$\Gamma_{\mathrm{gr}}^{\mathrm{f}\to\mathrm{t}} = \gamma_{\mathrm{g}}^{\mathrm{t}} G\left(\omega^{\mathrm{ox}}\right) H\left(\boldsymbol{\sigma}_{\mathrm{eff}}^{\mathrm{t}}\right) \omega^{\mathrm{Lt}}\varepsilon^{\mathrm{t}}, \tag{3.19}$$

where the coefficient $\gamma_{\mathrm{g}}^{\mathrm{t}}$ accounts for the nutrient uptake and for the mass of interstitial fluid that becomes tumor due to cell growth. The function G accounts for the effect of nutrient level on cell growth, while H describes the inhibition of cell growth due to the mechanical stress exerted on the cells. Finally, the factor $\omega^{\mathrm{Lt}}\varepsilon^{\mathrm{t}}$ accounts for the volume fraction of viable tumor cells (i.e. only viable cells can proliferate).

The second reaction term in equation (3.2) accounts for cell lysis in the necrotic cell population (NTCs). Its form is given by:

$$\Gamma_{\mathrm{ly}}^{\mathrm{t}\to\mathrm{f}} = \gamma_{\mathrm{f}}^{\mathrm{t}}\omega^{\mathrm{Nt}}\varepsilon^{\mathrm{t}}. \tag{3.20}$$

Here, $\gamma_{\mathrm{f}}^{\mathrm{t}}$ takes into account the degradation of cellular membranes and the mass conversion into interstitial fluid. Since $\omega^{\mathrm{Nt}}\varepsilon^{\mathrm{t}}$ is the volume fraction of necrotic cells, the lysis term is active only on the dead part of the tumor tissue.

The rate of necrosis of tumor cells in equation (3.4) is described by the relation:

$$\varepsilon^{\mathrm{t}} r^{\mathrm{Nt}} = \gamma_{\mathrm{n}}^{\mathrm{t}} I\left(\omega^{\mathrm{ox}}\right) \omega^{\mathrm{Lt}}\varepsilon^{\mathrm{t}}, \tag{3.21}$$

where the parameter $\gamma_{\mathrm{n}}^{\mathrm{t}}$ regulates the rate of cell death. The function I describes cell necrosis by lack of nutrient. By doing so, cell death is considered to solely depend on nutrient concentration. Note that equation (3.21) can be readily modified to include also other effects, such as the action of a particular drug or mechanical stress.

During the growth of the tumor, nutrients are subtracted from the interstitial fluid, so that the mass exchange term in equation (3.6) takes the form:

$$\Gamma_{\mathrm{ox}}^{\mathrm{ox}\to\mathrm{t}} = \gamma_0^{\mathrm{t}} \frac{\omega^{\mathrm{ox}}}{\omega^{\mathrm{ox}} + c_{\mathrm{ox}}} \omega^{\mathrm{Lt}}\varepsilon^{\mathrm{t}}. \tag{3.22}$$

This expression is validated experimentally in [30, 31] and takes into account the dependence of nutrient consumption on the local level of nutrient in the tissue. The two oxygen uptake parameters γ_0^{t} and c_{ox} describe respectively the order of magnitude of oxygen uptake in the tumor and the oxygen mass fraction at which oxygen consumption is reduced by half. The functions G, H and I are derived from phenomenological arguments and are selected to be similar to the available literature on the topic [23, 158, 195, 98, 167, 131]. In particular, the following set is assumed:

$$G(\omega^{\mathrm{ox}}) = \left\langle \frac{\omega^{\mathrm{ox}} - \omega^{\mathrm{ox}}_{\mathrm{crit}}}{\omega^{\mathrm{ox}}_{\mathrm{env}} - \omega^{\mathrm{ox}}_{\mathrm{crit}}} \right\rangle_+, \tag{3.23}$$

$$H(\boldsymbol{\sigma}^{\mathrm{t}}_{\mathrm{eff}}) = 1 - \delta_1 \frac{\langle \Sigma \rangle_+}{\langle \Sigma \rangle_+ + \delta_2}, \tag{3.24}$$

$$I(\omega^{\mathrm{ox}}) = \left\langle \frac{\omega^{\mathrm{ox}}_{\mathrm{crit}} - \omega^{\mathrm{ox}}}{\omega^{\mathrm{ox}}_{\mathrm{env}} - \omega^{\mathrm{ox}}_{\mathrm{crit}}} \right\rangle_+. \tag{3.25}$$

Here $\omega^{\mathrm{ox}}_{\mathrm{crit}}$ is the oxygen threshold value below which cell growth is inhibited, the constant $\omega^{\mathrm{ox}}_{\mathrm{env}}$ is the environmental mass fraction of oxygen, and the Macaulay brackets $\langle \cdot \rangle_+$ indicate the positive value of their argument. Since ω^{ox} within the spheroid can only be equal or smaller than $\omega^{\mathrm{ox}}_{\mathrm{env}}$, it follows that the brackets will return a number between one ($\omega^{\mathrm{ox}} = \omega^{\mathrm{ox}}_{\mathrm{env}}$) and zero ($\omega^{\mathrm{ox}} \leq \omega^{\mathrm{ox}}_{\mathrm{crit}}$) [165, 166]. The constants δ_1 and δ_2 (with $\delta_1 < 1$) account for the action of mechanical stress on cell proliferation, modeling the inhibitory effect of compression on tumor cells duplication [83, 35, 129]. Note that the expression for H is different from the usual forms assumed in literature. Indeed, some authors use a linear expression, as for example in [159, 98, 178], whereas others consider an inversely proportional relation [23]. However, as it will be shown in the next sections, the relation in equation (3.24) is able to better describe the experimental results.

3.1.2.4 The tumor spheroid case

The mathematical model presented above is extended in view of the comparison with the experiments. In this work the focus is on modeling tumor spheroids, which are an aggregate of tumor cells approximately of spherical shape [180, 104, 53]. As a starting point, we adapt the equations of the more general model for spherical symmetry. If the constituents are assumed incompressible and the densities of the phases are supposed to be equal ($\rho^{\mathrm{t}} = \rho^{\mathrm{f}} \equiv \rho$), equation (3.15) becomes:

$$\operatorname{div}\left(\varepsilon^{\mathrm{t}} \boldsymbol{v}^{\mathrm{t}} + \varepsilon^{\mathrm{f}} \boldsymbol{v}^{\mathrm{f}}\right) = 0. \tag{3.26}$$

Note that, in this way, Biot's coefficient takes the value $\alpha_{\mathrm{B}} = 1$. In spherical symmetry, equation (3.26) reads:

$$\frac{1}{r^2}\frac{\partial}{\partial r}\left[r^2\left(\varepsilon^{\mathrm{t}}v^{\mathrm{t}} + \varepsilon^{\mathrm{f}}v^{\mathrm{f}}\right)\right] = 0, \tag{3.27}$$

which, by symmetry, gives:

$$v^{\mathrm{f}} = -\frac{\varepsilon^{\mathrm{t}}}{\varepsilon^{\mathrm{f}}}v^{\mathrm{t}} = -\frac{\varepsilon^{\mathrm{t}}}{1-\varepsilon^{\mathrm{t}}}v^{\mathrm{t}}. \tag{3.28}$$

Substituting the new relation into equation (3.10) gives the expressions for the phase velocities as:

$$v^{\mathrm{t}} = \frac{k}{\mu^{\mathrm{f}}}\frac{\partial p^{\mathrm{f}}}{\partial r}, \quad v^{\mathrm{f}} = -\frac{\varepsilon^{\mathrm{t}}}{1-\varepsilon^{\mathrm{t}}}\frac{k}{\mu^{\mathrm{f}}}\frac{\partial p^{\mathrm{f}}}{\partial r}. \tag{3.29}$$

From the point of view of the motion of the phases, since the hydraulic conductivity k/μ^{f} is a positive constant, (3.29) implies that the interstitial fluid is directed opposite to the pressure gradient while tumor cells move along it. When the interstitial fluid pressure is higher in the tumor center, the interstitial fluid flows towards the boundary of the tumor whereas tumor cells move in the direction of the tumor center as observed experimentally in [49, 92] and already discussed in [23]. This mechanism enables the recirculation of interstitial fluid in the tumor tissue: tumor cells in the inner regions of the tumor become necrotic due to nutrient deprivation and turn into interstitial fluid after lysis. This fluid flows towards tumor periphery and can be employed by proliferating cells. From the equilibrium equation for the total stress (3.9), and equations (3.7) and (3.18), we arrive at the important relation:

$$\frac{\partial p^{\mathrm{f}}}{\partial r} = -\frac{\partial \Sigma}{\partial r} = -\Sigma'\frac{\partial \varepsilon^{\mathrm{t}}}{\partial r}, \quad \Sigma' \equiv \frac{\partial \Sigma}{\partial \varepsilon^{\mathrm{t}}}. \tag{3.30}$$

The final system of equations for spherical symmetry and with the new expressions for the velocities reads:

$$\frac{\partial \varepsilon^{\mathrm{t}}}{\partial t} - \frac{1}{r^2}\frac{\partial}{\partial r}\left(r^2\varepsilon^{\mathrm{t}}\frac{k}{\mu^{\mathrm{f}}}\Sigma'\frac{\partial \varepsilon^{\mathrm{t}}}{\partial r}\right) - \frac{1}{\rho}\left(\Gamma_{\mathrm{gr}}^{\mathrm{f}\to\mathrm{t}} - \Gamma_{\mathrm{ly}}^{\mathrm{t}\to\mathrm{f}}\right) = 0, \tag{3.31}$$

$$\frac{\partial\left(\omega^{\mathrm{Nt}}\varepsilon^{\mathrm{t}}\right)}{\partial t} - \frac{1}{r^2}\frac{\partial}{\partial r}\left(r^2\omega^{\mathrm{Nt}}\varepsilon^{\mathrm{t}}\frac{k}{\mu^{\mathrm{f}}}\Sigma'\frac{\partial \varepsilon^{\mathrm{t}}}{\partial r}\right) - \frac{1}{\rho}\left(\varepsilon^{\mathrm{t}}r^{\mathrm{Nt}} - \Gamma_{\mathrm{ly}}^{\mathrm{t}\to\mathrm{f}}\right) = 0, \tag{3.32}$$

$$\begin{aligned}\frac{\partial\left[\left(1-\varepsilon^{\mathrm{t}}\right)\omega^{\mathrm{ox}}\right]}{\partial t} &+ \frac{1}{r^2}\frac{\partial}{\partial r}\left(r^2\omega^{\mathrm{ox}}\varepsilon^{\mathrm{t}}\frac{k}{\mu^{\mathrm{f}}}\Sigma'\frac{\partial \varepsilon^{\mathrm{t}}}{\partial r}\right)\\ &- \frac{1}{r^2}\frac{\partial}{\partial r}\left[r^2\left(1-\varepsilon^{\mathrm{t}}\right)D^{\mathrm{ox}}\frac{\partial \omega^{\mathrm{ox}}}{\partial r}\right] + \frac{1}{\rho}\Gamma_{\mathrm{ox}}^{\mathrm{ox}\to\mathrm{t}} = 0.\end{aligned} \tag{3.33}$$

The growth of the spheroid is modeled as a free-boundary problem, and the interface constituted by the tumor cells moves with velocity v^{t}:

$$\frac{dR}{dt} = v^{\mathrm{t}} = -\frac{k}{\mu^{\mathrm{f}}}\Sigma' \frac{\partial \varepsilon^{\mathrm{t}}}{\partial r}\bigg|_{r=R}, \tag{3.34}$$

with R being the radius of the spheroid. To close the differential problem in (3.31)-(3.33) it is necessary to define a set of boundary and initial conditions. In particular, no-flow boundary conditions are assumed at the spheroid center, while Dirichlet boundary conditions are assumed on the tumor external surface:

$$\frac{\partial \varepsilon^{\mathrm{t}}}{\partial r} = \frac{\partial \omega^{\mathrm{Nt}}}{\partial r} = \frac{\partial \omega^{\mathrm{ox}}}{\partial r} = 0, \quad \text{in } r = 0, \tag{3.35}$$

$$\varepsilon^{\mathrm{t}} = \varepsilon^{\mathrm{t}}_{\mathrm{ext}}, \quad \omega^{\mathrm{Nt}} = 0, \quad \omega^{\mathrm{ox}} = \omega^{\mathrm{ox}}_{\mathrm{env}}, \quad \text{in } r = R. \tag{3.36}$$

Note that the first condition in (3.36) implies prescribing an external stress on the tumor surface, since from (3.17) and (3.18) we have:

$$\Sigma\left(\varepsilon^{\mathrm{t}}_{\mathrm{ext}}\right) = \Sigma_{\mathrm{ext}}. \tag{3.37}$$

In the case of a stress-free growing spheroid, the external volume fraction satisfies:

$$\Sigma\left(\varepsilon^{\mathrm{t}}_{\mathrm{ext}}\right) = 0, \quad \varepsilon^{\mathrm{t}}_{\mathrm{ext}} = \varepsilon^{\mathrm{t}}_{\mathrm{n}}. \tag{3.38}$$

Finally, the following initial conditions are assumed throughout the domain:

$$\varepsilon^{\mathrm{t}} = \varepsilon^{\mathrm{t}}_{\mathrm{ext}}, \quad \omega^{\mathrm{Nt}} = 0, \quad \omega^{\mathrm{ox}} = \omega^{\mathrm{ox}}_{\mathrm{env}}, \quad \text{for } 0 < r < R \text{ at } t = 0. \tag{3.39}$$

3.1.3 Materials and methods

3.1.3.1 Cell culture and spheroid formation

Human multiforme glioblastoma U-87 MG cells (ATCC) are grown at 37 °C at 5% CO2 in EMEM (HyClone) supplemented with 50 U/mL penicillin, 50 μg/mL streptomycin and 10% FBS (v/v). Multicellular U-87 MG spheroids are prepared by the liquid overlay method [179, 28]. Briefly, serum free EMEM medium with 2% (w/v) agar is prepared and sterilized; 50 μL of the agar solution is added to the bottom of each well of the 96-well plates to prevent cell adhesion onto the well surface. Plates are allowed to cool down before use. U-87 MG cells are counted and then seeded at different densities: 1000, 5000 and 10000 cells/well. Plates are centrifuged for 5 min at 1000 x g. Spheroid diameter is measured every 2 days using Nikon Eclipse Ti microscope (Nikon) with NIS-Element software. The culture medium is replaced with fresh medium every 3 days.

3.1.3.2 Cell viability and spheroid compression experiments

For the compression experiments, Dextran is added to the culture medium to exert mechanical stress on the spheroids as reported in [128, 129, 46]. Briefly, cell culture medium is mixed with the purified Dextran ($M_w = 100$kDa) and the resulting solution is placed at 37 °C to obtain full solubilization. To test the effect of the Dextran solutions on U-87 MG cell viability, XTT assay is performed [175]. In particular, 10000 cells are plated in each well of 96-well plate. After 24 h, the medium is substituted with different concentrations of Dextran medium (20 g/l, 55 g/l and 80 g/l). After 72 h of incubation, the XTT assay is performed according to the manufacturers protocol. The same solutions of Dextran at different concentrations are prepared to test the effect of different mechanical pressures on the surface of the spheroids. In particular, 5000 U-87 MG cells are seeded in 48-well plates (day 0), as reported before, and the Dextran medium is added after spheroid formation (day 3) at a concentration of 20 g/l to exert 1 kPa, 55 g/l to exert 5 kPa and 80 g/l to exert 10 kPa. The stress acting on the spheroids is estimated as in [128, 129, 46] via the following mathematical expression:

$$p = 286c + 87c^2 + 5c^3,$$

where p is the obtained external mechanical pressure (Pa), and c is the concentration of Dextran (% w/w). This expression was originally derived to describe the osmotic pressure of Dextran solutions in colloidal systems [18] and then validated to hold also for the spheroid compression experiments [129].

Spheroid diameter measurement and medium replacement follow the same procedures described above.

3.1.4 Results

3.1.4.1 Evolution of tumor spheroids

The mathematical framework presented above is applied to analyze the growth of a multicellular tumor spheroid *in vitro*. In particular, the growth of the tumor mass is investigated, including necrotic tumor cells and the consumption of nutrient (oxygen) over time. The geometry of the problem and the boundary conditions are described in Figure 3.3. Note that all the boundary value problems in the thesis have been solved using the commercial finite element software COMSOL Multiphysics (COMSOL, Inc., Burlington, MA, USA). At the boundary B1, the TC volume fraction (ε^{t}), the oxygen mass fraction (ω^{ox}), and the necrotic cell mass fraction (ω^{Nt}) are fixed over time. Then, zero fluxes for all phases are imposed at the symmetry boundaries B2. Finally,

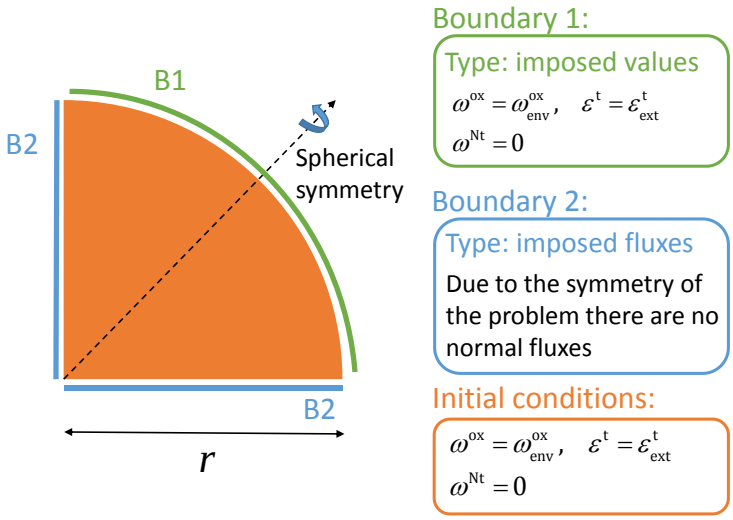

Figure 3.3: Scheme for the geometry of a tumor spheroid immersed in cell culture medium. The initial and boundary conditions for the differential problem are reported on the right.

the initial values for the tumor cell volume fraction, the oxygen mass fraction, and the necrotic cell mass fraction are selected as prescribed by (3.39) and reported in the figure. All other governing parameters are listed in Table 3.1. Numerical results for the evolution of the three principal variables of the model are shown in Figure 3.4. In Figure 3.4.a, the volume fraction of tumor cells in the spheroid is plotted for different times over the spheroid radius. Initially, the tumor is composed only by living tumor cells and interstitial fluid. After a few days, necrotic tumor cells appear in the center of the spheroid. Living tumor cells are restricted to the outer portion of the tumor, where there is still enough nutrient to support their growth. At day 25, necrotic cells occupy the main portion of the spheroid, constituting the *necrotic core*, while the proliferating portion of the tumor is further reduced. Since tumor growth is described by equations (3.19) and (3.23), only tumor cells that experience an oxygen level over the critical threshold are allowed to proliferate. This means that the living tumor cells that can actually proliferate are distributed only over a small portion of the radius near the external boundary, called the *proliferative rim*. The remaining portion of living cells are non-proliferating cells that can resume proliferation after an increase in the level of nutrient. Note that the volume fraction of IF is approximately constant over time, apart for a small increase at the spheroid center and reduction at the spheroid periphery. These are due, respectively, to the lysis term active at the

Table 3.1: Parameters for the simulation of spheroid growth.

Symbol	Parameter	Unit	Value	Reference
$\omega_{\text{env}}^{\text{ox}}$	Environmental oxygen mass fraction	$(-)$	7.0×10^{-6}	[134, 133]
$\omega_{\text{env}}^{\text{ox}}$	Environmental oxygen mass fraction[a]	$(-)$	7.7×10^{-6}	[134, 133]
c_{ox}	Coefficient for oxygen consumption	$(-)$	1.48×10^{-7}	[30, 31]
γ_0^{t}	Coefficient for oxygen consumption	$\text{kg}/(\text{m}^3 \cdot \text{s})$	3.0×10^{-4}	[30, 31]
β	Parameter in the expression for Σ	$(-)$	0.5	[23]
$\varepsilon_{\text{n}}^{\text{t}}$	Parameter in the expression for Σ	$(-)$	0.8	[23]
ε_0^{t}	Parameter in the expression for Σ	$(-)$	1/3	[23]
k	Intrinsic permeability of the tumor tissue	m^2	1.8×10^{-15}	[136]
μ^{f}	Dynamic viscosity of IF	$\text{Pa} \cdot \text{s}$	1.0×10^{-3}	[167]
D^{ox}	Oxygen diffusion coefficient	m^2/s	3.2×10^{-9}	[167]
ρ	Density of the phases	$\text{kg}/(\text{m}^3)$	1.0×10^3	[167]
$\omega_{\text{crit}}^{\text{ox}}$	Critical oxygen mass fraction	$(-)$	2.0×10^{-6}	-
$\gamma_{\text{g}}^{\text{t}}$	Coefficient for cell proliferation	$\text{kg}/(\text{m}^3 \cdot \text{s})$	5.4×10^{-3}	-
$\gamma_{\text{n}}^{\text{t}}$	Coefficient for cell necrosis	$\text{kg}/(\text{m}^3 \cdot \text{s})$	1.5×10^{-1}	-
$\gamma_{\text{f}}^{\text{t}}$	Coefficient for cell lysis	$\text{kg}/(\text{m}^3 \cdot \text{s})$	1.15×10^{-2}	-
α	Parameter in the expression for Σ	Pa	1.0×10^5	-

[a]Value used for the simulations with compressed spheroids. Since the wells used to culture the spheroids are larger, a higher value for the available oxygen is considered

tumor center and to the fluid consumption induced by cell growth at the boundary.

The evolution of the oxygen mass fraction, the sole nutrient species considered here, is shown in Figure 3.4.b. Each line is plotted over the spheroid radius, every 5 days from the beginning of the simulation. As the spheroid grows, gradients of oxygen concentration develop from the tumor boundary to the center of the spheroid. After a few days the oxygen mass fraction reaches a plateau at the center of the tumor, with a value below the critical threshold $\omega_{\text{crit}}^{\text{ox}}$. This can be explained by considering that necrotic cells do not consume oxygen, and therefore do not alter the oxygen profile. Moreover, oxygen consumption is proportional to the amount of oxygen available through equation (3.22), and this contributes to a decreased slope in the curves towards the center of the spheroid.

Finally, the evolution of the necrotic mass fraction is presented in the graph of Figure 3.4.c. The necrotic portion of the tumor develops from the center towards the boundary. As the interface between living and necrotic TCs is diffuse, the separation between the two is smooth and the model can account for perinecrotic regions.

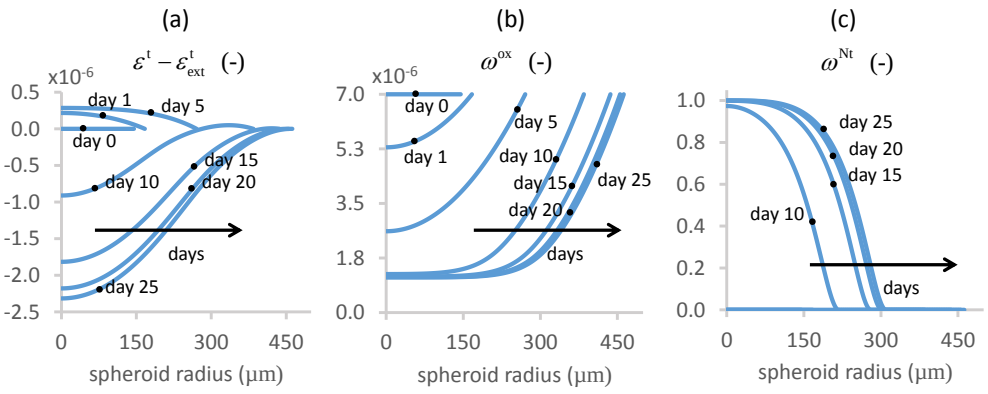

Figure 3.4: **a** Volume fraction of tumor cells, plotted as the difference between the volume fraction inside the spheroid and at the spheroid boundary (here, $\varepsilon^t_{ext} = \varepsilon^t_n$, since the spheroids are not compressed). **b** Mass fraction of oxygen. **c** Mass fraction of necrotic tumor cells. All the variables are plotted over the spheroid radius with each line drawn every five days from the beginning of the simulation.

3.1.4.2 Spheroids grown with different initial cell densities

The computational model is validated against data from tumor spheroid cultures. U87-MG cells, a human glioblastoma cell line, are cultured with a standard protocol (see Section 3.1.3). The experimental set up is shown in Figure 3.5. The bottom of standard cell culture wells is covered with agarose, in order to prevent adhesion of tumor cells. Cells are seeded at different initial numbers (1000, 5000, 10000) and rapidly form spheroids suspended in standard culture medium. The evolution of the spheroid radii is then recorded over time via optical microscopy and the resulting growth curves are plotted in Figure 3.6.a. It is possible to distinguish between the first stages of growth, characterized by an exponential/linear behavior, followed by a phase of growth saturation where the radius reaches a steady value.

After recording the curves, a series of simulations is run to reproduce the experimental data. The growth curves corresponding to the best fit of the experimental data are shown in Figure 3.6.b. The governing parameters are taken from literature when they are available and we use the same order of magnitude of the experimental values when they refer to other cell species. Table 3.1 lists the parameters used in this study together with the ones determined by the fit of the curves. There is a good agreement with the experimental data, for all the three different initial cell seeding numbers. The model captures the growth dynamics both in the first fast-growing

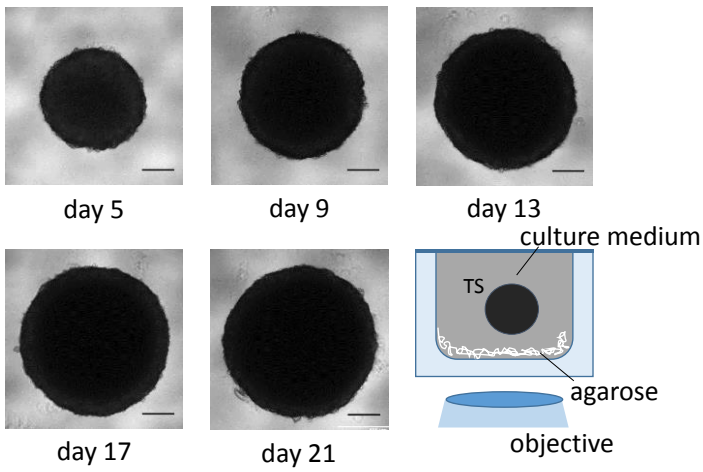

Figure 3.5: Optical images for the growth of U-87MG spheroids from day 5 to day 21. The scale bar is 200 μm, and the spheroids are taken from the 10000 seeded cells initial condition. The last image represents a scheme of the culture protocol.

phase and in the later phase of growth saturation. Note that the same parameters are used for fitting all the three curves and only the initial radii of the spheroids are changed, showing a good quality of the fit.

This experiment is useful for validating the model and displays a second remarkable result. The different initial seeding of tumor cells affects the initial radius of the tumor spheroid, which increases from about 100 μm to almost 190 μm. The data show that, although being constituted by a larger initial number of tumor cells, bigger spheroids reach the same final radius of smaller ones. This result agrees with what is reported in literature about the existence of a steady radius for growing spheroids [181, 55, 27, 59], which in our case takes approximately the value of 475 μm. Interestingly, the model reproduces the same behavior of the experiments with the steady state being reached after 25 days from cell seeding. As the spheroids grow freely in the culture medium, the only mechanism to stop cell proliferation is given by equations (3.23) and (3.25), in which it is assumed that cell mitosis and necrosis depend only on the local level of nutrient. Therefore, in this modeling framework, the hypothesis of nutrient deprivation is sufficient to explain the phenomenon of growth saturation and the existence of an asymptotic radius for the spheroid.

As a further remark about these results, in Figure 3.6.c the previous curves are shifted of the proper amount with respect to the different initial conditions. It is

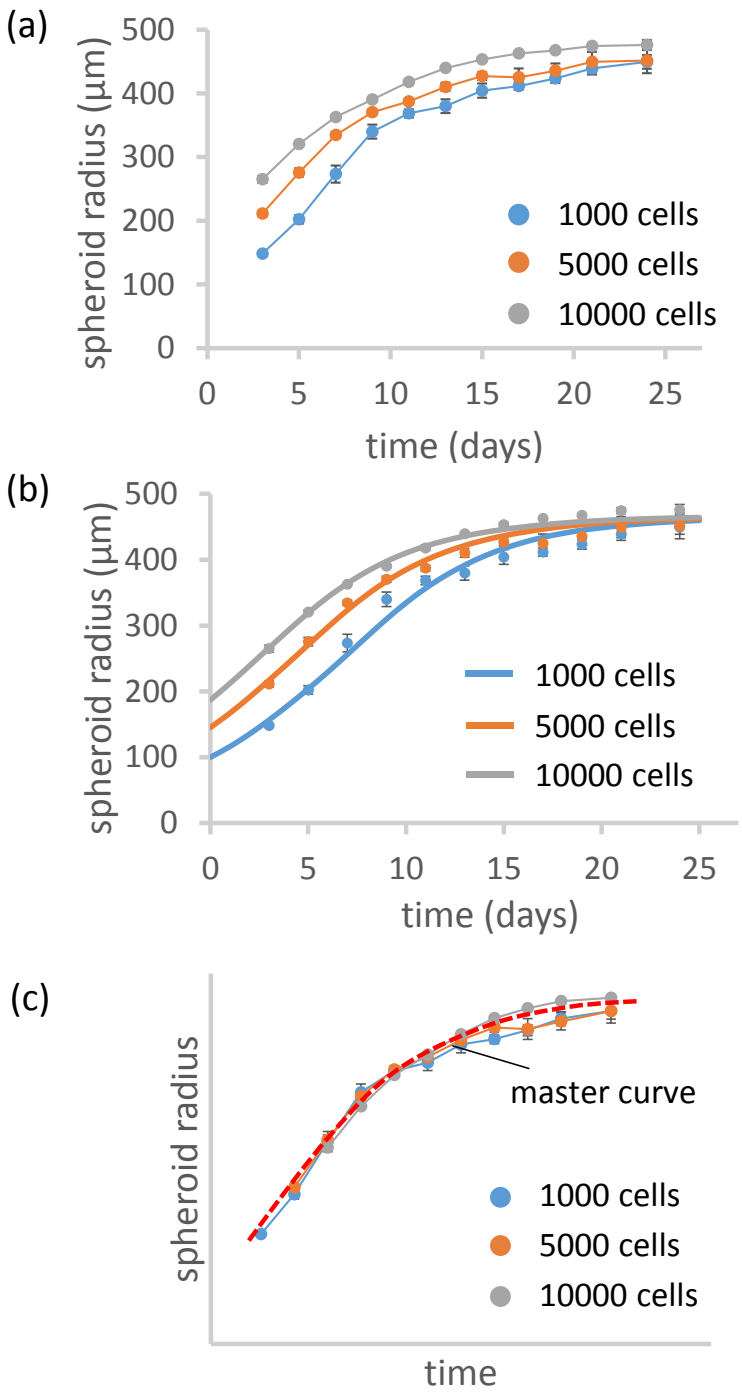

Figure 3.6: Growth curves recorded from the free growth experiments. **a** Each curve represents a different initial condition in terms of seeded cells. N $\geq$ 4 spheroids are considered for each condition. Points are experimental data, error bars are the standard deviations of the measurements. **b** Solid lines result from fits with the mathematical model. **c** Growth curve obtained by superimposing the evolution of the radii of spheroids grown from different initial cell seeding numbers.

interesting to see that they coalesce to a single *master curve*. Spheroids grown from a different initial radius follow the same curve, showing that there exists a common dynamics regulating the growth of these cellular aggregates.

3.1.4.3 Compression experiments

The application of a constant mechanical stress on the surface of the growing spheroids is investigated in the following experiments. Addition of Dextran to the cell culture medium produces an osmotic pressure on the outermost layer of cells located on the spheroid surface. The osmotic pressure acts as a network stress directed to decrease the volume occupied by the spheroids [128, 129, 46]. This compressive force can be calibrated experimentally as in [18, 20]. An empirical law is then provided to relate the concentration of Dextran in the solution to the external pressure exerted on the surface of the spheroids. Three pressure conditions are explored following the approach described in Section 3.1.3, namely 1 kPa, 5 kPa and 10 kPa, plus a control experiment (CTRL) with no external pressure. Cell viability is checked as reported in Section 3.1.3, in which it is shown that the addition of Dextran does not alter cell death or growth. The results are presented in Figure 3.7, where the growth of the spheroids is followed for 18 days after the addition of Dextran. Figure 3.7.a shows optical images of sample spheroids referring to the control and to the most compressed condition for different time instants. Starting from a similar initial radius (about 200 μm), the two spheroids reach considerable different volumes at day 18. It is possible to observe that the compressed spheroid grows to a lesser extent compared to the stress free case.

The growing curves for the other external applied pressures are collected in Figure 3.7.b. The highest value for the radius is reached in the spheroids grown in the absence of any external compression. When Dextran is added to the medium and the osmotic stress builds up, both the growth rate and the final diameter decrease. If the applied pressure is released, the growth of the aggregates resumes. This suggests that the effect of the stress is reversible (see Figure 3.8), as shown in the seminal work of Helmlinger [83]. The effect of the external pressure on the growth of the spheroid is included in the model through equation (3.24), which describes the inhibition of cell proliferation due to the applied mechanical stress on the tumor cells. The most common mathematical expressions for the inhibiting function reported in literature are based on linear or inversely proportional assumptions [159, 23, 98, 131]. These forms are tested against the experimental data in Figure 3.9, together with an exponential relation and a MichaelisMenten-like expression. The data in Table 3.2

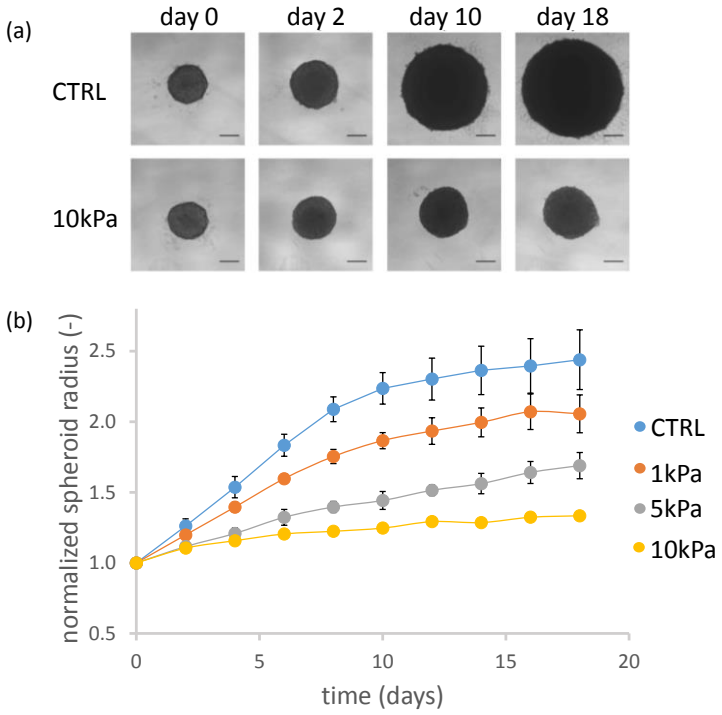

Figure 3.7: **a** Optical images of U-87MG spheroids grown under the effect of the Dextran solutions. The first row shows the control experiments and the second row a spheroid under the highest compression. The scale bar is 200 μm, and the initial seeding is 5000 tumor cells. **b** Experimental results for the compression experiments. The points are the experimental data, the error bars represent the standard deviations of the measurements. For each condition, N = 5 spheroids are considered.

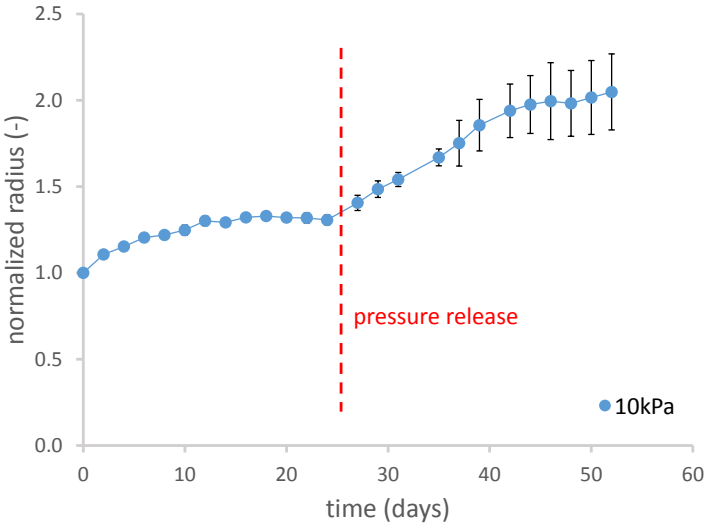

Figure 3.8: Growth curve for the spheroids under the highest compression, monitored over 52 days. The points are the experimental data and the error bars represent the standard deviations of the measurements. The red dashed line indicates the time instant when the external stress is removed from the spheroids. After the stress release, the spheroids resume their growth.

represent the values of the parameters that provide the best fits to the experimental curves. The linear relationship, applied in Figure 3.9.a, underestimates the inhibition effect for low compressions, leading to larger values of the radius for the 1 kPa and 5 kPa cases. At the same time, for larger compressions the linear relationship gives overestimates for the inhibition, resulting in smaller radii for the 10 kPa curve than experimentally measured. The exponential relationship is applied in Figure 3.9.b, in which it is possible to observe an improvement for high compressions but a similar underestimation for the 1 kPa and 5 kPa curves. Another improvement can be seen in Figure 3.9.c, referring to the inversely proportional expression. In this case there is a good agreement with the experimental data for all the curves, except for the 1 kPa case. The best results are obtained with the Michaelis-Menten-like law, represented in Figure 3.9.d. All the different compression levels are well described by the model, together with the final radii reached by the spheroids.

3.1.4.4 Effect of the growth inhibition parameters

The effect of an external stress acting on the cellular component of the spheroid can be evaluated through a parametric study on the growth inhibition parameters

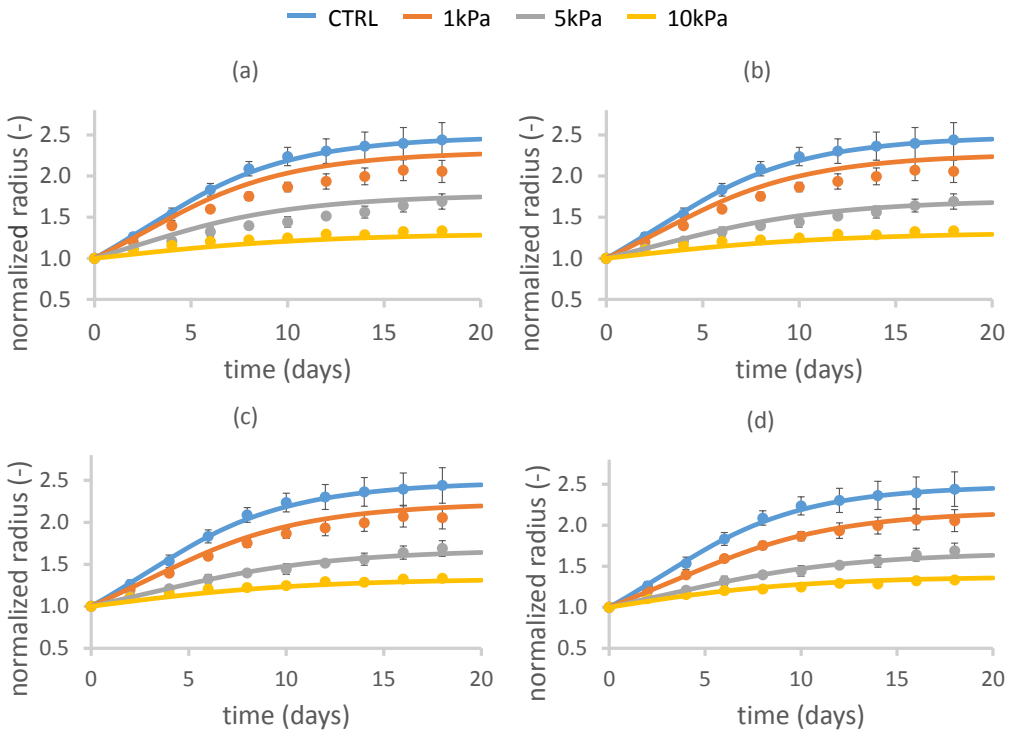

Figure 3.9: Fit of the experimental data for the compression experiments. Results from the linear (**a**), exponential (**b**), inversely proportional (**c**), and Michaelis-Menten-like (**d**) assumptions for the function H in Equation (3.24).

Table 3.2: Different mathematical expressions for the growth inhibition function in Equation (3.24).

Growth inhibition	Mathematical expression	δ_1	δ_2
Linear	$H = 1 - \delta_1 \langle \Sigma \rangle_+$	7.38×10^{-5} 1/Pa	-
Exponential	$H = \exp(-\delta_1 \langle \Sigma \rangle_+)$	1.30×10^{-4} 1/Pa	-
Inversely proportional	$H = 1/(1 + \delta_1 \langle \Sigma \rangle_+)$	2.27×10^{-4} 1/Pa	-
Michaelis-Menten-like	$H = 1 - \delta_1 \langle \Sigma \rangle_+ / (\delta_2 + \langle \Sigma \rangle_+)$	7.13×10^{-1} -	1.54×10^3 Pa

δ_1 and δ_2 of equation (3.24). The growth curves obtained by varying one of the two parameters and keeping the other fixed for the case of an external pressure of 5 kPa are presented in Figure 3.10. The two solid lines represent reference values assumed

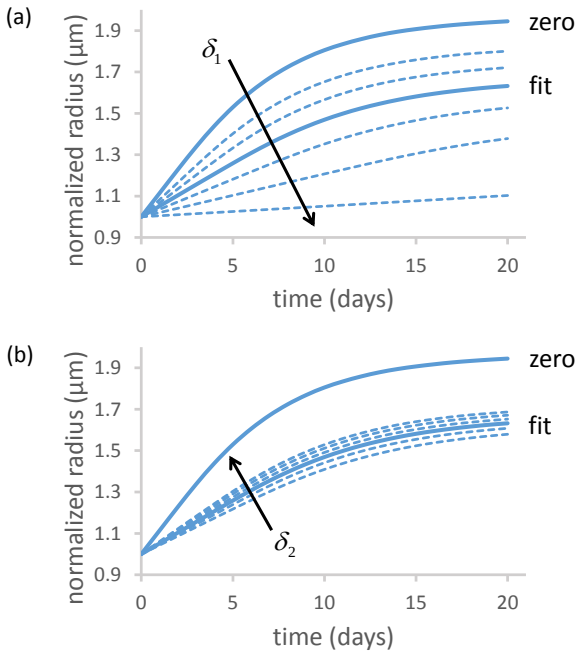

Figure 3.10: Parametric study for the growth inhibition parameters in Equation (3.24). Effects of δ_1 (**a**) and of δ_2 (**b**) on the growth of the spheroids.

by the parameters. In particular, "zero" indicates the curve obtained by setting both δ_1 and δ_2 to zero, while "fit" is the curve obtained with the values in Table 3.2. The effect of different values for δ_1 is shown in Figure 3.10.a. The arrow points in the direction of increasing δ_1, while for δ_2 we take the value in Table 3.2. From the top curve to the bottom one we consider values for δ_1 that are, respectively, -50, -25, +25,

+50 and +75% of the reference value in Table 3.2. As δ_1 increases, tumor cells sense more the effect of external stresses on their proliferation. This results in smaller final radii of the spheroids and in slower growth rates. If the value of δ_1 is sufficiently high, then the tumor starts to shrink and an equilibrium radius no longer exists.

The same investigation, this time for δ_2, is reported in Figure 3.10.b. In this case, the arrow points in the opposite direction, indicating that an increase in δ_2 leads to an increase of the final radius. This difference can be easily explained by considering that H in equation (3.24) is directly proportional to δ_1 and inversely proportional to δ_2. However, it is possible to note that the effect of varying δ_2 is less pronounced on the growth curve, since its reference value in Table 3.2 is much smaller than the pressures in the compression experiments.

These results indicate collectively a double effect of the external environment in limiting the growth of the tumor. Tumor growth may be hindered by nutrient deprivation, but also by external stresses exerted by regions close to the tumor.

3.1.5 Conclusions

In the present study, a recent model for tumor growth has been extended to describe the evolution of tumor spheroids. A set of experiments is carried out and the resulting data are compared to numerical predictions. The experimental growth curves validate the model equations both for the free-growth case, in which the cells are cultured in three dimensions in standard culture medium, and for the mechanically compressed setup, in which the spheroids are subjected to an external pressure. In addition to providing the data for the validation, the first series of experiments highlights the existence of a *master curve* (Figure 3.6.c). This common growth trend supports the hypothesis of describing the cell aggregates as a dynamical system, which behavior can be predicted, at least as a first approximation, by the laws of mechanics. The results of the model in terms of tumor volume fraction, oxygen mass fraction and necrotic mass fraction are reported and appear in line with the results of the original model in [167]. The second set of experiments about spheroids compression extends the work in [46] by adding another cancer cell species (U87-MG) to their study. The observed evolution curves are similar to their findings and confirm the hypothesis of an inhibitory effect of external stress on cancer cell proliferation. Regarding the description of this phenomenon, the experimental data are exploited to design a constitutive relationship that performs better, compared to the existing laws, in describing the evolution of the system.

Several simplifying assumptions are considered in the work and the model is certainly open to further improvements. In particular, here only one nutrient species, namely oxygen, diffuses in the interstitial fluid and regulates the proliferation of tumor cells. Although the action of other chemicals is implicitly included in the mass transfer term in (3.19), modeling additional nutrients, growth and necrosis factors could provide supplementary insights into the evolution of the tumor system [34, 91]. Another point that should be addressed is the choice of the constitutive relations used to close the differential system. Most of these laws, as it happens frequently in literature, are derived from phenomenological arguments and deserve more experimental work to be linked to the biology of what they are describing. In particular, here it is assumed that the compression of the spheroids induces inhibition of cell growth, without modifying the apoptosis rate of the cells. This hypothesis is still a matter of debate in literature - see for example [129] and comments therein. Here, it is adopted to account for the experimental observations in [46], in which the experimental setup is similar to the one in this work. A systematic comparison of different compression modalities may improve the understanding of this phenomenon and the design of more accurate constitutive laws. Finally, here a very simple mechanical description of the tumor ensemble is considered, function of the volume fraction of the tumor cells. This assumption provides a great simplification of the mechanical equations and describes accurately the data, however it does not take into account several phenomena related to the stress experienced by the cells inside the tumor tissue. For example, viscous effects existing at smaller time-scales than cell proliferation are neglected, as well as cellular adhesion bonds breakage and formation during the evolution of the tumor mass [6, 150].

As a possible development of the current work, we plan to perform further experiments. These will provide better estimates for the model parameters and, as new data will be collected, will provide quantities that could be compared to the output of the model equations. A part of the future experimental work will be also devoted to the biochemical understanding of the growth inhibition process due to mechanical stress. Even if some work is already present in literature [46, 54], many details remain obscure as well as a proper implementation of the phenomena in the growth equations.

A better description of the interactions between the tumor and its external microenvironment (biochemical and mechanical) may contribute to the understanding of the disease progression, and to the design of new therapeutic treatments.

3.2 Model analysis through a parametric study

3.2.1 Introduction

In Section 3.1, we specialize the modeling framework in [167] for tumor spheroids. A set of experiments on U-87 spheroids is carried out to validate the equations and test new constitutive relations. Comparison with experiments is performed both with spheroids freely suspended in the culture medium and subjected to different mechanical loads.

Even though the model is simplified with respect to the original work, it still retains a significant degree of complexity. The equations are strongly coupled, nonlinear effects arise, and understanding the role of the different parameters appears to be difficult. For example, in the previous Section, it is not clear which model parameters have a significant effect on the growth of the spheroids.

Here, we perform a parametric analysis on a set of governing coefficients appearing in the model equations. We test the effect of parameter variation on the spheroid growth curve and in particular on the final radius reached by the cell aggregate. Finally, we provide a discussion of the results and summarize our findings in the conclusions.

3.2.2 Summary of the mathematical model

Here, we recall briefly the equations derived in the previous section. The tumor tissue is modeled as a biphasic porous medium, composed of the following constituents, or phases: (i) the tumor cells (TCs), which are divided into living (LTCs) and necrotic (NTCs) cells, and (ii) the interstitial fluid (IF). In the language of porous media theory, the union of TCs and extracellular matrix (ECM) constitutes the solid skeleton of the system, whereas the IF represents the fluid phase permeating the pores. The IF carries nutrients, growth factors and waste products. For the sake of simplicity, we consider only one nutrient in our model, namely oxygen (ox), which diffuses in the IF and is consumed by LTCs. Adequate levels of nutrient are necessary for cell proliferation, otherwise they start necrosis and lysis. Finally, we assume cell duplication to be influenced by the local level of mechanical stress, with cells proliferating poorly when

Section 3.2 of this chapter is based upon the work in: Mascheroni P, Boso D P, Stigliano C, Carfagna M, Preziosi L, Decuzzi P, Schrefler B A (2016), "A parametric study of a multiphase porous media model for tumor spheroids and environment interactions", *VII European Congress on Computational Methods in Applied Sciences and Engineering - ECCOMAS 2016*, ECCOMAS Proceedings.

subjected to compression. In the following, t and f will denote quantities related to the solid and fluid part of the biphasic system, respectively.

We denote the volume fractions of the solid and the fluid by ε^{t} and ε^{f}, respectively. We assume that the fluid permeates completely the voids left by the solid skeleton, and apply the saturation constraint:

$$\varepsilon^{\mathrm{t}} + \varepsilon^{\mathrm{f}} = 1. \tag{3.40}$$

Then, we write the governing equations for the tumor cell volume fraction (ε^{t}), the interstitial fluid pressure (p^{f}), the oxygen mass fraction (ω^{ox}) and the necrotic cell mass fraction (ω^{Nt}). Below, we report the balance laws as appear for the tumor spheroid growth case. We refer the interested reader to Section 3.1.2 for the full derivation. In particular, we solve the system of equations given by:

$$\frac{\partial \varepsilon^{\mathrm{t}}}{\partial t} - \frac{1}{r^2}\frac{\partial}{\partial r}\left(r^2 \varepsilon^{\mathrm{t}} \frac{k}{\mu^{\mathrm{f}}} \Sigma' \frac{\partial \varepsilon^{\mathrm{t}}}{\partial r}\right) - \frac{1}{\rho}\left(\Gamma_{\mathrm{gr}}^{\mathrm{f}\to\mathrm{t}} - \Gamma_{\mathrm{ly}}^{\mathrm{t}\to\mathrm{f}}\right) = 0, \tag{3.41}$$

$$\frac{\partial \left(\omega^{\mathrm{Nt}} \varepsilon^{\mathrm{t}}\right)}{\partial t} - \frac{1}{r^2}\frac{\partial}{\partial r}\left(r^2 \omega^{\mathrm{Nt}} \varepsilon^{\mathrm{t}} \frac{k}{\mu^{\mathrm{f}}} \Sigma' \frac{\partial \varepsilon^{\mathrm{t}}}{\partial r}\right) - \frac{1}{\rho}\left(\varepsilon^{\mathrm{t}} r^{\mathrm{Nt}} - \Gamma_{\mathrm{ly}}^{\mathrm{t}\to\mathrm{f}}\right) = 0, \tag{3.42}$$

$$\begin{aligned}\frac{\partial \left[\left(1-\varepsilon^{\mathrm{t}}\right)\omega^{\mathrm{ox}}\right]}{\partial t} &+ \frac{1}{r^2}\frac{\partial}{\partial r}\left(r^2 \omega^{\mathrm{ox}} \varepsilon^{\mathrm{t}} \frac{k}{\mu^{\mathrm{f}}} \Sigma' \frac{\partial \varepsilon^{\mathrm{t}}}{\partial r}\right) \\ &- \frac{1}{r^2}\frac{\partial}{\partial r}\left[r^2 \left(1-\varepsilon^{\mathrm{t}}\right) D^{\mathrm{ox}} \frac{\partial \omega^{\mathrm{ox}}}{\partial r}\right] + \frac{1}{\rho}\Gamma_{\mathrm{ox}}^{\mathrm{ox}\to\mathrm{t}} = 0.\end{aligned} \tag{3.43}$$

Here r is the radial coordinate over the spheroid radius; k is the intrinsic permeability of the solid matrix; μ^{f} is the dynamic viscosity of the IF; D^{ox} is the diffusion coefficient of oxygen; and ρ is the density of the phases. As described in detail in Section 3.1.2, Σ is a quantity relating the mechanical stress in the tumor to the solid volume fraction. In the equations above we make use of Σ', the derivative of Σ with respect to ε^{t}. This quantity can be computed analytically from the expression reported in Section 3.1.2, Equation (3.17).

The mass exchange terms appearing in equations (3.41)-(3.43) have the form:

$$\Gamma_{\mathrm{gr}}^{\mathrm{f}\to\mathrm{t}} = \gamma_{\mathrm{g}}^{\mathrm{t}} \left\langle \frac{\omega^{\mathrm{ox}} - \omega_{\mathrm{crit}}^{\mathrm{ox}}}{\omega_{\mathrm{env}}^{\mathrm{ox}} - \omega_{\mathrm{crit}}^{\mathrm{ox}}} \right\rangle_{+} H\left(\Sigma\right) \omega^{\mathrm{Lt}} \varepsilon^{\mathrm{t}}, \tag{3.44}$$

$$\Gamma_{\mathrm{ly}}^{\mathrm{t}\to\mathrm{f}} = \gamma_{\mathrm{f}}^{\mathrm{t}} \omega^{\mathrm{Nt}} \varepsilon^{\mathrm{t}}, \tag{3.45}$$

$$\varepsilon^{\mathrm{t}} r^{\mathrm{Nt}} = \gamma_{\mathrm{n}}^{\mathrm{t}} \left\langle \frac{\omega_{\mathrm{crit}}^{\mathrm{ox}} - \omega^{\mathrm{ox}}}{\omega_{\mathrm{env}}^{\mathrm{ox}} - \omega_{\mathrm{crit}}^{\mathrm{ox}}} \right\rangle_{+} \omega^{\mathrm{Lt}} \varepsilon^{\mathrm{t}}, \tag{3.46}$$

$$\Gamma_{\mathrm{ox}}^{\mathrm{ox}\to\mathrm{t}} = \gamma_{0}^{\mathrm{t}} \frac{\omega^{\mathrm{ox}}}{\omega^{\mathrm{ox}} + c_{\mathrm{ox}}} \omega^{\mathrm{Lt}} \varepsilon^{\mathrm{t}}. \tag{3.47}$$

Here $\gamma_{\mathrm{g}}^{\mathrm{t}}$, $\gamma_{\mathrm{f}}^{\mathrm{t}}$, $\gamma_{\mathrm{n}}^{\mathrm{t}}$ and γ_{0}^{t} are coefficients that account for the nutrient and IF mass that becomes tumor due to cell growth; the degradation of cellular membranes and the following mass conversion into IF; the rate of cell death; and the oxygen uptake rate in the tumor, respectively. The quantity $\omega^{\mathrm{Lt}} = 1 - \omega^{\mathrm{Nt}}$ represents the mass fraction of LTCs, and guarantees that growth, death and oxygen uptake are active only on the living portion of the spheroid. The Macaulay brackets $\langle\cdot\rangle_{+}$ appearing in Equations (3.44) and (3.46) return the positive value of their argument. Since the oxygen mass fraction inside the spheroid is equal or smaller than its environmental level in the culture medium $\omega_{\mathrm{env}}^{\mathrm{ox}}$, the brackets in equation (3.44) will return a value between unity (for $\omega^{\mathrm{ox}} = \omega_{\mathrm{env}}^{\mathrm{ox}}$) and zero (for $\omega^{\mathrm{ox}} \leq \omega_{\mathrm{crit}}^{\mathrm{ox}}$). Note that here $\omega_{\mathrm{crit}}^{\mathrm{ox}}$ is the oxygen threshold level below which cell proliferation is inhibited. Equation (3.45) describes cell lysis occurring in the NTCs, whereas a consideration similar to the one for Equation (3.44) holds true for equation (3.46), which describes TC death due to the lack of nutrient. Finally, Equation (3.47) describes the uptake of oxygen by LTCs and accounts for the dependence of nutrient consumption on its local level. Here c_{ox} is the oxygen mass fraction at which oxygen consumption is reduced by half. Note that the function H in Equation (3.44) describes the inhibition of cell proliferation due to the mechanical stress exerted on the TCs. Even though several alternatives are given in the literature, in Section 3.1.4 we provide a mathematical expression for this quantity that is able to describe accurately our experimental observations on spheroid growth under a controlled external compression. Accordingly, in the following we set:

$$H = 1 - \frac{\delta_1 \langle \Sigma \rangle_{+}}{\delta_2 + \langle \Sigma \rangle_{+}}. \tag{3.48}$$

We model the growth of the spheroid as a free-boundary problem, where the interface constituted by the TCs moves with velocity v^{t}, given by:

$$\frac{dR}{dt} = v^{\mathrm{t}} = -\frac{k}{\mu^{\mathrm{f}}} \Sigma' \frac{\partial \varepsilon^{\mathrm{t}}}{\partial r}\bigg|_{r=R}, \tag{3.49}$$

with R being the external radius of the spheroid. The closed form of the differential problem is obtained by defining a set of boundary and initial conditions. In particular, spherical symmetry requires no-flow boundary conditions at the spheroid center, while we assume Dirichlet boundary conditions on the tumor external surface:

$$\frac{\partial \varepsilon^{\mathrm{t}}}{\partial r} = \frac{\partial \omega^{\mathrm{Nt}}}{\partial r} = \frac{\partial \omega^{\mathrm{ox}}}{\partial r} = 0, \quad \text{in } r = 0, \tag{3.50}$$

$$\varepsilon^{\mathrm{t}} = \varepsilon_{\mathrm{ext}}^{\mathrm{t}}, \quad \omega^{\mathrm{Nt}} = 0, \quad \omega^{\mathrm{ox}} = \omega_{\mathrm{env}}^{\mathrm{ox}}, \quad \text{in } r = R. \tag{3.51}$$

Finally, we assume the following initial conditions over the spheroid radius:

$$\varepsilon^{\mathrm{t}} = \varepsilon_{\mathrm{ext}}^{\mathrm{t}}, \quad \omega^{\mathrm{Nt}} = 0, \quad \omega^{\mathrm{ox}} = \omega_{\mathrm{env}}^{\mathrm{ox}}, \quad \text{for } 0 < r < R \text{ at } t = 0. \tag{3.52}$$

3.2.3 Results and discussion

In Section 3.1.4, we have performed numerical simulations of the Equations in (3.41)-(3.43) and we have recorded the resulting growth curves, namely the evolution of the spheroid radius over time. We have analyzed both the case of spheroids freely growing in their culture medium, and the case where an external compression is applied. The values of the governing parameters are obtained from the literature, when they are available, and from the fit of the experimental curves.

Here, we investigate the dependence of the growth curves on a set of these parameters, summarized in Table 3.3. We start our analysis from R_0, the initial radius of the spheroid. In Figure 3.11 we report the behavior of the growth curve for different initial spheroid radii. Note that in all the following figures the curve in red is the one corresponding to the reference value in Table 3.3. We consider spheroids with initial radii of 90, 117.5, 145, 172.5 and 200 μm. For all the different conditions, in particular for the small initial radii, it is possible to visualize the three stages characterizing the growth of the spheroids [181, 27, 59]: the exponential phase in the first days of growth, where the cells proliferate in a nutrient-rich environment; the linear phase, where the the tumor mass becomes larger and the nutrient starts to run low; and the growth saturation phase, where a significant portion of the spheroid is necrotic and only a small rim of cell proliferates at the tumor border. Notably, although the spheroids with the larger initial radii are comprised of more tumor cells than the others, they reach a similar final radius, of about 475 μm. This behavior is consistent with our assumption of growth as limited by nutrient deprivation. For a fixed level of external oxygen ($\omega_{\text{env}}^{\text{ox}}$), only a fixed number of TCs is allowed to coexist in the spheroid mass. This condition is met sooner for the spheroids with larger initial radii and later for the others, as shown in the curves and observed experimentally in Section 3.1.4.

Table 3.3: Parameters considered in this study. The reference value is the one used in Section 3.1.4.

Symbol	Parameter	Reference value	Unit
R_0	Initial radius of the spheroid	145	μm
$\omega_{\text{crit}}^{\text{ox}}$	Critical mass fraction of oxygen	2.0×10^{-6}	-
$\gamma_{\text{g}}^{\text{t}}$	Coefficient related to growth	5.4×10^{-3}	kg/(m$^3 \cdot$ s)
$\gamma_{\text{n}}^{\text{t}}$	Coefficient related to necrosis	1.5×10^{-1}	kg/(m$^3 \cdot$ s)
$\gamma_{\text{f}}^{\text{t}}$	Coefficient related to lysis	1.15×10^{-2}	kg/(m$^3 \cdot$ s)
α	Coefficient in the definition of Σ	1.0×10^{5}	Pa

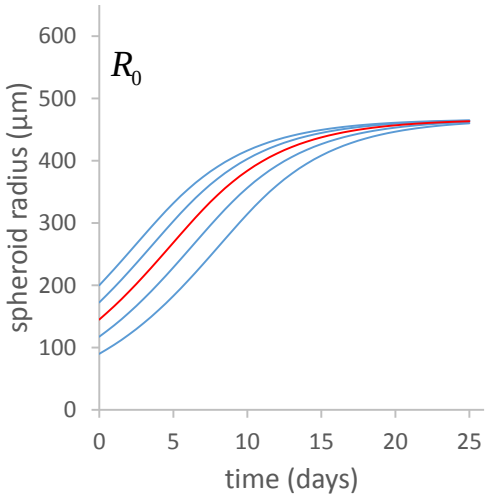

Figure 3.11: Spheroid growth curves for different initial radii.

Next, we study the effect of a variation in the critical level of oxygen $\omega_{\text{crit}}^{\text{ox}}$. The resulting growth curves are shown in Figure 3.12. We consider values for $\omega_{\text{crit}}^{\text{ox}}$ of 1.0×10^{-6}, 2.0×10^{-6}, 3.0×10^{-6}, 4.0×10^{-6}, 5.0×10^{-6} and 6.0×10^{-6} (the black arrow points in the direction of increasing values of $\omega_{\text{crit}}^{\text{ox}}$; this holds true also for the following figures, in which the black arrow indicates increasing values of the investigated parameter). The choice of this parameter affects significantly the final radius reached by the spheroids. In particular, higher values of the critical level of oxygen provide smaller final radii. This follows from the modeling choice in Equation (3.44), where cell proliferation is a linear function of the oxygen critical level. If this threshold value is high when compared to the external mass fraction of oxygen, only a small portion of the spheroid is able to proliferate and the final radius is reduced.

The next parameter that we consider is the growth coefficient $\gamma_{\text{g}}^{\text{t}}$. In Figure 3.13, we consider values of this coefficient that are ± 25, ± 50 and $\pm 75\%$ of the reference value. Also for this parameter, the final radius reached by the spheroid strongly depends on its value. Interestingly, $\gamma_{\text{g}}^{\text{t}}$ seems to regulate the time scale of the phenomenon. For small values of the growth coefficient, at the end of the simulations the spheroid is still in the first stages of growth. On the contrary, for higher values of $\gamma_{\text{g}}^{\text{t}}$ the spheroid reaches faster its final radius. We also observe that the steady radius increases for increasing values of the growth coefficient. Indeed, growth saturation is established when the net production of new tumor mass is zero. This means that, in a given time interval, the number of new cells produced by growth has to be equivalent to the number of cells undergoing lysis. This number is approximately given by the

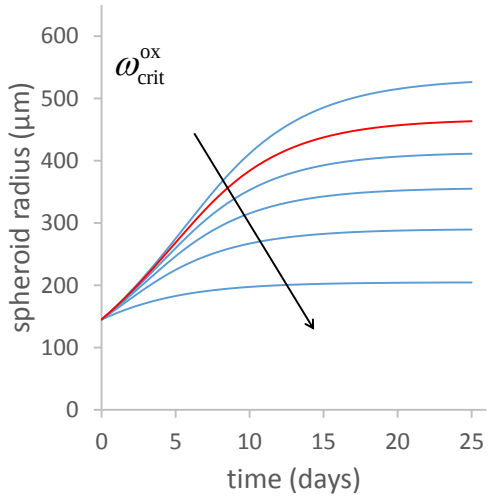

Figure 3.12: Spheroid growth curves for different critical levels of oxygen.

number of necrotic cells times the lysis rate. If the lysis rate is fixed, as in the present case, and the growth coefficient is increased, there is a net production of TCs and the radius grows further. To reach a new steady condition, the necrotic core of the spheroid has to increase in size, so that the number of cells undergoing lysis is again equal to the number of generated TCs. This idea can be tested through a variation of the parameters that regulate cell death, namely γ_n^t and γ_f^t, together with a consistent variation of the growth coefficient γ_g^t. If we double each of these constants at the same time, we expect the steady radius of the spheroid to be unaltered, since we have maintained the original ratio between cell production and removal. This condition is shown in Figure 3.13, by the gray dashed line. Note that the final radius is the same as the one obtained with the reference value, but now the time needed to reach the steady state is significantly reduced.

Then, we consider the case of a variation in the coefficient γ_n^t, regulating the necrosis of the LTCs. The influence of this parameter is shown in Figure 3.14. For this coefficient, we analyze values that are ± 25, ± 50 and $+75\%$ of the reference value. As shown in the Figure, the variation of γ_n^t has a very little effect on the resulting growth curves. The shape of the curve is not significantly altered and the final radius has a variation of less than 5%. This is probably due to the fact that this term is active on a population of TCs that is still alive, but is located in a region of the spheroid where the nutrient level is below the critical threshold. This condition is poorly encountered in the spheroids at this stage of their growth [127], resulting in the small influence of this parameter.

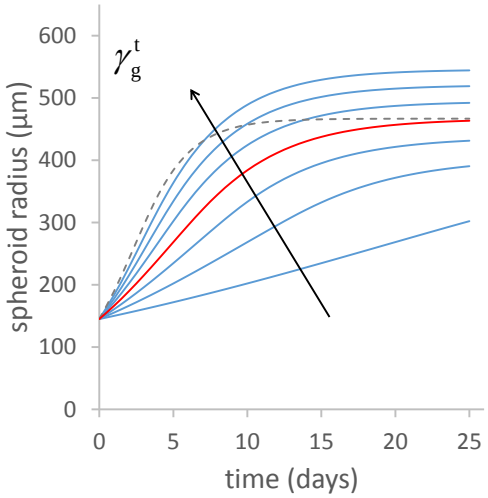

Figure 3.13: Spheroid growth curves for different values of the growth coefficient.

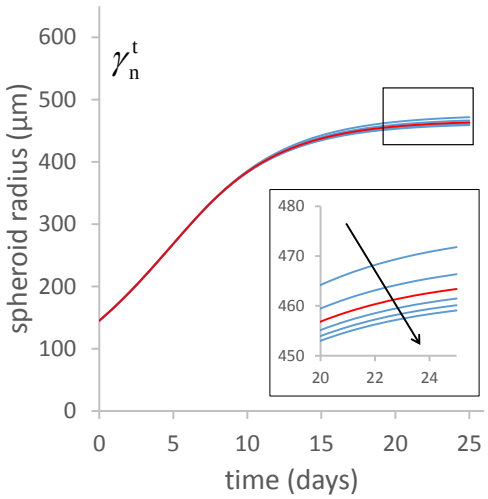

Figure 3.14: Spheroid growth curves for different values of the necrosis coefficient.

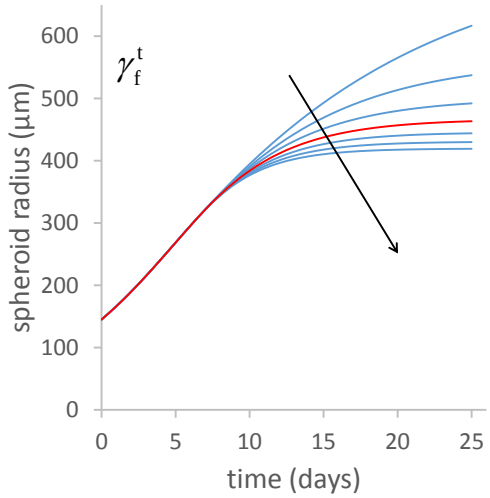

Figure 3.15: Spheroid growth curves for different values of the lysis coefficient.

The fifth parameter that we study is the lysis coefficient γ_f^t. Figure 3.15 shows the results of considering values for this parameter that are ± 25, ± 50 and $\pm 75\%$ of its reference value. We first observe that the effects of varying the parameter only appear after day 8. This is consistent with the onset of a necrotic population inside the spheroid, which occurs after a few days from the beginning of the simulation. Figure 3.15 shows that the value of the lysis coefficient has a significant impact on the spheroid final radius. Notably, there is a saturation effect for high values of γ_f^t. This may be due to the limited amount of NTCs that exists in the necrotic core at fixed γ_n^t, and that can therefore undergo lysis.

Finally, we study the effects of varying α in the mathematical expression for Σ. The value of the derivative Σ' is directly proportional to this parameter, as shown in Section 3.1.2. We vary the value of α for the ± 25, ± 50 and $\pm 75\%$ with respect to its reference value. Even though we apply a significant variation, there is no apparent effect in the growth curves, which appear superimposed. This finding may point to the fact that the dynamics of the system, at least for the set of parameters considered, are mainly governed by the constitutive relations for the mass exchange between the phases.

3.2.4 Conclusions

In this Section, we have performed a parametric study on a mathematical model for tumor spheroid growth that was presented in Section 3.1. The influence of a set of

parameters on the growth curves of the spheroids has been evaluated, and we have provided a discussion of the results. In summary, some of the parameters show a little effect on the growth dynamics, such as the mechanical coefficient α and the coefficient related to necrosis $\gamma_{\mathrm{n}}^{\mathrm{t}}$. On the other hand, other parameters have a significant impact on the final radius reached by the spheroids, namely the critical oxygen mass fraction $\omega_{\mathrm{crit}}^{\mathrm{ox}}$, the coefficient related to growth $\gamma_{\mathrm{g}}^{\mathrm{t}}$ and the coefficient related to lysis $\gamma_{\mathrm{f}}^{\mathrm{t}}$.

3.3 Effects of anticancer treatments

3.3.1 Introduction

A major hurdle to chemotherapy success is resistance of tumor cells to therapeutic agents. In general, resistance may arise as an intrinsic cellular response or as a result of drug treatment [198]. It is known that the presence of a low-proliferating cell population is one of the leading factors contributing to drug resistance in solid tumors [132, 184]. In fact, several chemotherapeutic agents are effective against rapidly dividing cells. Moreover, as certain normal tissues display high rates of cellular divisions (such as the gut mucosal and bone marrow cells), there exists a toxicity limit determining the maximum administrable drug dose [43].

Such resistance mechanisms, dependent on the proliferative activity of tumor cells, are generally investigated *in vitro* through the use of tumor spheroids [185]. Contrary to conventional monolayer cultures, tumor spheroids display heterogeneous cell populations, including quiescent and necrotic cells, together with resistant phenomena to different chemotherapeutic drugs [127]. Cell quiescence results both from the lack of nutrients and growth factors within the tumor, and from adhesion interactions between cells of the same type. Indeed, cells from healthy tissues display a mechanism of *contact inhibition* that regulates proliferation in a crowded environment [1]. This mechanism allows cells to stop proliferation as soon as a threshold is reached at a given site. Tumor cells exhibit an analogous behavior, even though to a significant lesser extent than their healthy counterpart, and with more relevance in three-dimensional cultures than in monolayers [172].

The biochemical pathways underlying contact inhibition are still an active area of research. They are linked to adhesive interactions between neighboring cells, mediated by adhesion proteins such as cadherins [2]. Moreover, these mechanisms include a series of proteins involved in cell cycle regulation. To this regard, the G1 checkpoint, also known as the restriction point (R), represents a fundamental step in the cell cycle, controlling cell commitment to mitosis [144]. Regulation of this cell checkpoint depends on the retinoblastoma protein (pRb). In particular, the hypophosphorylated form of pRb prevents progression from the G1 to the S phase of the cell cycle, inhibiting cell duplication. On the other hand, phosphorylation of pRb leads to its inactivation allowing the cell to undergo mitosis. Phosphorylation of

Section 3.3 of this chapter is based upon the work in: Mascheroni P, Boso D P, Preziosi L, Schrefler B A, "Evaluating the influence of mechanical stress on anticancer treatments through a multiphase porous media model", submitted to *Journal of Theoretical Biology*.

pRb depends on cyclin-dependent kinases (Cdks), which in turn are subject to the action of cyclins [48]. Finally, the activity of the whole complex is further regulated by several inhibitor proteins, in particular the cyclin-dependent kinase inhibitor p27 [84, 145]. Interestingly, an over-expression of this protein has been observed following cell-cell contact in three-dimensional cultures, as compared to the levels expressed in monolayers [171, 172, 197]. The adhesive interactions between cells inside tumor spheroids lead to upregulation of p27, which results in cell arrest in a quiescent phase of the cycle. Recently, the expression of p27 has been investigated through a series of experiments involving mechanical compression of three-dimensional cell aggregates [46]. Results show that a controlled compressive stress on tumor spheroids inhibits cell proliferation by an over-expression of p27, blocking the cancerous cells at the restriction point of the cell cycle.

At the beginning of this Introduction, we have observed that the presence of a non-proliferating cellular fraction has important consequences on the therapeutic efficacy of different chemotherapeutic agents. Notably, previous works have shown that a reduction in p27 expression in tumor spheroids could lead to better outcomes in terms of drug performance [171, 172, 197]. However, experiments quantifying the influence of mechanical stress on drug efficacy have still to be performed. Note that, interestingly, the compressive stresses that can be induced in tumor spheroids are of the same order of magnitude of those measured in vivo [22, 177, 54], in the range of a few kPa.

Phenomena concerning the mechanisms of drug action, as well as the mechanical characterization of the state of a tissue, are difficult to investigate from a pure biological and biochemical framework. To this end, mathematical models provide a valuable tool for establishing which of the biophysical features of the tumor and the stroma are responsible for the observed behaviors. As recalled in Chapter 2, several review papers discussing different approaches to cancer modeling have been published [158, 148, 24, 164, 3]. Some models describe the action of a therapeutic agent on tumor spheroids [190, 69, 60], whereas others take into account *in vivo* settings, as in [86, 95, 131]. There are also models addressing the effects of mechanical stress on tumor development, such as those in [98, 177, 112]. However, to our knowledge, there is a lack of mathematical models focusing on the interactions between anticancer agents and the mechanical environment surrounding the tumor.

The aim of this Section is to develop a theoretical framework that is able to take these interactions into account, providing new insights into mechanics-mediated drug resistance. In the following, we specialize our study to tumor spheroids. We

address the effects of a chemotherapeutic agent, supposed to target cell proliferation, on these cell aggregates. Then, we evaluate the influence of mechanical compression on treatment efficacy.

The remainder of the Section is organized as follows. Section 3.3.2 describes the mathematical model; the governing equations are presented, together with the assumed constitutive relations and parameter values. In Section 3.3.3 we report the results of the model. We start from the effects of different drug concentrations on the spheroid growth curve. Then, we consider a range of mechanical pressures acting on the spheroid surface and investigate their interactions with the treatment. Finally, we test different mathematical expressions for the drug-induced cell death term. Section 3.3.4, at the end, presents some concluding remarks.

3.3.2 Governing equations

3.3.2.1 Balance laws

We build upon the mathematical model in Section 3.1 to describe the transport of chemotherapeutic agents within an avascular tumor. The tumor is modeled as a biphasic porous material, and the governing equations are derived from porous media theory. Again, we denote by t the solid phase of the porous medium, constituted by tumor cells (TCs) and ECM. The interstitial fluid (IF) constitutes the fluid phase (f), and permeates the pores of the cellular scaffold. In our description, TCs are divided into living (LTC) and necrotic (NTC) fractions. In addition, we assume that the IF carries a nutrient, namely oxygen (ox), and a drug (ch). We consider a saturated material, where the IF fills all the voids of the porous medium. This results in the saturation constraint:

$$\varepsilon^{\mathrm{t}} + \varepsilon^{\mathrm{f}} = 1, \tag{3.53}$$

where ε^{α} denotes the volume fraction of phase α ($\alpha = t, \mathrm{f}$). The mass balance equations for the phases in the biphasic system are given by:

$$\partial_t \left(\rho^{\mathrm{t}}\varepsilon^{\mathrm{t}}\right) + \operatorname{div}\left(\varepsilon^{\mathrm{t}}\rho^{\mathrm{t}}\boldsymbol{v}^{\mathrm{t}}\right) = \Gamma_{\mathrm{gr}}^{\mathrm{f}\to\mathrm{t}} - \Gamma_{\mathrm{de}}^{\mathrm{t}\to\mathrm{f}}, \tag{3.54}$$

$$\partial_t \left(\varepsilon^{\mathrm{f}}\rho^{\mathrm{f}}\right) + \operatorname{div}\left(\varepsilon^{\mathrm{f}}\rho^{\mathrm{f}}\boldsymbol{v}^{\mathrm{f}}\right) = -\Gamma_{\mathrm{gr}}^{\mathrm{f}\to\mathrm{t}} + \Gamma_{\mathrm{de}}^{\mathrm{t}\to\mathrm{f}}. \tag{3.55}$$

Here, ρ^{α} is the true mass density and $\boldsymbol{v}^{\alpha}$ the velocity of the α phase ($\alpha = t, \mathrm{f}$). As before, $\Gamma_{\mathrm{gr}}^{\mathrm{f}\to\mathrm{t}}$ is the term responsible for mass exchange between IF and TCs, dependent on cell proliferation. $\Gamma_{de}^{\mathrm{f}\to t}$ represents instead mass exchange between TCs and IF resulting from cell death and their following degradation. In this case, we

need to include in the previous exchange term the action of the chemotherapeutic agent. Oxygen and drug are described as species dissolved into the IF, and their mass balance reads:

$$\partial_t\left(\varepsilon^{\mathrm{f}}\rho^{\mathrm{f}}\omega^{\mathrm{ox}}\right) + \operatorname{div}\left(\varepsilon^{\mathrm{f}}\rho^{\mathrm{f}}\omega^{\mathrm{ox}}\boldsymbol{v}^{\mathrm{f}}\right) - \operatorname{div}\left(\varepsilon^{\mathrm{f}}\rho^{\mathrm{f}}D^{\mathrm{ox}}\operatorname{grad}\omega^{\mathrm{ox}}\right) = -\Gamma_{\mathrm{ox}}^{\mathrm{ox}\to\mathrm{t}}, \tag{3.56}$$

$$\partial_t\left(\varepsilon^{\mathrm{f}}\rho^{\mathrm{f}}\omega^{\mathrm{ch}}\right) + \operatorname{div}\left(\varepsilon^{\mathrm{f}}\rho^{\mathrm{f}}\omega^{\mathrm{ch}}\boldsymbol{v}^{\mathrm{f}}\right) - \operatorname{div}\left(\varepsilon^{\mathrm{f}}\rho^{\mathrm{f}}D^{\mathrm{ch}}\operatorname{grad}\omega^{\mathrm{ch}}\right) = -\Gamma_{\mathrm{ch}}^{\mathrm{ch}\to\mathrm{t}}, \tag{3.57}$$

where ω^β denotes the mass fraction of species β and D^β is its diffusion coefficient ($\beta = \mathrm{ox}, \mathrm{ch}$). The terms $\Gamma_{\mathrm{ox}}^{\mathrm{ox}\to\mathrm{t}}$ and $\Gamma_{\mathrm{ch}}^{\mathrm{ch}\to\mathrm{t}}$ represent oxygen and drug uptake by TCs, respectively. We describe the evolution for living and necrotic TCs through the system:

$$\partial_t\left(\varepsilon^{\mathrm{t}}\rho^{\mathrm{t}}\omega^{\mathrm{Lt}}\right) + \operatorname{div}\left(\varepsilon^{\mathrm{t}}\rho^{\mathrm{t}}\omega^{\mathrm{Lt}}\boldsymbol{v}^{\mathrm{t}}\right) = -\varepsilon^{\mathrm{t}}r^{\mathrm{Nt}} + \Gamma_{\mathrm{gr}}^{\mathrm{f}\to\mathrm{t}}, \tag{3.58}$$

$$\partial_t\left(\varepsilon^{\mathrm{t}}\rho^{\mathrm{t}}\omega^{\mathrm{Nt}}\right) + \operatorname{div}\left(\varepsilon^{\mathrm{t}}\rho^{\mathrm{t}}\omega^{\mathrm{Nt}}\boldsymbol{v}^{\mathrm{t}}\right) = \varepsilon^{\mathrm{t}}r^{\mathrm{Nt}} - \Gamma_{\mathrm{de}}^{\mathrm{t}\to\mathrm{f}}. \tag{3.59}$$

Consistently with before, we have denoted by ω^{Lt} and ω^{Nt} the mass fractions of living and necrotic cells, respectively. Here $\varepsilon^{\mathrm{t}}r^{\mathrm{Nt}}$ is an intra-phase mass exchange term, accounting for the transfer of TCs from living to necrotic. Note that, by summing (3.58) and (3.59) we obtain (3.54) assuming that:

$$\omega^{\mathrm{Lt}} = 1 - \omega^{\mathrm{Nt}}. \tag{3.60}$$

The last equation is obtained from the balance law for momentum. Following Section 3.1.2, we have:

$$\boldsymbol{\sigma}_{\mathrm{eff}}^{\mathrm{t}} = \boldsymbol{\sigma}_{\mathrm{tot}} + \alpha_{\mathrm{B}}p^{\mathrm{f}}\boldsymbol{I}, \tag{3.61}$$

where we used the same notation as before for the total and effective stress tensors and for the IF fluid pressure. Then, the linear momentum balance equation for the tissue reads [111]:

$$\operatorname{div}\boldsymbol{\sigma}_{\mathrm{tot}} = \operatorname{div}\left(\boldsymbol{\sigma}_{\mathrm{eff}}^{\mathrm{t}} - \alpha_{\mathrm{B}}p^{\mathrm{f}}\boldsymbol{I}\right) = 0. \tag{3.62}$$

3.3.2.2 Constitutive relations

In Section 3.1.2, constitutive relationships for the effective stress and the mass transfer terms have been formulated. In particular, we have assumed the following form for the effective stress:

$$\boldsymbol{\sigma}_{\mathrm{eff}}^{\mathrm{t}} = -\Sigma\left(\varepsilon^{\mathrm{t}}\right)\boldsymbol{I}, \tag{3.63}$$

with Σ given by Equation (3.17).

The growth term $\Gamma_{\mathrm{gr}}^{\mathrm{f}\to\mathrm{t}}$ takes the same form as in Section 3.1.2. For the sake of completeness, we report it below:

$$\Gamma_{\mathrm{gr}}^{\mathrm{f}\to\mathrm{t}} = \gamma_{\mathrm{g}}^{\mathrm{t}} \left\langle \frac{\omega^{\mathrm{ox}} - \omega_{\mathrm{crit}}^{\mathrm{ox}}}{\omega_{\mathrm{env}}^{\mathrm{ox}} - \omega_{\mathrm{crit}}^{\mathrm{ox}}} \right\rangle_{+} \left(1 - \delta_1 \frac{\langle\Sigma\rangle_{+}}{\langle\Sigma\rangle_{+} + \delta_2}\right) \omega^{\mathrm{Lt}} \varepsilon^{\mathrm{t}}. \tag{3.64}$$

The rate of TC death in Equation (3.54) is given by:

$$\Gamma_{\mathrm{de}}^{\mathrm{t}\to\mathrm{f}} = \Gamma_{\mathrm{d,ly}}^{\mathrm{t}\to\mathrm{f}} + \Gamma_{\mathrm{d,ch}}^{\mathrm{t}\to\mathrm{f}}, \tag{3.65}$$

where the two contributions are related to cell lysis and drug action. In particular, the first term accounts for cell lysis and is given by the form already used in Section 3.1.2:

$$\Gamma_{\mathrm{d,ly}}^{\mathrm{t}\to\mathrm{f}} = \gamma_{\mathrm{f}}^{\mathrm{t}} \omega^{\mathrm{Nt}} \varepsilon^{\mathrm{t}}. \tag{3.66}$$

The second term takes the form:

$$\Gamma_{\mathrm{d,ch}}^{\mathrm{t}\to\mathrm{f}} = f_{\mathrm{ch}} \gamma_{\mathrm{c1}}^{\mathrm{t}} \omega^{\mathrm{ch}} \omega^{\mathrm{Lt}} \varepsilon^{\mathrm{t}}. \tag{3.67}$$

Here, $\gamma_{\mathrm{c1}}^{\mathrm{t}}$ accounts for the rate of drug-induced cell death. The function f_{ch} is related to the mechanism of action of the drug that is considered. Since we are interested in drugs that target TC proliferation, we assume f_{ch} to depend on the growth term in (3.64):

$$f_{\mathrm{ch}}\left(\omega^{\mathrm{ox}}, \Sigma\right) = \frac{\Gamma_{\mathrm{gr}}^{\mathrm{f}\to\mathrm{t}}}{\max\left(\Gamma_{\mathrm{gr}}^{\mathrm{f}\to\mathrm{t}}\right)} = \left\langle \frac{\omega^{\mathrm{ox}} - \omega_{\mathrm{crit}}^{\mathrm{ox}}}{\omega_{\mathrm{env}}^{\mathrm{ox}} - \omega_{\mathrm{crit}}^{\mathrm{ox}}} \right\rangle_{+} \left(1 - \delta_1 \frac{\langle\Sigma\rangle_{+}}{\langle\Sigma\rangle_{+} + \delta_2}\right). \tag{3.68}$$

In this way, the drug is most effective on the TCs that are well nourished and not compressed. Note that, depending on the particular drug that is considered, different choices for f_{ch} are possible (for example, in this framework it is possible to simulate drugs targeting hypoxia or specific cellular species in the tumor).

The rate of necrosis of living tumor cells in Equations (3.58) and (3.59) is described by the same relation that we presented in Section 3.1.2, given by:

$$\varepsilon^{\mathrm{t}} r^{\mathrm{Nt}} = \left\langle \frac{\omega^{\mathrm{ox}} - \omega_{\mathrm{crit}}^{\mathrm{ox}}}{\omega_{\mathrm{env}}^{\mathrm{ox}} - \omega_{\mathrm{crit}}^{\mathrm{ox}}} \right\rangle_{+} \omega^{\mathrm{Lt}} \varepsilon^{\mathrm{t}}. \tag{3.69}$$

Also for the oxygen consumption, we have the same expression as in Section 3.1.2, that is:

$$\Gamma_{\mathrm{ox}}^{\mathrm{ox}\to\mathrm{t}} = \gamma_0^{\mathrm{t}} \frac{\omega^{\mathrm{ox}}}{\omega^{\mathrm{ox}} + c_{\mathrm{ox}}} \omega^{\mathrm{Lt}} \varepsilon^{\mathrm{t}}. \tag{3.70}$$

Finally, the mass transfer term related to drug uptake in equation 3.65 takes the form:

$$\Gamma_{\mathrm{ch}}^{\mathrm{ch}\to\mathrm{t}} = \gamma_{\mathrm{c2}}^{\mathrm{t}} \omega^{\mathrm{ch}} \omega^{\mathrm{Lt}} \varepsilon^{\mathrm{t}}, \tag{3.71}$$

where we assumed the simplest kinetics for drug uptake (i.e. linear), with $\gamma_{\mathrm{c2}}^{\mathrm{t}}$ accounting for the drug uptake rate by LTCs [60, 191].

3.3.2.3 Model specialization to tumor spheroids

The equations of the model can be specialized to the case of tumor spheroids, following a similar procedure to that in Section 3.1.2. The resulting system for the TC volume fraction, necrotic mass fraction, and oxygen and drug mass fractions can be summarized as:

$$\frac{\partial \varepsilon^{\mathrm{t}}}{\partial t} - \frac{1}{r^2}\frac{\partial}{\partial r}\left(r^2 \varepsilon^{\mathrm{t}} \frac{k}{\mu^{\mathrm{f}}} \Sigma' \frac{\partial \varepsilon^{\mathrm{t}}}{\partial r}\right) - \frac{1}{\rho}\left(\Gamma_{\mathrm{gr}}^{\mathrm{f}\to\mathrm{t}} - \Gamma_{\mathrm{de}}^{\mathrm{t}\to\mathrm{f}}\right) = 0, \tag{3.72}$$

$$\frac{\partial \left(\omega^{\mathrm{Nt}} \varepsilon^{\mathrm{t}}\right)}{\partial t} - \frac{1}{r^2}\frac{\partial}{\partial r}\left(r^2 \omega^{\mathrm{Nt}} \varepsilon^{\mathrm{t}} \frac{k}{\mu^{\mathrm{f}}} \Sigma' \frac{\partial \varepsilon^{\mathrm{t}}}{\partial r}\right) - \frac{1}{\rho}\left(\varepsilon^{\mathrm{t}} r^{\mathrm{Nt}} - \Gamma_{\mathrm{d,ly}}^{\mathrm{t}\to\mathrm{f}}\right) = 0, \tag{3.73}$$

$$\begin{aligned}\frac{\partial \left[\left(1-\varepsilon^{\mathrm{t}}\right)\omega^{\mathrm{ox}}\right]}{\partial t} &+ \frac{1}{r^2}\frac{\partial}{\partial r}\left(r^2 \omega^{\mathrm{ox}} \varepsilon^{\mathrm{t}} \frac{k}{\mu^{\mathrm{f}}} \Sigma' \frac{\partial \varepsilon^{\mathrm{t}}}{\partial r}\right) \\ &- \frac{1}{r^2}\frac{\partial}{\partial r}\left[r^2 \left(1-\varepsilon^{\mathrm{t}}\right) D^{\mathrm{ox}} \frac{\partial \omega^{\mathrm{ox}}}{\partial r}\right] + \frac{1}{\rho}\Gamma_{\mathrm{ox}}^{\mathrm{ox}\to\mathrm{t}} = 0,\end{aligned} \tag{3.74}$$

$$\begin{aligned}\frac{\partial \left[\left(1-\varepsilon^{\mathrm{t}}\right)\omega^{\mathrm{ch}}\right]}{\partial t} &+ \frac{1}{r^2}\frac{\partial}{\partial r}\left(r^2 \omega^{\mathrm{ch}} \varepsilon^{\mathrm{t}} \frac{k}{\mu^{\mathrm{f}}} \Sigma' \frac{\partial \varepsilon^{\mathrm{t}}}{\partial r}\right) \\ &- \frac{1}{r^2}\frac{\partial}{\partial r}\left[r^2 \left(1-\varepsilon^{\mathrm{t}}\right) D^{\mathrm{ch}} \frac{\partial \omega^{\mathrm{ch}}}{\partial r}\right] + \frac{1}{\rho}\Gamma_{\mathrm{ch}}^{\mathrm{ch}\to\mathrm{t}} = 0.\end{aligned} \tag{3.75}$$

Here, we have adopted spherical symmetry, and r is the radial coordinate over the spheroid radius. The parameters k and μ^{f} are the intrinsic permeability of the cellular scaffold and the dynamic viscosity of IF, respectively. They arise by assuming Darcy's law for the relative velocity of the two phases, as specified in Section 3.1.2. Moreover, we take the phases to be incompressible and assign a common value for their densities, which we denote by the constant ρ. Finally, here we make use of Σ', the derivative of Σ with respect to ε^{t}.

Again, we model the growth of the spheroid as a free-boundary problem, where the interface constituted by TCs is a material surface for the TCs that moves with velocity v^{t}, given by:

$$\frac{dR}{dt} = v^{\mathrm{t}} = -\left.\frac{k}{\mu^{\mathrm{f}}} \Sigma' \frac{\partial \varepsilon^{\mathrm{t}}}{\partial r}\right|_{r=R}, \tag{3.76}$$

where R is the external radius of the spheroid. The closed form of the differential problem is then obtained by defining a proper set of boundary and initial conditions. In particular, symmetry requires no-flow boundary conditions at the spheroid center,

Table 3.4: Parameters used in the simulations considering the effects of the drug.

Parameter	Unit	Value	Reference
$\omega_{\text{env}}^{\text{ox}}$	$(-)$	7.7×10^{-6}	[134, 133]
c_{ox}	$(-)$	1.48×10^{-7}	[30, 31]
γ_0^{t}	$\text{kg}/(\text{m}^3 \cdot \text{s})$	3.0×10^{-4}	[30, 31]
β	$(-)$	0.5	[23]
$\varepsilon_{\text{n}}^{\text{t}}$	$(-)$	0.8	[23]
ε_0^{t}	$(-)$	1/3	[23]
k	m^2	1.8×10^{-15}	[136]
μ^{f}	$\text{Pa} \cdot \text{s}$	1.0×10^{-3}	[167]
D^{ox}	m^2/s	3.2×10^{-9}	[167]
ρ	$\text{kg}/(\text{m}^3)$	1.0×10^3	[167]
$\omega_{\text{crit}}^{\text{ox}}$	$(-)$	2.0×10^{-6}	[120]
$\gamma_{\text{g}}^{\text{t}}$	$\text{kg}/(\text{m}^3 \cdot \text{s})$	5.4×10^{-3}	[120]
$\gamma_{\text{n}}^{\text{t}}$	$\text{kg}/(\text{m}^3 \cdot \text{s})$	1.5×10^{-1}	[120]
$\gamma_{\text{f}}^{\text{t}}$	$\text{kg}/(\text{m}^3 \cdot \text{s})$	1.15×10^{-2}	[120]
α	Pa	1.0×10^5	[120]
$\omega_{\text{env}}^{\text{ch}}$	$(-)$	$8.696 \div 271.76 \times 10^{-9}$	[60]
D^{ch}	m^2/s	9.375×10^{-14}	[60]
$\gamma_{\text{c2}}^{\text{t}}$	$\text{kg}/(\text{m}^3 \cdot \text{s})$	1.157×10^{-2}	[60]
$\gamma_{\text{c1}}^{\text{t}}$	$\text{kg}/(\text{m}^3 \cdot \text{s})$	5.0×10^4	-

while we enforce Dirichlet boundary conditions on the tumor external surface:

$$\frac{\partial \varepsilon^{\text{t}}}{\partial r} = \frac{\partial \omega^{\text{Nt}}}{\partial r} = \frac{\partial \omega^{\text{ox}}}{\partial r} = \frac{\partial \omega^{\text{ch}}}{\partial r} = 0, \quad \text{in } r = 0, \tag{3.77}$$

$$\varepsilon^{\text{t}} = \varepsilon_{\text{ext}}^{\text{t}}, \quad \omega^{\text{Nt}} = 0, \quad \omega^{\text{ox}} = \omega_{\text{env}}^{\text{ox}}, \quad \omega^{\text{ch}} = \omega_{\text{env}}^{\text{ch}}, \quad \text{in } r = R. \tag{3.78}$$

Finally, we assume the following initial conditions over the spheroid radius:

$$\varepsilon^{\text{t}} = \varepsilon_{\text{ext}}^{\text{t}}, \quad \omega^{\text{Nt}} = 0, \quad \omega^{\text{ox}} = \omega_{\text{env}}^{\text{ox}}, \quad \omega^{\text{ch}} = 0, \quad \text{for } 0 < r < R \text{ at } t = 0. \tag{3.79}$$

3.3.2.4 Model parameters

The parameters used in the model are listed in Table 3.4. In this Section, we need to add the values for the parameters appearing in the equations governing drug transport and uptake. For these quantities we assume the values in [60], obtained for spheroids treated with Doxorubicin. Actually, the parameter governing drug-induced cell death, $\gamma_{\text{c1}}^{\text{t}}$, depends on the particular therapeutic agent and cell line that are considered. Here it is selected to produce a reasonable response of the model when TCs are subjected to the given drug concentrations.

3.3.3 Results

3.3.3.1 Tumor spheroid growth in the presence of a drug

In this section we test the effects of a drug that targets cell proliferation in a three-dimensional cell aggregate. First we consider tumor spheroids that grow suspended in culture medium, subjected to different drug concentrations. We assume drug concentration at spheroid boundary to start from zero and, following a ramp, to reach the final value $\omega^{\mathrm{ch}}_{\mathrm{env}}$ after 3 h. In Figure 3.16, we show the evolution of the spheroid radius over time for different drug mass fractions (i.e. $\omega^{\mathrm{ch}}_{\mathrm{env}} = 0.086,\ 0.347,\ 1.391,\ 2.717 \times 10^{-7}$). Here, the arrow points in the direction of increasing ω^{ch}. We consider

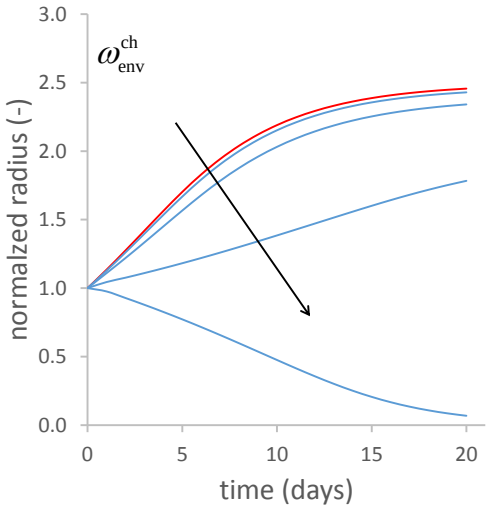

Figure 3.16: Effect of different drug concentrations on spheroid growth. The red line refers to a spheroid grown in the absence of drug. The other lines are for $\omega^{\mathrm{ch}}_{\mathrm{env}} = 0.086,\ 0.347,\ 1.391,\ 2.717 \times 10^{-7}$.

the normalized value of the spheroid radius, namely the ratio between the value of the radius at time t and the initial radius of the spheroid (200 μm in this case). The red line represents a spheroid grown in the absence of drug. We can distinguish between the first stages of growth, displaying an exponential/linear behavior, followed by a phase of growth saturation where the radius tends to a steady value. Low concentrations of drug do not alter the shape of the growth curve, whereas for high levels of the chemotherapeutic agent the spheroid starts to shrink and, for the highest value of ω^{ch}, growth is almost completely inhibited. This behavior closely resembles the growth curves obtained for example in [96, 127], where spheroids from various cell lines are subjected to different drugs.

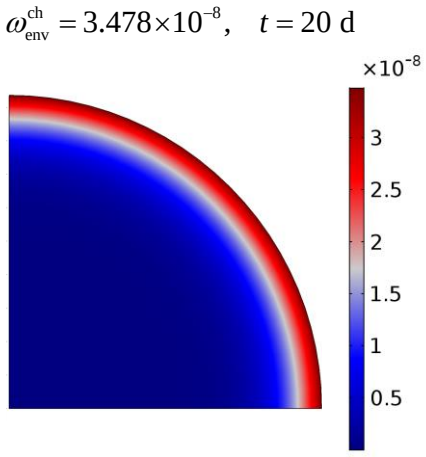

Figure 3.17: Drug mass fraction inside the spheroid at day 20 and for $\omega_{\text{env}}^{\text{ch}} = 3.478 \times 10^{-8}$.

Figure 3.17 shows the drug mass fraction inside the spheroid for an intermediate value of ω^{ch}, at the end of the simulation. Note the steep gradient of drug appearing from the boundary towards the center of the cell aggregate. In this case, the therapeutic agent can exert its effect only over the outermost region of the spheroid. This phenomenon arises as a consequence of poor diffusion of the drug molecules inside the tissue, and due to drug uptake by proliferating TCs. Interestingly, similar results are obtained in the experimental literature analyzing the penetration of free drug into a spheroid (see for example [187, 68]). Moreover, some researchers couple the therapeutic agent to a nanoparticle, enabling a larger penetration into the tumor [96, 187]. This latter kind of results can be integrated in the current model, once suitable mechanisms for nanoparticle delivery are hypothesized.

Then, we look for the value of drug mass fraction that is able to provide a reduction of 50% in spheroid volume (usually identified with the label IC_{50}, for "half maximal inhibitory concentration" [42]). We find a value of $\omega_{\text{env}}^{\text{ch}} = 1.185 \times 10^{-7}$, which we will denote from now on with IC_{50}. The growth curve relative to this drug mass fraction is shown in Figure 3.18.a, where we report the evolution of the normalized volume (i.e. the ratio between the spheroid volume at time t and its initial volume) over time. Figures 3.18.b-f show the evolution of different quantities, namely oxygen, necrotic and drug mass fractions, over spheroid radius and for different times. The evolution of oxygen mass fraction is represented in Figure 3.18.b. Note the steep oxygen gradient at the end of the simulation, from spheroid boundary towards its interior. The necrotic mass fraction of TCs is displayed in Figure 3.18.c. A necrotic

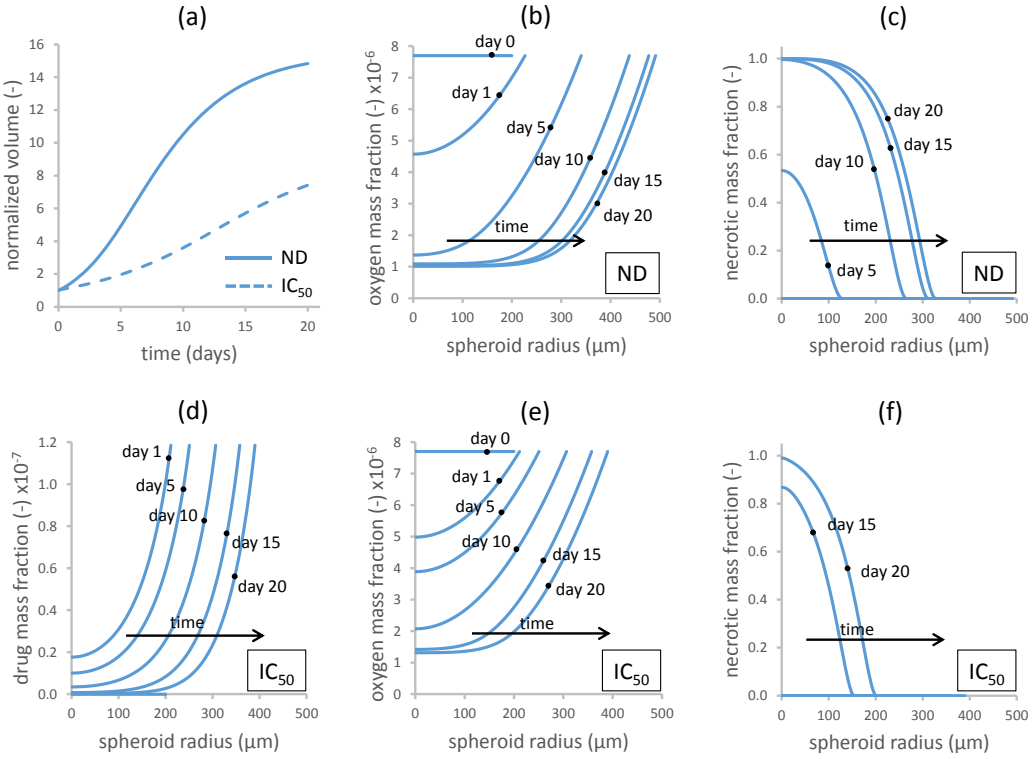

Figure 3.18: Comparison between a spheroid grown without an external drug (ND) and one treated with a drug mass fraction equal to IC_{50}.

population appears after a few days from the beginning of the simulation and gives rise to a necrotic core at later days. Both Figures 3.18.b and 3.18.c refer to a spheroid not treated with the drug, whereas the second row of Figures (3.18.d-f) pertains to a spheroid grown in the presence of a drug with a mass fraction equal to IC_{50}. The drug mass fraction over the spheroid radius is presented in Figure 3.18.d. Note that, after a few days from the beginning of the simulation, the therapeutic agent is mainly distributed over the spheroid periphery. Figure 3.18.e shows the oxygen mass fraction in the drug-treated spheroid. We can observe a behavior similar to the one in Figure 3.18.b, but this time over a smaller spheroid. Finally, the necrotic mass fraction in a spheroid subjected to the drug is shown in Figure 3.18.f. Compared to Figure 3.18.c, here the necrotic core is less extended and appears at later times in the simulation. This may be due to a smaller mass fraction of LTCs that can undergo necrosis, deriving from LTC killing by the chemotherapeutic agent.

3.3.3.2 Effect of mechanical compression on drug efficacy

In Section 3.1, we investigated the effects of an external mechanical pressure on the growth curves of tumor spheroids. Figure 3.19 report these previous findings, in terms of the evolution of the normalized volumes of spheroids subjected to different compressive stresses. We consider four compression levels, ranging from 1 kPa to 10

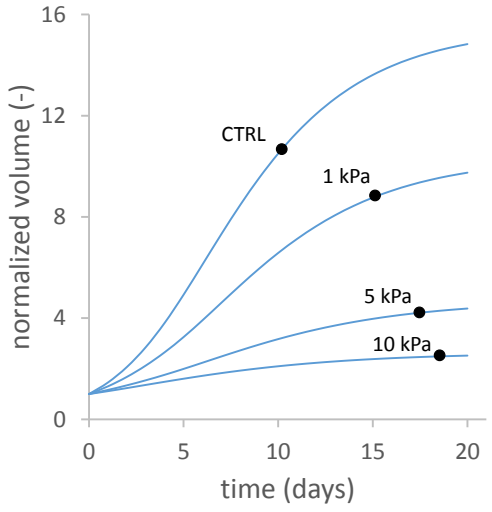

Figure 3.19: Normalized volumes of spheroids grown under different external mechanical pressures.

kPa. The growth of the most compressed spheroid shows a 7-fold reduction when compared to the control (grown in the absence of an external stress). Note that

the inhibitory effect of compressive stresses is included in the equations through the constitutive relation in (3.64). We make use of these results to test our newly introduced framework for drug transport and uptake in the spheroid. In particular, we apply the same external mass fraction of drug (IC_{50}) to each of the compression tests. Then, we check for variations in spheroid volumes with respect to the case with no drug added to the culture medium (Figure 3.20 and 3.21). Figure 3.20 compares the

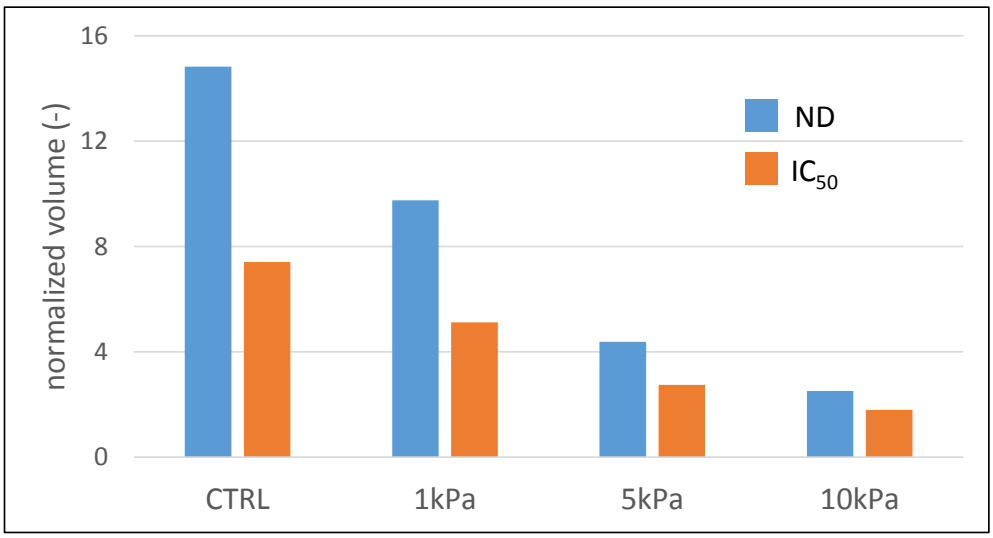

Figure 3.20: Comparison of the normalized volumes of spheroids subjected to different mechanical stresses, grown in the absence of drug (ND) or subjected to a drug concentration of IC_{50}.

normalized volumes of spheroids undergoing different compressive stresses. We test spheroids in the absence (ND) or presence (IC_{50}) of a chemotherapeutic drug. Both the series, ND and IC_{50}, exhibit the same decreasing trend, although with a slower volume reduction for drug-treated spheroids. The variation between the two volumes for each compressive condition is shown in Figure 3.21. According to the definition of IC_{50}, the control case exhibits a 50% reduction in volume. Interestingly, the series displays a percentage variation decreasing with the extent of mechanical compression, as highlighted by the black arrow. The case undergoing maximum compression shows a variation of about 30% in volume reduction. The observed behavior arises as a consequence of a lower proliferation index within the spheroid. In fact, mechanical stress inhibits cell proliferation via Equation (3.64) of the model, providing smaller values for the growth term as compression increases. Since our discussion is based on drugs that target cell duplication, growth inhibition is responsible for a cell population over which the therapeutic agent is less effective. Note that this effect could be relevant for in vivo applications: a drug concentration that is known to be effective in a particular

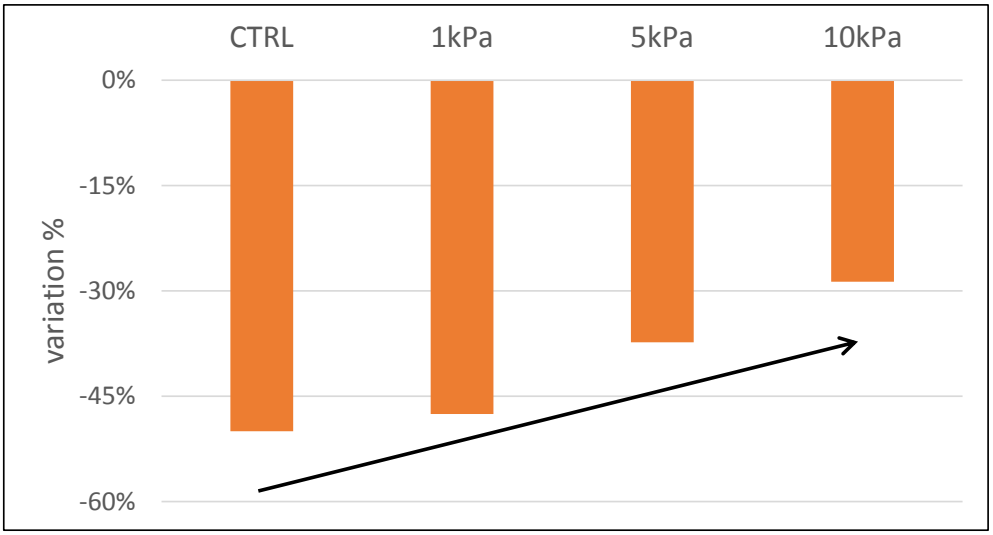

Figure 3.21: Variation in spheroid volume due to the action of a chemotherapeutic drug at different external mechanical pressures.

regime (such as 3D cultures) could not provide the same results when the tumor is subjected to mechanical compression.

3.3.3.3 Analysis of different drug-induced death terms

To confirm that model results are not biased by the particular choice of the term in (3.67), we test different mathematical expressions accounting for drug-induced cell death. The simplest hypothesis, assumed in (3.67), considers cell death to be proportional to the local amount of drug. In the following, we will refer to this case as the "linear" one. We introduce two additional relationships, given by:

$$\Gamma_{\mathrm{d,ch}}^{\mathrm{t}\to\mathrm{f}} = f_{\mathrm{ch}} \frac{m_1 \omega^{\mathrm{ch}}}{\omega^{\mathrm{ch}} + m_2} \omega^{\mathrm{Lt}} \varepsilon^{\mathrm{t}}, \tag{3.80}$$

$$\Gamma_{\mathrm{d,ch}}^{\mathrm{t}\to\mathrm{f}} = f_{\mathrm{ch}} p_1 \left(\omega^{\mathrm{ch}}\right)^{p_2} \omega^{\mathrm{Lt}} \varepsilon^{\mathrm{t}}. \tag{3.81}$$

In (3.80), we assume a dependence of the Michaelis-Menten type; in (3.81) the assume relationship takes the form of a power law. Note that, as the functional dependence on the local drug concentration changes, these relations give rise to new values for the inhibitory concentration IC_{50}. We report the new IC_{50} and the values for the parameters that characterize the above expressions in Table 3.5. Once the new forms for the drug-induced cell death term are implemented into the model, we perform the same numerical tests of the previous Section to analyze the coupled effect of drug action and mechanical compression. In Figure 3.22, we report the variation in terms of spheroid volume induced by the drug for different compressive stresses. Like in

Table 3.5: Parameter values for the relations assumed in the cell death term.

Relation	Parameter	Value	Unit	IC_{50}
Linear	γ_{c1}^{t}	5.0×10^{4}	$kg/(m^3 \cdot s)$	1.185×10^{-7}
Michaelis-Menten	m_1	1.5×10^{-2}	$kg/(m^3 \cdot s)$	5.345×10^{-8}
	m_2	1.0×10^{-7}	$(-)$	
Power law	p_1	2.5×10^{11}	$kg/(m^3 \cdot s)$	1.862×10^{-7}
	p_2	2	$(-)$	

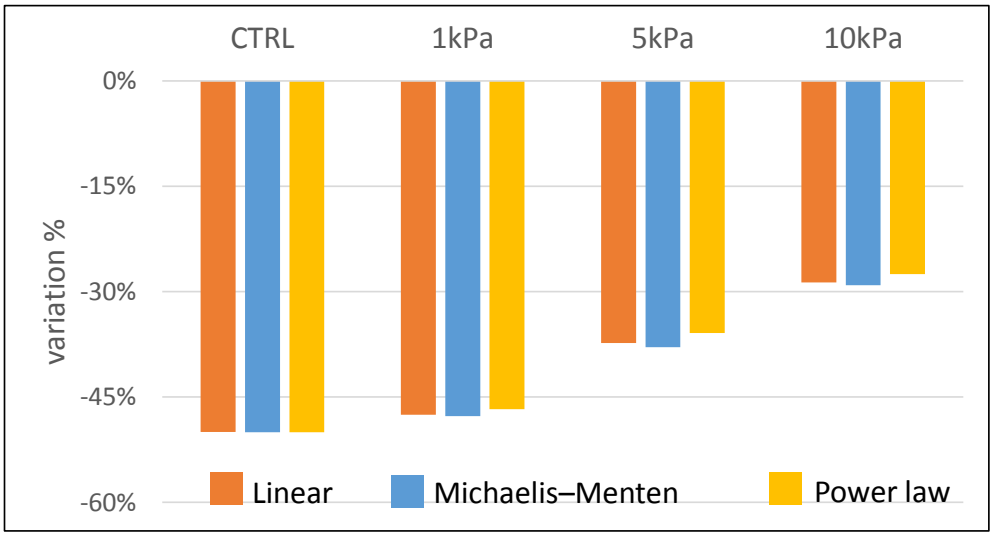

Figure 3.22: Effect of different mathematical relations on spheroid volume variation.

Figure 3.21, the first series of data serves as a control and indicates a variation of 50% with respect to the drug-free condition. The other series are related to the different compression regimes and compare the model response for the different mathematical relationships assumed for the death term. It is possible to observe that the variation in volume reduction is similar to the linear case, analyzed in the previous section. The effect of mechanical compression on drug efficacy described previously does not seem therefore to be originated from the particular mathematical form adopted for the death term in (3.67).

3.3.4 Conclusions

In this work, we introduce equations for drug transport and uptake by TCs in our previous mathematical model for avascular tumor growth. Then, we adapt the equations for the tumor spheroid case and test the effects of a proliferation targeting drug on

spheroid growth curves. We observe a qualitative agreement between model results and experimental literature [96, 127]. After that, we simulate tumor spheroids undergoing mechanical compressive stresses of different amplitudes, and consider their volume reduction due to the presence of a therapeutic agent. Interestingly, we notice a decreased growth inhibition efficacy of the drug in terms of the final volumes reached by the spheroids. Finally, we test three different mathematical expressions for the cell death term induced by the therapeutic agent. The resulting predictions are similar for all the tested expressions, suggesting that the particular form of the adopted constitutive relation does not influence model response. Taken together, these results suggest that mechanical compression of tumor spheroids may compromise the efficacy of a chemotherapeutic agent targeting cell proliferation.

As several simplifying assumptions are considered in the work, the model is certainly open to further improvements. In particular, here we model only one nutrient species, i.e. oxygen, diffusing in the interstitial fluid and regulating TC proliferation. Even though the presence of other chemicals is implicitly contained within the mass exchange term in (3.64), including additional nutrients, growth and necrosis factors could provide a more detailed description of the tumor system [34, 91]. Moreover, since the particular physiochemical environment in which the tumor is embedded affects significantly the outcomes of therapies (see for example [115, 168]), the inclusion of additional factors could result in a better description of drug dynamics. Another point requiring some attention is the proper choice of constitutive relations. As it happens frequently in literature, most of these laws are derived from phenomenological arguments. More experimental work is needed to link the mathematical form that is assigned to the various terms to the underlying biology. This kind of reasoning should be applied to the constitutive relations accounting for the drug uptake and the following effects on TCs, as well as the mechanical description of the tumor ensemble. For the latter, here we consider a simple law, linking the stress in the tissue to the local volume fraction of tumor cells. This assumption provides a great simplification of the equations and is shown to give a good description of experimental observations, as shown in Section 3.1. However, it neglects several phenomena related to the mechanical behavior of a biological tissue. For example, viscoplastic effects existing at smaller timescales than those of cell proliferation are not taken into account [56, 66]. Also, breaking and formation of cellular bonds during tumor development should be included to give a more complete description [7, 147]. Finally, we highlight the need for experiments addressing the interactions between therapeutic agents and tumor mechanical environment. These will serve to calibrate the parameters in

the equations and to test model results. Part of future experimental work should also be devoted to the biochemical understanding of the growth inhibition process following mechanical stress. Although some work is already present in the literature [35, 112, 46], several details remain to be elucidated. New investigations analyzing the interactions between the tumor and its bio-mechanical environment should allow a better understanding of disease progression, with the final goal of aiding the design of effective therapeutic treatments.

Chapter 4

Modeling the mechanical response of the tumor tissue

4.1 Introduction

At the present time, a unifying description of cancer is still lacking. This happens both because many tumors are characterized by different origins and features, and the determinants of tumor progression are still partially unclear [192]. Cells in solid tumors live in a rich environment, filled with water and proteins [113, 2]. Several nutrients diffuse into the interstitial fluid and are consumed by the cells to support their survival and duplication. Among the other substances dispersed into the fluid, there is also a plethora of chemical factors. In particular, growth promoting factors, growth inhibitory factors, and chemotactic factors are able to trigger subcellular pathways, eventually resulting in different cell behaviors. The extracellular space is also filled by a network of cross-linked proteins, organized in the extracellular matrix (ECM). This matrix constitutes a biological scaffold that provides structural and biochemical support to the surrounding cells. By exerting forces on the proteins of the network, cells can migrate towards different regions of the tissue, or proliferate once they have formed stable bonds. The ECM is also subjected to continuous remodeling by cells, as some of them produce matrix degrading enzymes while others secrete new filaments. Remarkably, all these phenomena are influenced by the mechanical stress to which the tissue is subjected, through mechanisms that are still an active area of research [183, 82, 155]. Cell duplication depends on the balance between biochemical and mechanical inputs, too. While the dependence of cell growth on certain nutrients and

Chapter 4 of this dissertation is based upon the work in: Mascheroni P, Carfagna M, Grillo A, Boso D P, Preziosi L, Schrefler B A, "An avascular tumor growth model based on porous media mechanics and evolving natural configurations", submitted to *New Journal of Physics*.

growth factors is well documented (see for example [132]), several new studies are focused on determining the influence of mechanical stress on cell proliferation [107, 57]. In one of the first works about this subject, Helmlinger and coworkers [83] show that a compressive stress is able to inhibit the proliferation of cells in tumor spheroids. These findings are confirmed and extended by later works from the same group [35] and by other researches that use different experimental methodologies [47, 128]. All these phenomena constitute a complex framework, which is continuously enriched by new discoveries and increasingly large data sets. Recently, Hanahan and Weinberg [79, 80] published two landmark papers in which they summarize the characteristics shared by malignant tumors. In general, these common traits are related to the occurrence of a failure in cell control mechanisms, and lead to uncontrolled cell proliferation and avoidance of self-death signaling.

Facing this complexities, physical scientists have started to apply the tools from physics, mathematics and engineering to contribute to cancer research in the last years [125]. The problem of describing cancer through mathematical models is, however, a difficult one. On the other hand, such models may give some insight into the understanding of the illness, as discussed in Section 2.3. Several models in the literature focus on the biochemical events occurring during the growth of a tumor. These are generally formulated in terms of balance laws along with advection-diffusion-reaction equations for modeling the evolution of nutrients, and suitable closure conditions for the cell velocity field [7]. More recently, mathematical models started to consider the mechanical aspects of tumor growth, including the dependence of cell growth and death on compression, the effect of mechanical stresses on the tissues surrounding the tumor, and the constitutive laws connecting stresses and deformations in the tumor tissue [164]. Several models describe the tumor mass as a fluid, which in some cases might be a strong simplification. However, significant theoretical difficulties may arise when modeling tumors as solids. In fact, tumor cells duplicate and die, the ECM remodels continuously, and the ensemble of cells is subjected to internal reorganization and change in adhesion properties. In terms of continuum mechanics, it is difficult to define a reference configuration from which deformations can be calculated, since the material is continuously changing. A possible solution to this problem is found by applying the theory of evolving natural configurations. As the basic concept has its roots in the works of Skalak and Rodriguez [170, 157] (taking in turn inspiration from classical theories in elastoplasticity [15, 103, 108]), Rajagopal and Humphrey [87] apply this theory to describe the growth and remodeling of different tissues. The method consists in splitting the evolution of the system in growth, plastic remodeling,

and elastic distortions through a multiplicative decomposition of the deformation gradient tensor. Starting from the early works of Ambrosi and Mollica [4, 5], considering a purely elastic monophasic model to evaluate residual stresses in tumor spheroids, Ambrosi and Preziosi in [6] develop a multiphase framework in which internal cell reorganization is also taken into account. The flow rule for cell bond reorganization was further studied in the works of Giverso and Preziosi [66] to describe experiments of cell aggregate compression.

In this Chapter, we extend the modeling framework mentioned above by including the effect of a nutrient on the tumor growth dynamics. Two cell populations are also taken into account, describing proliferating and necrotic tumor cells. Moreover, we test the influence of external healthy tissues with different mechanical properties on tumor development. These new features are analyzed in three cases of biological interest, namely the growth of a tumor spheroid in the culture medium, in a host tissue, and in a three-dimensional configuration. The dependence of tumor development on the external mechanical environment is investigated, with particular attention to cell reorganization and its impact on stress relaxation.

The Section is then organized as follows. In section 4.2, we introduce the mathematical model, with a focus on the decomposition of the deformation gradient. In section 4.3, we simplify the model to study a trial case, namely the compression of a soft tissue. In section 4.4, we present the numerical results for three tumor growth conditions. Finally, we draw our conclusions and propose further research in Section 4.5.

4.2 Mathematical model

In our model, a tumor mass is described as a biphasic system comprising a solid and a fluid phase. The solid phase (s) is assumed to consist of cells and ECM. These constitute a scaffold that will be described as a solid medium in the sequel. The fluid phase (f) is identified with the tumor's interstitial fluid. We hypothesize that only two types of cells are relevant for our purposes: the proliferating cells (p) and the necrotic cells (n), included in the solid phase. On the other hand, the fluid phase comprises only a nutrient (N). Clearly, many other chemicals are present in this fluid constituent, even though they are not explicitly accounted for here. In some tests studied in this work, we shall also consider the presence of a soft host tissue and of a stiff host tissue (e.g., bone), which surround the growing tumor. In our model, we shall assume that these tissues occupy three different subdomains of the same region

of space, and that both the soft and the stiff host tissue comprise a solid and a fluid phase, which, in analogy with the notation used for the tumor, are associated with the apices (s) and (f). Again, we use (N) for identifying the nutrient constituent of the fluid in the soft and stiff host tissue.

4.2.1 Balance equations

We indicate by K_t the region of space occupied by the system at time t, and we assume that K_t is partitioned into three disjoint sets, i.e., $K_t = \mathcal{T}_t \sqcup \mathcal{H}_t \sqcup \mathcal{B}_t$. Here, $\mathcal{T}_t$ represents the *tumor tissue*, $\mathcal{H}_t$ is a *soft host tissue*, and $\mathcal{B}_t$ denotes a *stiff host tissue*, e.g., the bone. Since the majority of the processes, such as growth and mass exchange among the system's constituents, take place in the tumor we start our discussion by considering first only the balance laws holding in the interior of $\mathcal{T}_t$.

We assume that the pore space of the cellular scaffold, which represents the solid phase, is completely filled with the fluid. The system is thus constrained by the saturation condition

$$\varepsilon^{\mathrm{f}} + \varepsilon^{\mathrm{s}} = 1, \tag{4.1}$$

where ε^{α} is the volume fraction of the αth phase ($\alpha = \mathrm{f}, \mathrm{s}$). The different constituents (or species) in the phases are described through their mass fraction ω^{β}, with $\beta = \mathrm{p}, \mathrm{n}$ in the solid phase, and $\beta = \mathrm{N}$ in the fluid phase. The mass balance laws for the constituents of the solid phase (i.e., the proliferating and necrotic cells) are given by

$$\partial_t \left(\varepsilon^{\mathrm{s}} \rho^{\mathrm{s}} \omega^{\mathrm{p}}\right) + \operatorname{div}\left(\varepsilon^{\mathrm{s}} \rho^{\mathrm{s}} \omega^{\mathrm{p}} \boldsymbol{v}^{\mathrm{s}}\right) = \Gamma_{\mathrm{p}}^{\mathrm{p}\to\mathrm{n}} + \Gamma_{\mathrm{p}}^{\mathrm{f}\to\mathrm{p}}, \tag{4.2}$$

$$\partial_t \left(\varepsilon^{\mathrm{s}} \rho^{\mathrm{s}} \omega^{\mathrm{n}}\right) + \operatorname{div}\left(\varepsilon^{\mathrm{s}} \rho^{\mathrm{s}} \omega^{\mathrm{n}} \boldsymbol{v}^{\mathrm{s}}\right) = \Gamma_{\mathrm{n}}^{\mathrm{p}\to\mathrm{n}} + \Gamma_{\mathrm{n}}^{\mathrm{n}\to\mathrm{f}}. \tag{4.3}$$

Here, ρ^{s} and $\boldsymbol{v}^{\mathrm{s}}$ denote the mass density and the velocity of the solid phase, respectively. The terms $\Gamma_{\mathrm{p}}^{\mathrm{p}\to\mathrm{n}}$, $\Gamma_{\mathrm{p}}^{\mathrm{f}\to\mathrm{p}}$, $\Gamma_{\mathrm{n}}^{\mathrm{p}\to\mathrm{n}}$, and $\Gamma_{\mathrm{n}}^{\mathrm{n}\to\mathrm{f}}$ are sources and sinks of mass that account for the mass exchange processes among the constituents of the system under study. More specifically, $\Gamma_{\mathrm{p}}^{\mathrm{p}\to\mathrm{n}}$ is the rate at which proliferating cells become necrotic, and $\Gamma_{\mathrm{p}}^{\mathrm{f}\to\mathrm{p}}$ is the mass uptake of the proliferating cells due to the exchange of mass with the fluid phase. Analogously, $\Gamma_{\mathrm{n}}^{\mathrm{p}\to\mathrm{n}}$ is the increase of mass of the necrotic cells at the expenses of the proliferating ones, and $\Gamma_{\mathrm{n}}^{\mathrm{n}\to\mathrm{f}}$ denotes the rate at which necrotic cells dissolve in the fluid phase. Summing together (4.2) and (4.3), and recalling the constraint on the mass fractions, $\omega^{\mathrm{p}} + \omega^{\mathrm{n}} = 1$, we determine the mass balance law for the solid phase as a whole, i.e.,

$$\partial_t \left(\varepsilon^{\mathrm{s}} \rho^{\mathrm{s}}\right) + \operatorname{div}\left(\varepsilon^{\mathrm{s}} \rho^{\mathrm{s}} \boldsymbol{v}^{\mathrm{s}}\right) = \Gamma^{\mathrm{s}}, \tag{4.4}$$

where Γ_{s} is given by

$$\Gamma^{\mathrm{s}} = \Gamma_{\mathrm{p}}^{\mathrm{p}\to\mathrm{n}} + \Gamma_{\mathrm{p}}^{\mathrm{f}\to\mathrm{p}} + \Gamma_{\mathrm{n}}^{\mathrm{p}\to\mathrm{n}} + \Gamma_{\mathrm{n}}^{\mathrm{n}\to\mathrm{f}}. \tag{4.5}$$

In particular, we choose $\Gamma_{\mathrm{p}}^{\mathrm{p}\to\mathrm{n}}$ and $\Gamma_{\mathrm{n}}^{\mathrm{p}\to\mathrm{n}}$ such that they balance each other, i.e.,

$$\Gamma_{\mathrm{p}}^{\mathrm{p}\to\mathrm{n}} + \Gamma_{\mathrm{n}}^{\mathrm{p}\to\mathrm{n}} = 0 \quad \Rightarrow \quad \Gamma_{\mathrm{p}}^{\mathrm{p}\to\mathrm{n}} = -\Gamma_{\mathrm{n}}^{\mathrm{p}\to\mathrm{n}}, \tag{4.6}$$

which implies the equality

$$\Gamma^{\mathrm{s}} = \Gamma_{\mathrm{p}}^{\mathrm{f}\to\mathrm{p}} + \Gamma_{\mathrm{n}}^{\mathrm{n}\to\mathrm{f}}. \tag{4.7}$$

In addition to (4.2) and (4.3) we consider also the mass balance law of the fluid phase as a whole and of the nutrient, i.e.,

$$\partial_t \left(\varepsilon^{\mathrm{f}}\rho^{\mathrm{f}}\right) + \mathrm{div}\left(\varepsilon^{\mathrm{f}}\rho^{\mathrm{f}}\boldsymbol{v}^{\mathrm{f}}\right) = \Gamma^{\mathrm{f}}, \tag{4.8}$$

$$\partial_t \left(\varepsilon^{\mathrm{f}}\rho^{\mathrm{f}}\omega^{\mathrm{N}}\right) + \mathrm{div}\left(\varepsilon^{\mathrm{f}}\rho^{\mathrm{f}}\omega^{\mathrm{N}}\boldsymbol{v}^{\mathrm{f}}\right) + \mathrm{div}\boldsymbol{J}^{\mathrm{N}} = \Gamma_{\mathrm{N}}^{\mathrm{N}\to\mathrm{p}} \tag{4.9}$$

where ρ^{f} and $\boldsymbol{v}^{\mathrm{f}}$ are the mass density and the velocity of the fluid phase, respectively, ω^{N} is the mass fraction of the nutrient, and $\boldsymbol{J}^{\mathrm{N}}$ is the mass flux vector of the nutrient, which is generated by the difference between its own velocity and $\boldsymbol{v}^{\mathrm{f}}$. We assume that $\boldsymbol{J}^{\mathrm{N}}$ obeys standard Fick's law, which yields the expression $\boldsymbol{J}^{\mathrm{N}} = -\varepsilon^{\mathrm{f}}\rho^{\mathrm{f}}\boldsymbol{D}^{\mathrm{N}}\mathrm{grad}\,\omega^{\mathrm{N}}$, where $\boldsymbol{D}^{\mathrm{N}}$ is the diffusion tensor. Finally, Γ^{f} is the rate at which the fluid phase exchanges mass with the solid phase, and $\Gamma_{\mathrm{N}}^{\mathrm{N}\to\mathrm{p}}$ is the term describing the uptake of nutrients from the interstitial fluid to the proliferating cells. Since the biphasic system under study is assumed to be closed with respect to mass, Γ^{s} and Γ^{f} must satisfy the condition

$$\Gamma^{\mathrm{f}} + \Gamma^{\mathrm{s}} = 0, \quad \Rightarrow \quad \Gamma^{\mathrm{s}} = -\Gamma^{\mathrm{f}}. \tag{4.10}$$

In addition to the mass balance laws (4.2), (4.3), (4.8), and (4.9), we also consider the momentum balance laws associated with the solid and the fluid phase. By neglecting all external body forces, such as gravity, the local form of these balance laws can be written as

$$\partial_t(\varepsilon^{\mathrm{s}}\rho^{\mathrm{s}}\boldsymbol{v}^{\mathrm{s}}) + \mathrm{div}\left(\varepsilon^{\mathrm{s}}\rho^{\mathrm{s}}\boldsymbol{v}^{\mathrm{s}}\otimes\boldsymbol{v}^{\mathrm{s}}\right) = \mathrm{div}\boldsymbol{\sigma}^{\mathrm{s}} + \left(\boldsymbol{m}^{\mathrm{s}} + \Gamma^{\mathrm{s}}\boldsymbol{v}^{\mathrm{s}}\right), \tag{4.11}$$

$$\partial_t(\varepsilon^{\mathrm{f}}\rho^{\mathrm{f}}\boldsymbol{v}^{\mathrm{f}}) + \mathrm{div}\left(\varepsilon^{\mathrm{f}}\rho^{\mathrm{f}}\boldsymbol{v}^{\mathrm{f}}\otimes\boldsymbol{v}^{\mathrm{f}}\right) = \mathrm{div}\boldsymbol{\sigma}^{\mathrm{f}} + \left(\boldsymbol{m}^{\mathrm{f}} + \Gamma^{\mathrm{f}}\boldsymbol{v}^{\mathrm{f}}\right), \tag{4.12}$$

where $\boldsymbol{\sigma}^{\alpha}$ and $\boldsymbol{m}^{\alpha} + \Gamma^{\alpha}\boldsymbol{v}^{\alpha}$ (with $\alpha = \mathrm{f}, \mathrm{s}$) are, respectively, the Cauchy stress tensor of the αth phase and the gain or loss of momentum of the αth phase due to the interactions with the other one. We remark that $\Gamma^{\alpha}\boldsymbol{v}^{\alpha}$ is directly related to the mass transfer between the phases, while $\boldsymbol{m}^{\alpha}$ is due to overall contact forces exchanged by

the fluid and the solid phase at the interface. Since the system is assumed to be closed with respect to momentum, the closure condition

$$(\boldsymbol{m}^{\mathrm{s}} + \Gamma^{\mathrm{s}}\boldsymbol{v}^{\mathrm{s}}) + (\boldsymbol{m}^{\mathrm{f}} + \Gamma^{\mathrm{f}}\boldsymbol{v}^{\mathrm{f}}) = (\boldsymbol{m}^{\mathrm{s}} + \boldsymbol{m}^{\mathrm{f}}) + \Gamma^{\mathrm{s}}(\boldsymbol{v}^{\mathrm{s}} - \boldsymbol{v}^{\mathrm{f}}) = \mathbf{0} \tag{4.13}$$

is enforced. In the following, however, we neglect inertial forces and the contribution $\Gamma^{\mathrm{s}}(\boldsymbol{v}^{\mathrm{s}} - \boldsymbol{v}^{\mathrm{f}})$. This allows to rewrite the momentum balance laws (4.11) and (4.12) as

$$\mathrm{div}\boldsymbol{\sigma}^{\mathrm{s}} + \boldsymbol{m}^{\mathrm{s}} = \mathbf{0}, \tag{4.14}$$

$$\mathrm{div}\boldsymbol{\sigma}^{\mathrm{f}} + \boldsymbol{m}^{\mathrm{f}} = \mathbf{0}, \tag{4.15}$$

while the closure condition (4.13) becomes

$$\boldsymbol{m}^{\mathrm{s}} + \boldsymbol{m}^{\mathrm{f}} = \mathbf{0}. \tag{4.16}$$

Finally, adding together (4.11) and (4.12) leads to the balance law of momentum for the system as a whole, i.e.,

$$\mathrm{div}(\boldsymbol{\sigma}^{\mathrm{s}} + \boldsymbol{\sigma}^{\mathrm{f}}) = \mathbf{0}. \tag{4.17}$$

Equations (4.1)-(4.17) must be studied in conjunction with the balance laws pertaining to the subdomains $\mathcal{H}_t$ and $\mathcal{B}_t$. The saturation constraint applies also in each of these two subdomains, i.e., it holds that

$$\varepsilon^{\mathrm{s}} + \varepsilon^{\mathrm{f}} = 1, \qquad \text{in } \mathcal{H}_t \sqcup \mathcal{B}_t. \tag{4.18}$$

Moreover, since in this work it is assumed that in $\mathcal{H}_t$ and $\mathcal{B}_t$ cells do not proliferate or die, it is sufficient to consider only one mass balance law for the solid phase as a whole, in which neither mass sources nor mass sinks appear. Thus, the mass balance law (4.4) becomes

$$\partial_t\left(\varepsilon^{\mathrm{s}}\rho^{\mathrm{s}}\right) + \mathrm{div}\left(\varepsilon^{\mathrm{s}}\rho^{\mathrm{s}}\boldsymbol{v}^{\mathrm{s}}\right) = 0, \qquad \text{in } \mathcal{H}_t \sqcup \mathcal{B}_t. \tag{4.19}$$

In addition, the mass balance law for the fluid phase as a whole and for the nutrient read

$$\partial_t\left(\varepsilon^{\mathrm{f}}\rho^{\mathrm{f}}\right) + \mathrm{div}\left(\varepsilon^{\mathrm{f}}\rho^{\mathrm{f}}\boldsymbol{v}^{\mathrm{f}}\right) = 0, \qquad \text{in } \mathcal{H}_t \sqcup \mathcal{B}_t, \tag{4.20}$$

$$\partial_t\left(\varepsilon^{\mathrm{f}}\rho^{\mathrm{f}}\omega^{\mathrm{N}}\right) + \mathrm{div}\left(\varepsilon^{\mathrm{f}}\rho^{\mathrm{f}}\omega^{\mathrm{N}}\boldsymbol{v}^{\mathrm{f}}\right) + \mathrm{div}\boldsymbol{J}^{\mathrm{N}} = 0, \qquad \text{in } \mathcal{H}_t \sqcup \mathcal{B}_t. \tag{4.21}$$

Finally, similarly to (4.14)–(4.17), also in this case the linear momentum balance laws and the closure condition $\boldsymbol{m}^{\mathrm{s}} + \boldsymbol{m}^{\mathrm{f}} = \boldsymbol{0}$ must apply, i.e.,

$$\operatorname{div}(\boldsymbol{\sigma}^{\mathrm{s}} + \boldsymbol{\sigma}^{\mathrm{f}}) = \boldsymbol{0}, \qquad \text{in } \mathcal{H}_t \sqcup \mathcal{B}_t \tag{4.22}$$

$$\operatorname{div}\boldsymbol{\sigma}^{\mathrm{f}} + \boldsymbol{m}^{\mathrm{f}} = \boldsymbol{0}, \qquad \text{in } \mathcal{H}_t \sqcup \mathcal{B}_t. \tag{4.23}$$

If the fluid phase can be regarded as macroscopically inviscid and the constituents are assumed to be incompressible, the stress tensors of the solid and the fluid phase can be chosen constitutively as [117]

$$\boldsymbol{\sigma}^{\mathrm{s}} = -\varepsilon^{\mathrm{s}} p^{\mathrm{f}} \boldsymbol{I} + \boldsymbol{\sigma}^{\mathrm{s}}_{\mathrm{eff}}, \qquad \text{in } \mathcal{T}_t \sqcup \mathcal{H}_t \sqcup \mathcal{B}_t, \tag{4.24}$$

$$\boldsymbol{\sigma}^{\mathrm{f}} = -\varepsilon^{\mathrm{f}} p^{\mathrm{f}} \boldsymbol{I}, \qquad \text{in } \mathcal{T}_t \sqcup \mathcal{H}_t \sqcup \mathcal{B}_t, \tag{4.25}$$

in which $\boldsymbol{I}$ is the identity tensor, p^{f} represents the fluid pressure, and $\boldsymbol{\sigma}^{\mathrm{s}}_{\mathrm{eff}}$ is referred to as the *effective* Cauchy stress tensor of the solid phase.

To complete the mathematical model, we recall that the sets of equations (4.1)-(4.17) and (4.18)-(4.23) must be accompanied by the following interface conditions, which apply at the internal boundaries separating the three subdomains $\mathcal{T}_t$, $\mathcal{H}_t$, and $\mathcal{B}_t$:

$$\boldsymbol{v}^{\mathrm{s}} \cdot \boldsymbol{n}\big|_{\mathcal{I}^{\alpha\beta}} = \boldsymbol{v}^{\mathrm{s}} \cdot \boldsymbol{n}\big|_{\mathcal{I}^{\beta\alpha}}, \tag{4.26}$$

$$\varepsilon^{\mathrm{f}} \rho^{\mathrm{f}} \boldsymbol{v}^{\mathrm{f}} \cdot \boldsymbol{n}\big|_{\mathcal{I}^{\alpha\beta}} = \varepsilon^{\mathrm{f}} \rho^{\mathrm{f}} \boldsymbol{v}^{\mathrm{f}} \cdot \boldsymbol{n}\big|_{\mathcal{I}^{\beta\alpha}}, \tag{4.27}$$

$$\left(\varepsilon^{\mathrm{f}} \rho^{\mathrm{f}} \omega^{\mathrm{N}} \boldsymbol{v}^{\mathrm{f}} + \boldsymbol{J}^{\mathrm{N}}\right) \cdot \boldsymbol{n}\big|_{\mathcal{I}^{\alpha\beta}} = \left(\varepsilon^{\mathrm{f}} \rho^{\mathrm{f}} \omega^{\mathrm{N}} \boldsymbol{v}^{\mathrm{f}} + \boldsymbol{J}^{\mathrm{N}}\right) \cdot \boldsymbol{n}\big|_{\mathcal{I}^{\beta\alpha}}, \tag{4.28}$$

$$\left(\boldsymbol{\sigma}^{\mathrm{s}} + \boldsymbol{\sigma}^{\mathrm{f}}\right) \cdot \boldsymbol{n}\big|_{\mathcal{I}^{\alpha\beta}} = \left(\boldsymbol{\sigma}^{\mathrm{s}} + \boldsymbol{\sigma}^{\mathrm{f}}\right) \cdot \boldsymbol{n}\big|_{\mathcal{I}^{\beta\alpha}}, \tag{4.29}$$

$$\omega^{\mathrm{N}}\big|_{\mathcal{I}^{\alpha\beta}} = \omega^{\mathrm{N}}\big|_{\mathcal{I}^{\beta\alpha}}, \tag{4.30}$$

$$p^{\mathrm{f}}\big|_{\mathcal{I}^{\alpha\beta}} = p^{\mathrm{f}}\big|_{\mathcal{I}^{\beta\alpha}}, \tag{4.31}$$

where $\mathcal{I}^{\alpha\beta}$ is the interface between the αth and the βth subdomain, with $\alpha, \beta = \mathcal{T}_t, \mathcal{H}_t, \mathcal{B}_t$, and $\boldsymbol{n}$ is the unit vector normal to $\mathcal{I}^{\alpha\beta}$. We emphasize that the conditions on $\boldsymbol{v}^{\mathrm{s}} \cdot \boldsymbol{n}$, ω^{N}, and p^{f} require these quantities to be continuous across the interface, whereas all other conditions are interface balance laws.

4.2.2 Stress tensor and mechanical response

To assess the mechanical response of the system considered in this work, it is crucial to remark that, similarly to K_t, also an undeformed (reference) configuration of the whole system, K_0, can be determined. The latter can be written as the disjoint union $K_0 = \mathcal{T}_0 \sqcup \mathcal{H}_0 \sqcup \mathcal{B}_0$. Here, $\mathcal{T}_0$, $\mathcal{H}_0$, and $\mathcal{B}_0$ denote, respectively, the subdomains occupied by the tumor tissue, the soft host tissue, and the bone, each in its undeformed (sub)configuration. By introducing the solid motion as the one-parameter of mappings

$$\chi^{\mathrm{s}}(\,\cdot\,,t) : K_0 \to \mathbf{R}^3, \quad X \mapsto x = \chi^{\mathrm{s}}(X,t) \in K_t \subset \mathbf{R}^3, \tag{4.32}$$

where $\mathbf{R}^3$ denotes here the three-dimensional Euclidean space, it is possible to map the global reference configuration K_0 into $K_t = \chi^{\mathrm{s}}(K_0,t)$. More specifically, the mappings $\chi^{\mathrm{s}}(\,\cdot\,,t)$ are continuous throughout K_0, which means that the subdomains $\mathcal{T}_0$, $\mathcal{H}_0$, and $\mathcal{B}_0$ are mapped into $\mathcal{T}_t = \chi^{\mathrm{s}}(\mathcal{T}_0,t)$, $\mathcal{H}_t = \chi^{\mathrm{s}}(\mathcal{H}_0,t)$, and $\mathcal{B}_t = \chi^{\mathrm{s}}(\mathcal{B}_0,t)$, respectively. Moreover, vectors attached to the points X of the subdomains $\mathcal{T}_0$, $\mathcal{H}_0$, and $\mathcal{B}_0$ are mapped into vectors attached to the points $x = \chi^{\mathrm{s}}(X,t)$ of $\mathcal{T}_t$, $\mathcal{H}_t$, and $\mathcal{B}_t$ through the deformation gradient tensor $\boldsymbol{F}$, whose components are expressed by $F_{iI} = \partial\chi^{\mathrm{s}}_i/\partial X_I$, $i,I = 1,2,3$, in appropriate coordinate systems. However, since $\chi^{\mathrm{s}}(\,\cdot\,,t)$ is generally not differentiable over all K_0 (see the interface condition (4.26)), but only piecewise differentiable (i.e., differentiable in each subdomain), the tensor $\boldsymbol{F}$ is piecewise continuous in K_0 and, consequently, it has to be defined separately for each subdomain.

Because of the growth and remodeling occurring in the system, which lead to variations of mass and shape as well as to a reorganization of its internal structure, the global undeformed configuration K_0 is generally not stress-free. To achieve a stress-free state (also referred to as *natural state* in the literature), K_t (or K_0) should be torn up in small stress-free pieces. However, since the particles constituting the subdomains of K_t have different material properties (indeed, neither K_t nor K_0 represent a uniform body), each of its subdomains must be brought to a natural state that is in general different from the other ones. To this end, we denote by $\mathcal{T}_\nu$, $\mathcal{H}_\nu$, and $\mathcal{B}_\nu$ the collections of stress-free body elements of $\mathcal{T}_t$, $\mathcal{H}_t$, and $\mathcal{B}_t$, respectively. In particular, we notice that, since the bone is assumed to undergo neither growth nor remodeling, the collection $\mathcal{B}_\nu$ may be identified with the undeformed configuration $\mathcal{B}_0$.

A fundamental hypothesis of our model is that both the tumor and the soft host tissue exhibit hyperelastic behavior from the relaxed states $\mathcal{T}_\nu$ and $\mathcal{H}_\nu$, respectively.

To account for this constitutive prescription in conjunction with growth and structural evolution, we invoke the theory of evolving natural "configurations" [87]. We start with the description of the mechanical response of the tumor. As anticipated above, we consider the mechanical evolution of this tissue as dictated by three phenomena: growth, plastic reorganization, and elastic distortion. Hence, we introduce the multiplicative decomposition of the deformation gradient tensor $\boldsymbol{F}$ [15, 103, 52, 108, 126], as:

$$\boldsymbol{F} = \boldsymbol{F}_{\mathrm{e}}\boldsymbol{F}_{\mathrm{a}} = \boldsymbol{F}_{\mathrm{e}}\boldsymbol{F}_{\mathrm{p}}\boldsymbol{F}_{\mathrm{g}}, \quad \text{in } \mathcal{T}_0. \tag{4.33}$$

In (4.33), $\boldsymbol{F}$ is related to the global change of shape of the body, $\boldsymbol{F}_{\mathrm{a}}$ represents the total anelastic distortions responsible for the evolution of the internal structure of the body, and $\boldsymbol{F}_{\mathrm{e}}$ describes the total elastic distortion. Note that $\boldsymbol{F}_{\mathrm{a}}$ maps vectors attached to $\mathcal{T}_0$ into vectors attached to $\mathcal{T}_\nu$, and $\boldsymbol{F}_{\mathrm{e}}$ map vectors of $\mathcal{T}_\nu$ into vectors of $\mathcal{T}_t$. To sketch the conceptual meaning of (4.33), we follow the explanation given in [75]. Hence, we consider a body that is brought from $\mathcal{T}_0$ to its current configuration $\mathcal{T}_t$ by the action of external loads. These, in general, are responsible for varying both the shape and the internal structure of the body in $\mathcal{T}_0$. If structural changes occur, it is not possible to bring back the body to $\mathcal{T}_0$ by simply removing the external loads. Rather, if all the external loads were switched off, the body would occupy a configuration, different from both $\mathcal{T}_t$ and $\mathcal{T}_0$, in which residual stresses may be present. To eliminate these, one should ideally tear the body into small disjoint pieces, and let each of them individually attain $\mathcal{T}_\nu$. Note that, as the body elements in $\mathcal{T}_\nu$ may turn out to be geometrically incompatible, $\mathcal{T}_\nu$ cannot be generally regarded as a configuration in Euclidean space. According to Figure 4.1, we can then split the map from $\mathcal{T}_0$ to $\mathcal{T}_\nu$ in two parts: the first, described by $\boldsymbol{F}_{\mathrm{g}}$, is related to growth and death processes, leading to possible changes in the mass of the volume element; the second, given by $\boldsymbol{F}_{\mathrm{p}}$, is due to internal reorganization of the body, in terms of rearranging of the adhesion bonds between the cells. The determinant J of the deformation gradient $\boldsymbol{F}$ can be written as:

$$J = J_{\mathrm{e}}J_{\mathrm{a}} = J_{\mathrm{e}}J_{\mathrm{p}}J_{\mathrm{g}}, \tag{4.34}$$

where $J_{\mathrm{i}} = \det(\boldsymbol{F}_{\mathrm{i}})$ and $\mathrm{i} = \mathrm{e}, \mathrm{p}, \mathrm{g}$. We assume $\boldsymbol{F}_{\mathrm{g}}$ to be purely volumetric, i.e. $\boldsymbol{F}_{\mathrm{g}} = g\boldsymbol{I}$, and $\boldsymbol{F}_{\mathrm{p}}$ to be purely isochoric. It follows that $J_{\mathrm{g}} = g^3$, while $J_{\mathrm{p}} = 1$.

In the sequel, we assume that the soft host tissue experiences remodeling (i.e., a plastic reorganization of its internal structure). Thus, we specialize the decomposition (4.33) to the case of no growth by setting

$$\boldsymbol{F} = \boldsymbol{F}_{\mathrm{e}}\boldsymbol{F}_{\mathrm{a}} = \boldsymbol{F}_{\mathrm{e}}\boldsymbol{F}_{\mathrm{p}}, \qquad \text{in } \mathcal{H}_0, \tag{4.35}$$

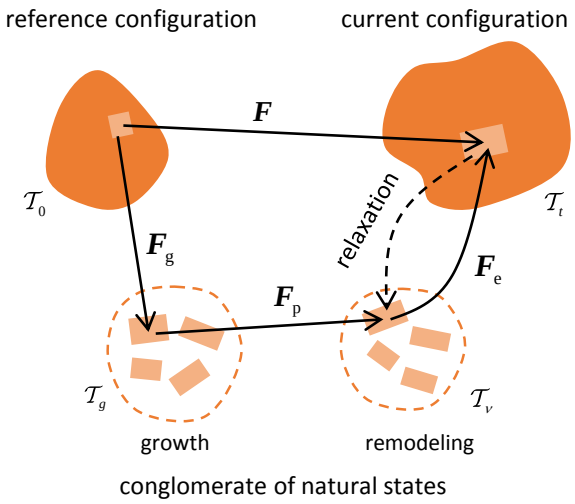

Figure 4.1: Schematic representation of the multiplicative decomposition of the deformation gradient tensor.

with $\boldsymbol{F}_\mathrm{a} = \boldsymbol{F}_\mathrm{p}$. Again, the determinant of the deformation gradient will be given by:

$$J = J_\mathrm{e} J_\mathrm{a} = J_\mathrm{e} J_\mathrm{p}, \tag{4.36}$$

with $J_\mathrm{a} = J_\mathrm{p} = 1$. Note that the deformation gradient tensor is decomposed in the same manner both for the tumor and for the soft host tissue. However, in the latter we assume that no growth is present, leading to the identities $\boldsymbol{F}_\mathrm{g} = \boldsymbol{I}$ and $g = 1$.

The strain energy density of the system per unit volume of the undeformed configuration K_0 is denoted by

$$\mathcal{W}_0 = \begin{cases} J_\mathrm{a}\mathcal{W}_\nu^\mathrm{t} = J_\mathrm{p} J_\mathrm{g} \mathcal{W}_\nu^\mathrm{t}, & \text{in } \mathcal{T}_0, \\ J_\mathrm{a}\mathcal{W}_\nu^\mathrm{h} = J_\mathrm{p} \mathcal{W}_\nu^\mathrm{h}, & \text{in } \mathcal{H}_0, \\ \mathcal{W}_0^\mathrm{b}, & \text{in } \mathcal{B}_0, \end{cases} \tag{4.37}$$

where $\mathcal{W}_\nu^\mathrm{t}$ and $\mathcal{W}_\nu^\mathrm{h}$ are the energy densities per unit volume of the natural state of the tumor and of the soft host tissue, respectively, and $\mathcal{W}_0^\mathrm{b}$ is the energy density of the bone per unit volume of the undeformed configuration $\mathcal{B}_0$. We start with the description of the mechanical response of the tumor and of the soft host tissue. Since the materials are assumed to be isotropic, the strain energy densities can be written as a function of the first three invariants of the elastic right Cauchy-Green deformation tensor $\boldsymbol{C}_\mathrm{e} = \boldsymbol{F}_\mathrm{e}^T \boldsymbol{F}_\mathrm{e}$. In particular, we have

$$\mathcal{W}_\nu^\mathrm{i}(\boldsymbol{C}_\mathrm{e}) = \tilde{\mathcal{W}}_\nu^\mathrm{i}(I_1, I_2, I_3), \qquad \text{i=t,h,} \tag{4.38}$$

where

$$I_1 = \mathrm{tr}\left(\boldsymbol{C}_\mathrm{e}\right), \tag{4.39}$$

$$I_2 = \frac{1}{2}\left[I_1^2 - \mathrm{tr}\left(\boldsymbol{C}_\mathrm{e}^2\right)\right], \tag{4.40}$$

$$I_3 = \det\left(\boldsymbol{C}_\mathrm{e}\right), \tag{4.41}$$

and $\boldsymbol{C}_\mathrm{e}$ is expressed piecewise as

$$\boldsymbol{C}_\mathrm{e} = \boldsymbol{F}_\mathrm{a}^{-T}\boldsymbol{C}\boldsymbol{F}_\mathrm{a}^{-1} = \begin{cases} g^{-2}\boldsymbol{F}_\mathrm{p}^{-T}\boldsymbol{C}\boldsymbol{F}_\mathrm{p}^{-1}, & \text{in } \mathcal{T}_0, \\ \boldsymbol{F}_\mathrm{p}^{-T}\boldsymbol{C}\boldsymbol{F}_\mathrm{p}^{-1}, & \text{in } \mathcal{H}_0, \end{cases} \tag{4.42}$$

$$\mathrm{tr}\left(\boldsymbol{C}_e\right) = \mathrm{tr}\left(\boldsymbol{C}\boldsymbol{B}_\mathrm{a}\right) = \begin{cases} g^{-2}\mathrm{tr}\left(\boldsymbol{C}\boldsymbol{B}_\mathrm{p}\right), & \text{in } \mathcal{T}_0, \\ \mathrm{tr}\left(\boldsymbol{C}\boldsymbol{B}_\mathrm{p}\right), & \text{in } \mathcal{H}_0, \end{cases} \tag{4.43}$$

$$\boldsymbol{B}_\mathrm{a} = \boldsymbol{F}_\mathrm{a}^{-1}\boldsymbol{F}_\mathrm{a}^{-T} = \begin{cases} g^{-2}\boldsymbol{B}_\mathrm{p}, & \text{in } \mathcal{T}_0, \\ \boldsymbol{B}_\mathrm{p}, & \text{in } \mathcal{H}_0. \end{cases} \tag{4.44}$$

From the expression of the energy we can calculate the solid phase second Piola-Kirchhoff stress tensor associated with the natural state of the subdomains $\mathcal{T}_0$ and $\mathcal{H}_0$:

$$\begin{aligned} \boldsymbol{S}^\mathrm{i}_{\nu,\mathrm{eff}} &= 2\frac{\partial \mathcal{W}^\mathrm{i}_\nu}{\partial \boldsymbol{C}_\mathrm{e}} = \sum_{j=1}^{3} 2\frac{\partial \mathcal{W}^\mathrm{i}_\nu}{\partial I_j}\frac{\partial I_j}{\partial \boldsymbol{C}_\mathrm{e}} = \sum_{j=1}^{3} 2b^\mathrm{i}_j\frac{\partial I_j}{\partial \boldsymbol{C}_\mathrm{e}} \\ &= \left(2b^\mathrm{i}_1 + 2b^\mathrm{i}_2 I_1\right)\boldsymbol{I} - 2b^\mathrm{i}_2\boldsymbol{C}_\mathrm{e} + 2b^\mathrm{i}_3 I_3\boldsymbol{C}_\mathrm{e}^{-1}. \end{aligned} \tag{4.45}$$

with $b^\mathrm{i}_j = \frac{\partial \mathcal{W}^\mathrm{i}_\nu}{\partial I_j}$, and $\mathrm{i} = \mathrm{t}, \mathrm{h}$. Note that the second Piola-Kirchhoff stress tensor associated with the reference configuration can be obtained as the Piola transformation $\boldsymbol{S}^\mathrm{i}_\mathrm{eff} = J_\mathrm{a}\boldsymbol{F}_\mathrm{a}^{-1}\boldsymbol{S}^\mathrm{i}_{\nu,\mathrm{eff}}\boldsymbol{F}_\mathrm{a}^{-T}$.

When the material response of the tumor is considered, i.e., for $\mathrm{i} = \mathrm{t}$, the effective second Piola-Kirchhoff stress tensor is a constitutive function of $\boldsymbol{F}$, g, and $\boldsymbol{B}_\mathrm{p}$, i.e., $\boldsymbol{S}^\mathrm{t}_\mathrm{eff} = \boldsymbol{S}^\mathrm{t}_\mathrm{eff}\left(\boldsymbol{F}, g, \boldsymbol{B}_\mathrm{p}\right)$. Moreover, recalling that the plastic distortions are isochoric, i.e., $J_\mathrm{p} = 1$, we finally obtain

$$\boldsymbol{S}^\mathrm{t}_\mathrm{eff} = 2gb^\mathrm{t}_1\boldsymbol{B}_\mathrm{p} + 2b^\mathrm{t}_2\frac{1}{g}\left[\mathrm{tr}\left(\boldsymbol{C}\boldsymbol{B}_\mathrm{p}\right)\boldsymbol{B}_\mathrm{p} - \boldsymbol{B}_\mathrm{p}\boldsymbol{C}\boldsymbol{B}_\mathrm{p}\right] + 2b^\mathrm{t}_3\frac{J^2}{g^3}\boldsymbol{C}^{-1}. \tag{4.46}$$

It is worth to remark that, by virtue of the hypothesis of isotropy, the plastic behavior of the system can be formulated in terms of $\boldsymbol{B}_\mathrm{p}$, rather than $\boldsymbol{F}_\mathrm{p}$. Although, on the one hand, this leads to a loss of information, on the other hand, it brings about

important simplifications. In this work we assume the Holmes and Mow form [85] for the strain energy densities of the tumor and of the soft host tissue. This constitutive behavior is able to capture the mechanical characteristics of soft hydrated tissues and is expressed by the formula:

$$\mathcal{W}_\nu^{\mathrm{i}} = a_0^{\mathrm{i}} \left[\exp\left(\Psi\right) - 1\right], \ \Psi = a_1^{\mathrm{i}} \left(I_1 - 3\right) + a_2^{\mathrm{i}} \left(I_2 - 3\right) - \beta^{\mathrm{i}} \ln\left(I_3\right), \tag{4.47}$$

where i=t,h, and a_0^{i}, a_1^{i}, a_2^{i}, β^{i} are coefficients related to material properties, i.e.,

$$a_0^{\mathrm{i}} = \frac{2\mu^{\mathrm{i}} + \lambda^{\mathrm{i}}}{4}, \quad a_1^{\mathrm{i}} = \frac{2\mu^{\mathrm{i}} - \lambda^{\mathrm{i}}}{2\mu^{\mathrm{i}} + \lambda^{\mathrm{i}}}, \quad a_2^{\mathrm{i}} = \frac{\lambda^{\mathrm{i}}}{2\mu^{\mathrm{i}} + \lambda^{\mathrm{i}}}, \quad \beta^{\mathrm{i}} = a_1^{\mathrm{i}} + 2a_2^{\mathrm{i}}, \tag{4.48}$$

Here, λ^{i} and μ^{i} are the Lamé constants of the solid scaffold, and β^{i} is usually assumed to be one. In equation (4.46), b_j^{i}, $j = 1, 2, 3$, can be calculated from (4.45) as

$$b_1^{\mathrm{i}} = a_1^{\mathrm{i}} \left(\mathcal{W}_\nu^{\mathrm{i}} + a_0^{\mathrm{i}}\right), \tag{4.49}$$

$$b_2^{\mathrm{i}} = a_2^{\mathrm{i}} \left(\mathcal{W}_\nu^{\mathrm{i}} + a_0^{\mathrm{i}}\right), \tag{4.50}$$

$$b_3^{\mathrm{i}} = -\frac{\beta^{\mathrm{i}}}{I_3} \left(\mathcal{W}_\nu^{\mathrm{i}} + a_0^{\mathrm{i}}\right). \tag{4.51}$$

The relations in (4.49)-(4.51) can be substituted into the expression (4.46) for the solid stress in the reference configuration.

Concerning the effective stress of the bone tissue, we choose an energy density function of the Saint Venant-Kirchhoff type as

$$\mathcal{W}_0^{\mathrm{b}}(\boldsymbol{E}) = \mu^{\mathrm{b}} \operatorname{tr}(\boldsymbol{E}^2) + \frac{\lambda^{\mathrm{b}}}{2} [\operatorname{tr}(\boldsymbol{E})]^2, \tag{4.52}$$

where μ^{b} and λ^{b} are the shear modulus and the first Lamé parameter of the bone, respectively, and $\boldsymbol{E} = \frac{1}{2}(\boldsymbol{C} - \boldsymbol{I})$ is the Green-Lagrange strain tensor. Consequently, the constitutive part of the stress associated to the bone is given by

$$\boldsymbol{S}_{\mathrm{eff}}^{\mathrm{b}} = 2\mu^{\mathrm{b}}\, \boldsymbol{E} + \lambda^{\mathrm{b}} \operatorname{tr}(\boldsymbol{E}) \boldsymbol{I}. \tag{4.53}$$

The momentum equation (4.17) of the whole biphasic system rephrases, in the material configuration, as

$$\operatorname{Div}\left(\boldsymbol{P}_{\mathrm{eff}}^{\mathrm{s}} - J p^{\mathrm{f}} \boldsymbol{F}^{-T}\right) = 0, \tag{4.54}$$

where $\operatorname{Div}(\cdot)$ denotes the material divergence operator, and $\boldsymbol{P}_{\mathrm{eff}}^{\mathrm{s}} = \boldsymbol{F}\boldsymbol{S}_{\mathrm{eff}}^{\mathrm{s}}$. Note that, in the civil engineering framework, the pressure p^{f} is often identified with the fluid pressure, and it is usually multiplied by the Biot coefficient α_{B} (here taken equal to

one) [111]. Since the system is subdivided into different tissue compartments, the stress can be evaluated as

$$\boldsymbol{S}^{\mathrm{s}}_{\mathrm{eff}} = \begin{cases} \boldsymbol{S}^{\mathrm{t}}_{\mathrm{eff}}, & \text{in } \mathcal{T}_0, \\ \boldsymbol{S}^{\mathrm{h}}_{\mathrm{eff}}, & \text{in } \mathcal{H}_0, \\ \boldsymbol{S}^{\mathrm{b}}_{\mathrm{eff}}, & \text{in } \mathcal{B}_0. \end{cases} \tag{4.55}$$

where the three $\boldsymbol{S}^{\mathrm{i}}_{\mathrm{eff}}$ have been defined in (4.46) and (4.53), respectively.

The last equation in the model is the one governing the plastic distortions. This can be expressed in terms of the time derivative of $\boldsymbol{B}_{\mathrm{p}}$ as [6, 66, 67, 75, 76]:

$$\dot{\boldsymbol{B}}_{\mathrm{p}} = -\frac{2\lambda_{\mathrm{p}}}{\|\mathrm{dev}\,(\boldsymbol{\sigma}^{\mathrm{s}}_{\mathrm{eff}})\|}\left\langle \|\mathrm{dev}\,(\boldsymbol{\sigma}^{\mathrm{s}}_{\mathrm{eff}})\| - \sqrt{2/3}\sigma_{\mathrm{y}} \right\rangle_{+} \boldsymbol{B}_{\mathrm{p}}\,\mathrm{dev}\,(\boldsymbol{\Sigma}^{\mathrm{s}}_{\mathrm{eff}})\,, \tag{4.56}$$

where we denote by $\mathrm{dev}(\cdot)$ the deviatoric part of the tensor to which it is applied ($\mathrm{i} = \mathrm{t}, \mathrm{h}$). Note that the use of $\boldsymbol{B}_{\mathrm{p}}$, rather than $\boldsymbol{F}_{\mathrm{p}}$, as a measure of plastic deformations is allowed by the hypothesis of material isotropy [121, 169, 75]. In (4.56), $\boldsymbol{\sigma}^{\mathrm{s}}_{\mathrm{eff}}$ is the effective Cauchy stress in the solid phase, obtained from the second Piola-Kirchhoff tensor by the Piola transformation:

$$\boldsymbol{\sigma}^{\mathrm{s}}_{\mathrm{eff}} = \frac{1}{J}\boldsymbol{F}\boldsymbol{S}^{\mathrm{s}}_{\mathrm{eff}}\boldsymbol{F}^{T}. \tag{4.57}$$

Then, σ_{y} is the yield stress, above which the plastic flow starts (as indicated by the Macaulay brackets $\langle\cdot\rangle_{+}$ such that $\langle f\rangle_{+} = f$ if $f > 0$ and $\langle f\rangle_{+} = 0$ otherwise). Finally, $\boldsymbol{\Sigma}^{\mathrm{s}}_{\mathrm{eff}}$ is the material Mandel stress tensor in the solid phase, given by $\boldsymbol{\Sigma}^{\mathrm{s}}_{\mathrm{eff}} = \boldsymbol{F}^{T}\boldsymbol{P}^{\mathrm{s}}_{\mathrm{eff}}$. This remodeling activates in the tumor and in the soft host tissue, with a different value of the yield stress for each tissue ($\sigma^{\mathrm{t}}_{\mathrm{y}}$ and $\sigma^{\mathrm{h}}_{\mathrm{y}}$, respectively).

Notice that the equation for the plastic flow constitutes a phenomenological description of what happens at the cell scale: If we consider a cluster of cells subjected to a sufficiently high tension, some of their adhesive bonds may break and reform in other places. The mechanical energy required by the system for breaking the bonds and reforming them in other places is not stored, being dissipated during the process. Moreover, a cell aggregate subjected to a given load after reorganization will respond elastically for small loads, as long as the bonds are not broken again [6]. The law in (4.56) is thus stating the following: if the stress in the material is below a given threshold, denoted here by σ_{y}, then the derivative of $\boldsymbol{B}_{\mathrm{p}}$ is zero and no plastic flow occurs. When the stress exceeds the threshold, the material evolves to release the stress in excess, until the yield stress is reached or exceeded again. The parameter λ_{p} gives an indication of the characteristic time for cell reorganization and the following stress relaxation.

4.2.3 Constitutive relations for the mass exchange terms

The exchange term Γ^{s} appearing in equation (4.4) is related to tumor cell proliferation and death. Recalling equation (4.7), it is given by the sum of $\Gamma_{\mathrm{p}}^{\mathrm{f}\to\mathrm{p}}$ and $\Gamma_{\mathrm{n}}^{\mathrm{n}\to\mathrm{f}}$. The first quantity describes tumor growth and reads

$$\Gamma_{\mathrm{p}}^{\mathrm{f}\to\mathrm{p}} = \gamma_{\mathrm{fp}}^{\mathrm{p}} \left\langle \frac{\omega^{\mathrm{N}} - \omega_{\mathrm{cr}}^{\mathrm{N}}}{\omega_{\mathrm{env}}^{\mathrm{N}} - \omega_{\mathrm{cr}}^{\mathrm{N}}} \right\rangle_{+} \left(1 - \frac{\delta_1 \langle \bar{\sigma}_{\mathrm{eff}}^{\mathrm{s}} \rangle_{+}}{\langle \bar{\sigma}_{\mathrm{eff}}^{\mathrm{s}} \rangle_{+} + \delta_2} \right) \frac{\varepsilon^{\mathrm{f}}}{\varepsilon_0^{\mathrm{f}}} \omega^{\mathrm{p}} \varepsilon^{\mathrm{s}}, \tag{4.58}$$

where the coefficient $\gamma_{\mathrm{fp}}^{\mathrm{p}} \geq 0$ accounts for the nutrient uptake and for the mass of the interstitial fluid that becomes tumor due to cell growth, $\omega_{\mathrm{cr}}^{\mathrm{N}}$ is the critical level of oxygen below which cell proliferation is inhibited, $\omega_{\mathrm{env}}^{\mathrm{N}}$ is the mass fraction of oxygen in the environment, $\bar{\sigma}_{\mathrm{eff}}^{\mathrm{s}}$ is the spherical part of the effective Cauchy stress tensor associated with the solid phase, i.e., $\bar{\sigma}_{\mathrm{eff}}^{\mathrm{s}} = -\mathrm{tr}(\boldsymbol{\sigma}_{\mathrm{eff}}^{\mathrm{s}})/3$, and the positive constants δ_1 and δ_2 (with $\delta_1 < 1$) account for the action of mechanical stress on cell proliferation. Due to its form, the term in parentheses in (4.58) describes growth inhibition due to tumor compression. Finally, $\varepsilon_0^{\mathrm{f}}$ is the initial volume fraction of the fluid phase. The second part of Γ^{s}, namely $\Gamma_{\mathrm{n}}^{\mathrm{n}\to\mathrm{f}}$, takes the form:

$$\Gamma_{\mathrm{n}}^{\mathrm{n}\to\mathrm{f}} = -\gamma_{\mathrm{nf}}^{\mathrm{n}} \omega^{\mathrm{n}} \varepsilon^{\mathrm{s}}. \tag{4.59}$$

This term is related to cell death from lysis in the necrotic population of the tumor. The coefficient $\gamma_{\mathrm{nf}}^{\mathrm{n}}$ takes into account the degradation of cellular membranes and the mass conversion into interstitial fluid. Then, the rate of tumor cell death in equation (4.2) is described by the relation

$$\Gamma_{\mathrm{p}}^{\mathrm{p}\to\mathrm{n}} = -\gamma_{\mathrm{pno}}^{\mathrm{p}} \left\langle 1 - \frac{\omega^{\mathrm{N}}}{\omega_{\mathrm{cr}}^{\mathrm{N}}} \right\rangle_{+} \omega^{\mathrm{p}} \varepsilon^{\mathrm{s}}, \tag{4.60}$$

where the parameter $\gamma_{\mathrm{pno}}^{\mathrm{p}}$ is related to the rate of cell necrosis. In this way, we assume cell death to occur solely by nutrient deprivation. Finally, nutrient consumption by tumor cells is described by:

$$\Gamma_{\mathrm{N}}^{\mathrm{N}\to\mathrm{p}} = -\gamma_{\mathrm{Np1}}^{\mathrm{N}} \frac{\omega^{\mathrm{N}}}{\omega^{\mathrm{N}} + \gamma_{\mathrm{Np2}}^{\mathrm{N}}} \omega^{\mathrm{p}} \varepsilon^{\mathrm{s}}. \tag{4.61}$$

Here, $\gamma_{\mathrm{Np1}}^{\mathrm{N}}$ and $\gamma_{\mathrm{Np2}}^{\mathrm{N}}$ are two coefficients regulating nutrient uptake by the cells. Note that the mathematical expressions adopted for the mass exchange terms are similar to the ones reported in Section 3.1, validated with data from tumor spheroid experiments.

4.2.4 Summary of the model equations

In this Section, we summarize the final form of the equations of the model. A thorough derivation is available in Appendix A. Granted that ε^{s} can be expressed as

$$\varepsilon^{\mathrm{s}} = \frac{g^3 \varepsilon^{\mathrm{s}}_{\nu}}{J}, \tag{4.62}$$

where $\varepsilon^{\mathrm{s}}_{\nu}$ is the solid volume fraction in the natural state, the final system of equations to be solved is given by

$$\frac{\dot{g}}{g} = \frac{1}{3}\frac{\Gamma^{\mathrm{s}}}{\varepsilon^{\mathrm{s}}\rho}, \tag{4.63}$$

$$\dot{\omega}^{\mathrm{p}} = \frac{J}{\rho \varepsilon^{\mathrm{s}}_{\nu} g^3}\left(\Gamma^{\mathrm{p}\to\mathrm{n}}_{\mathrm{p}} + \Gamma^{\mathrm{f}\to\mathrm{p}}_{\mathrm{p}} - \omega^{\mathrm{p}}\Gamma^{\mathrm{s}}\right), \tag{4.64}$$

$$J\varepsilon^{\mathrm{f}}\rho\dot{\omega}^{\mathrm{N}} + \rho \boldsymbol{Q}\cdot \mathrm{Grad}\,\omega^{\mathrm{N}} + \mathrm{Div}\left(\boldsymbol{\Psi}^{\mathrm{N}}\right) = J\left(\Gamma^{\mathrm{N}\to\mathrm{p}}_{\mathrm{N}} + \omega^{\mathrm{N}}\Gamma^{\mathrm{s}}\right), \tag{4.65}$$

$$\mathrm{Div}\left(\boldsymbol{Q}\right) + \dot{J} = 0, \tag{4.66}$$

$$\mathrm{Div}\left(\boldsymbol{P}^{\mathrm{s}}_{\mathrm{eff}} - Jp^{\mathrm{f}}\boldsymbol{F}^{-T}\right) = 0, \tag{4.67}$$

$$\dot{\boldsymbol{B}}_{\mathrm{p}} = -\frac{2\lambda_{\mathrm{p}}}{\|\mathrm{dev}\left(\boldsymbol{\sigma}^{\mathrm{s}}_{\mathrm{eff}}\right)\|}\left\langle \|\mathrm{dev}\left(\boldsymbol{\sigma}^{\mathrm{s}}_{\mathrm{eff}}\right)\| - \sqrt{2/3}\sigma_{\mathrm{y}}\right\rangle_{+}\boldsymbol{B}_{\mathrm{p}}\,\mathrm{dev}\left(\boldsymbol{\Sigma}^{\mathrm{s}}_{\mathrm{eff}}\right), \tag{4.68}$$

where we introduced the Piola transformations of Darcy's filtration velocity and Fick's mass flux

$$\boldsymbol{Q} = J\boldsymbol{F}^{-1}\varepsilon^{\mathrm{f}}\left(\boldsymbol{v}^{\mathrm{f}} - \boldsymbol{v}^{\mathrm{s}}\right) = -J\boldsymbol{F}^{-1}\boldsymbol{k}\boldsymbol{F}^{-T}\mathrm{Grad}\,p^{\mathrm{f}}, \tag{4.69}$$

$$\boldsymbol{\Psi}^{\mathrm{N}} = -J\varepsilon^{\mathrm{f}}\rho\boldsymbol{F}^{-1}\boldsymbol{D}^{\mathrm{N}}\boldsymbol{F}^{-T}\mathrm{Grad}\,\omega^{\mathrm{N}}. \tag{4.70}$$

The system in (4.63)-(4.68) is to be solved for the free unknowns

$$\mathcal{U} = \{g, \omega^{\mathrm{p}}, \omega^{\mathrm{N}}, p^{\mathrm{f}}, \chi^{\mathrm{s}}, \boldsymbol{B}_{\mathrm{p}}\}. \tag{4.71}$$

Note that the system is closed, since it features 13 scalar unknowns and (4.63)-(4.68) constitute a set of 13 scalar equations. In (4.69) and (4.70), $\boldsymbol{k}$ and $\boldsymbol{D}^{\mathrm{N}}$ are two isotropic tensors describing nutrient diffusivity and tissue hydraulic conductivity. They are given by the expressions $\boldsymbol{k} = k\boldsymbol{I}$ and $\boldsymbol{D}^{\mathrm{N}} = D^{\mathrm{N}}\boldsymbol{I}$, respectively. The equations (4.63)-(4.70) are obtained under the hypotheses that the mass densities of the fluid and solid phases are constant and equal ($\rho^{\mathrm{s}} = \rho^{\mathrm{f}} = \rho$). In the following, we consider only one nutrient species, namely oxygen.

4.3 Benchmark case for tissue compression

In this Section, we test the model on a simple case, namely the unconfined compression of a tissue specimen. We neglect the influence of growth, consider only one cellular species, and do not include nutrient transport in our description of the problem. The set of equations reduces to:

$$\dot{J} - \mathrm{Div}\left(\boldsymbol{K}\mathrm{Grad}\, p^{\mathrm{f}}\right) = 0, \tag{4.72}$$

$$\mathrm{Div}\left(\boldsymbol{P}^{\mathrm{s}}_{\mathrm{eff}} - Jp^{\mathrm{f}}\boldsymbol{F}^{-T}\right) = 0, \tag{4.73}$$

$$\dot{\boldsymbol{B}}_{\mathrm{p}} = -\frac{2\lambda_{\mathrm{p}}}{\|\mathrm{dev}\,(\boldsymbol{\sigma}^{\mathrm{s}}_{\mathrm{eff}})\|}\left\langle \|\mathrm{dev}\,(\boldsymbol{\sigma}^{\mathrm{s}}_{\mathrm{eff}})\| - \sqrt{2/3}\sigma^{\mathrm{t}}_{\mathrm{y}}\right\rangle_{+}\boldsymbol{B}_{\mathrm{p}}\,\mathrm{dev}\,(\boldsymbol{\Sigma}^{\mathrm{s}}_{\mathrm{eff}})\,, \tag{4.74}$$

where $\boldsymbol{K}$ is defined, according to (4.69), as $\boldsymbol{K} = J\boldsymbol{F}^{-1}\boldsymbol{k}\boldsymbol{F}^{-T}$.

In this benchmark, a tissue sample is inserted between two rigid and impermeable parallel plates, and is compressed according to some prescribed loading protocol. During compression, the boundaries that are not in contact with the plates can expand freely, allowing the fluid to flow out from the specimen. Similarly to [76], we consider a cylindrical specimen of biphasic material. Enforcing axial symmetry, we characterize the cylinder by an initial height of $h_0 = 1$ mm and an initial radius of $r_0 = 1.5$ mm. The lower boundary of the specimen is clamped at the lower plate of the experimental apparatus and is kept fixed. Instead, the upper boundary is in contact with the moving plate, and is assumed to expand frictionless. Finally, the lateral boundary of the specimen is regarded as traction-free and permeable to fluid flow. The geometry of the problem and the boundary conditions are then summarized in Figure 4.2.

For the initial conditions, we select the following set over the whole domain:

$$p^{\mathrm{f}} = 0, \quad \boldsymbol{B}_{\mathrm{p}} = \boldsymbol{I}, \quad J = 1. \tag{4.75}$$

For the upper plate, we consider the loading condition in Figure 4.3, where h is the vertical component of the solid displacement. In the simulations, we take the final displacement h_{c} to be 0.15 mm, and the final instant of time of the loading ramp as $t_{\mathrm{r}} = 30$ s. The material parameters used for this case are reported in Table 4.1. Figure 4.4 highlights the influence of plastic distortions on the mechanical and fluid dynamic response of the specimen. In Figures 4.4.a-b, we compare the fluid pressure distribution and the spherical part of the solid effective Cauchy stress tensor ($\bar{\sigma}^{\mathrm{s}}_{\mathrm{eff}}$) obtained in the poroelastic case (left column), with those obtained in the presence of plastic distortions (right column). To simulate the poroelastic case, we used a value

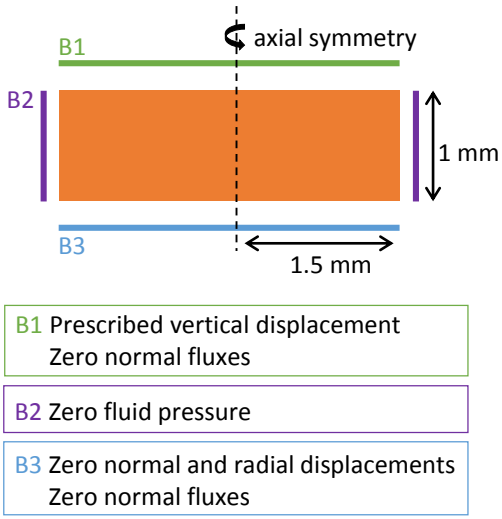

Figure 4.2: Geometry and boundary conditions for the compression benchmark.

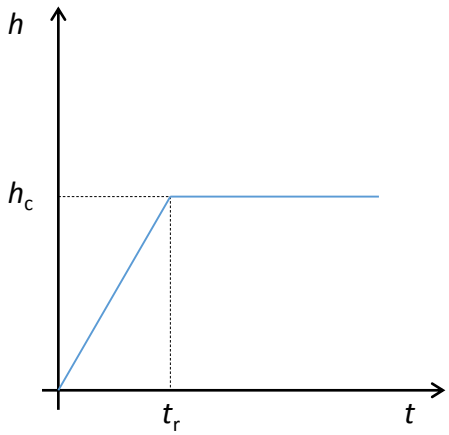

Figure 4.3: Loading condition for the upper plate in the compression benchmark.

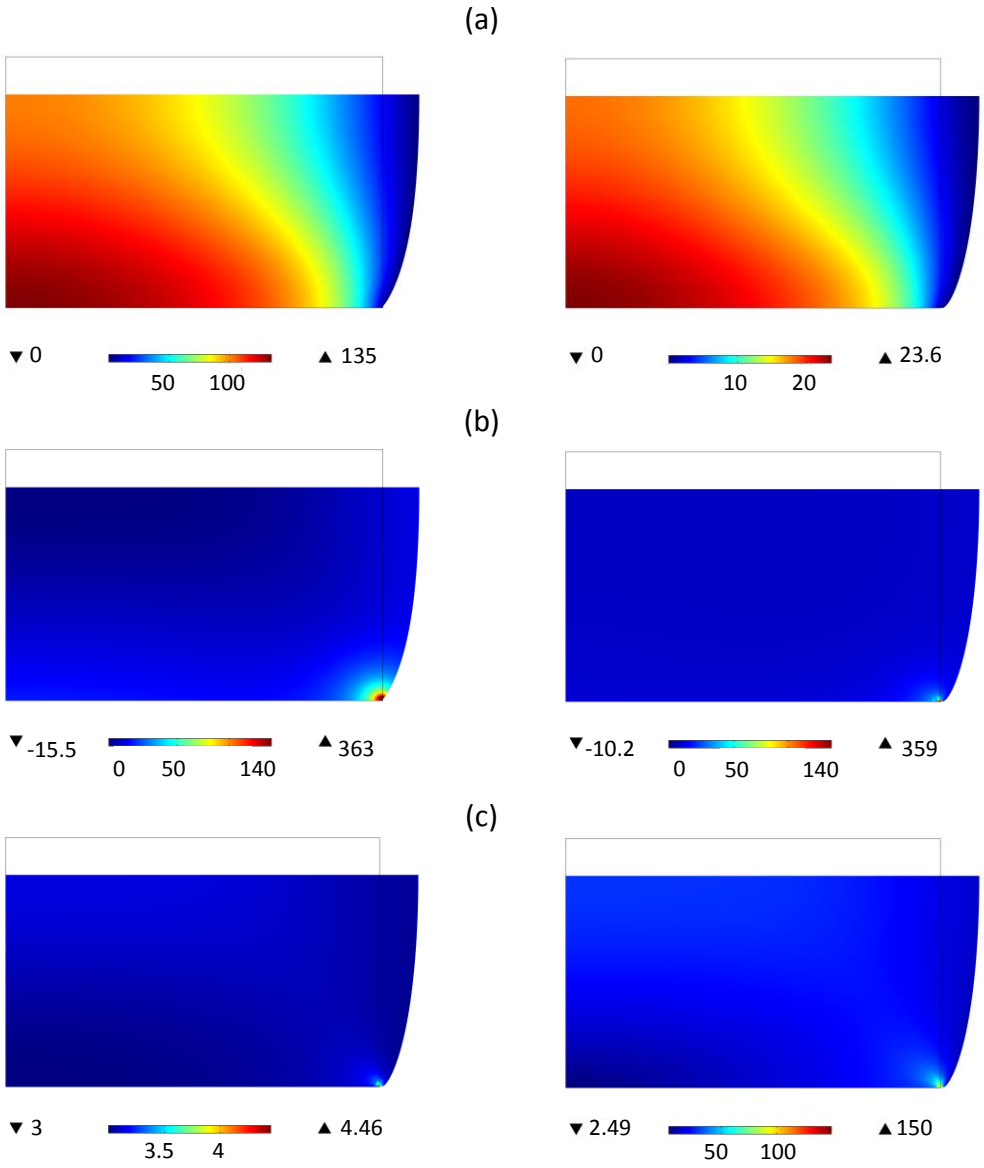

Figure 4.4: Comparison of the results for the compression benchmark in the absence and in the presence of plastic remodeling. All quantities are plotted in the deformed configuration of the specimen at time $t = t_r$. (a) p^f in the poroelastic (left) and poroplastic (right) case. (b) $\bar{\sigma}^s_{\text{eff}}$ in the poroelastic (left) and poroplastic (right) case. (c) Von Mises effective stress (left) and trace of $\boldsymbol{B}_p$ (right) in the poroplastic case.

Table 4.1: Model parameters for the compression benchmark.

Symbol	Parameter	Reference value	Unit
K^{t}	Tissue bulk modulus	2.033×10^{5}	Pa
μ^{t}	Tissue shear modulus	2.225×10^{5}	Pa
k	Tissue hydraulic conductivity	3.772×10^{-15}	$\mathrm{m}^2/(\mathrm{Pa} \cdot \mathrm{s})$
$\varepsilon_{\nu}^{\mathrm{s}}$	Solid volume fraction in natural state	0.2	$(-)$
$\sigma_{\mathrm{y}}^{\mathrm{t}}$	Yield stress	2.0×10^{3}	Pa
λ_{p}	Coefficient in the plastic flow rule	5.0×10^{-7}	$1/(\mathrm{Pa} \cdot \mathrm{s})$

for the yield stress that is never reached by the stress in the tissue. In particular, we set $\sigma_{\mathrm{y}}^{\mathrm{t}} = 1.0 \times 10^{20}$ Pa, a value leading to a pure elastic response. For this situation, it holds that $\boldsymbol{B}_{\mathrm{p}} = \boldsymbol{I}$ at all observed times. Instead, the stress exceeds the yield threshold in the poroplastic case, and $\boldsymbol{B}_{\mathrm{p}}$ evolves according to (4.74). This is shown in Figure 4.4.c, displaying the von Mises effective stress (left) and the first principal invariant of $\boldsymbol{B}_{\mathrm{p}}$ (right) at the end of the loading ramp.

The influence of remodeling is shown through the modulation of the fluid pressure distribution (Figure 4.4.a) and the lowering of the solid effective stress (Figure 4.4.b). Interestingly, the evolution of plastic distortions affects the time trend of pressure both in a qualitative and quantitative way. In Figure 4.5, the fluid pressure is evaluated at the point of the lower boundary of the specimen lying on the symmetry axis. Solid and dashed lines indicate the poroelastic and poroplastic case, respectively. It is

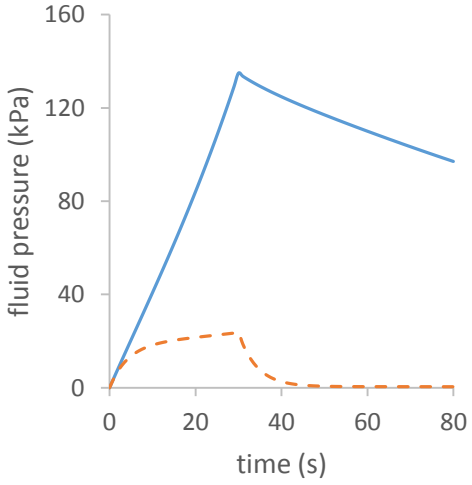

Figure 4.5: Time evolution of the fluid pressure for the compression benchmark. The poroelastic and poroplastic cases are represented by solid and dashed lines, respectively.

possible to notice that the fluid pressure attains its maximum at the end of the ramp load in both the cases, but the maximum value in the poroelastic case is higher than the one reached in the presence of remodeling. Also, the rate at which the pressure tends to the stationary state appears much higher in the poroplastic case than in the poroelastic one. These observations may result from the coupled nature of equations (4.72)-(4.74). Indeed, the balance of momentum (4.73) relates the fluid pressure p^{f} to the solid effective stress $\boldsymbol{P}^{\mathrm{s}}_{\mathrm{eff}}$. This quantity is in turn influenced by the evolution of the plastic distortions $\boldsymbol{B}_{\mathrm{p}}$, explaining the different behavior of the curves in Figure 4.5.

4.4 Benchmark cases for the tumor tissue

4.4.1 Introduction to the three cases

Hereafter, three benchmark tests are discussed. In the first case, we consider a tumor spheroid growing in the culture medium. In the second benchmark, the spheroid grows in a soft host tissue having spherical structure. Finally, in a third benchmark, we present the results of a tumor growing in a three-dimensional heterogeneous domain, in which the host tissue comprises both a soft material and a stiffer one, identified with a bone tissue.

In the first case, the model consists of a sphere segment in axisymmetric conditions. The spheroid has an initial radius of 100 μm and the initial solid volume fraction ε^{s} is fixed at 0.8 over the domain. We assume the following initial conditions:

$$g = 1, \quad \omega^{\mathrm{p}} = 1, \quad \omega^{\mathrm{N}} = \omega^{\mathrm{N}}_{\mathrm{env}}, \quad p^{\mathrm{f}} = 0, \quad \boldsymbol{B}_{\mathrm{p}} = \boldsymbol{I}, \quad \text{in } \mathcal{T}_0. \tag{4.76}$$

Moreover, the boundary conditions for the problem are summarized in Figure 4.6. On the outer boundary of the spheroid, we assume a fixed value ($\omega^{\mathrm{N}}_{\mathrm{env}}$) for the nutrient mass fraction and zero interstitial fluid pressure. Due to symmetry, no-flux boundary conditions are imposed normal to the radius of the sphere segment.

The parameters used for this first benchmark test come from different sources, and are reported in Table 4.2. Regarding the values used for the plastic flow rule, we have referred to the work of Iordan *et al.* [88] for an estimate of the yield stress in the tumor tissue. In addition, the value for the coefficient λ_{p} is derived from the cell reorganization time τ_{p} by the expression:

$$\tau_{\mathrm{p}} \simeq \frac{1}{\mu^{\mathrm{t}} \lambda_{\mathrm{p}}},$$

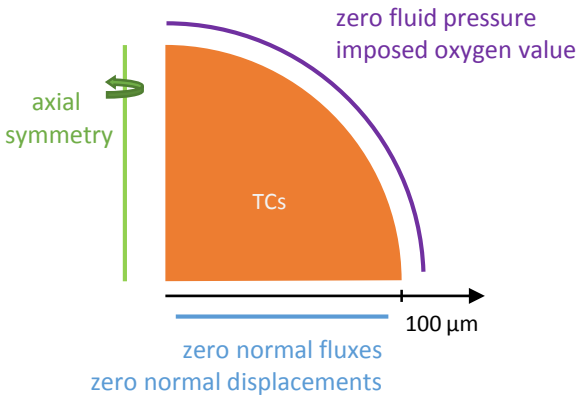

Figure 4.6: Geometry of the problem and boundary conditions for a tumor spheroid.

Table 4.2: Parameters used in the model for the tumor spheroid.

Symbol	Parameter	Unit	Value	Reference
$\varepsilon_{\nu}^{\mathrm{s}}$	Solid volume fraction in the natural state	$(-)$	8.0×10^{-1}	[66]
ρ	Density of the phases	$\mathrm{kg/m^3}$	1.0×10^{3}	[167]
k	Tumor hydraulic conductivity	$\mathrm{m^2/(Pa \cdot s)}$	4.875×10^{-13}	[159]
D^{N}	Nutrient diffusion coefficient	$\mathrm{m^2/s}$	3.2×10^{-9}	[167]
$\omega_{\mathrm{cr}}^{\mathrm{N}}$	Critical level of nutrient	$(-)$	2.0×10^{-6}	[120]
$\omega_{\mathrm{env}}^{\mathrm{N}}$	Environmental level of nutrient	$(-)$	7.0×10^{-6}	[134, 133]
$\gamma_{\mathrm{Np1}}^{\mathrm{N}}$	Coefficient related to nutrient consumption	$\mathrm{kg/(m^3 \cdot s)}$	3.0×10^{-4}	[30, 31]
$\gamma_{\mathrm{Np2}}^{\mathrm{N}}$	Coefficient related to nutrient consumption	$(-)$	1.48×10^{-7}	[30, 31]
$\gamma_{\mathrm{fp}}^{\mathrm{p}}$	Coefficient related to growth	$\mathrm{kg/(m^3 \cdot s)}$	5.348×10^{-3}	[65]
$\gamma_{\mathrm{pno}}^{\mathrm{p}}$	Coefficient related to necrosis	$\mathrm{kg/(m^3 \cdot s)}$	1.5×10^{-1}	[120]
$\gamma_{\mathrm{nf}}^{\mathrm{n}}$	Coefficient related to lysis	$\mathrm{kg/(m^3 \cdot s)}$	1.15×10^{-2}	[120]
λ_{p}	Coefficient related to cell reorganization time	$\mathrm{1/(Pa \cdot s)}$	8.334×10^{-7}	[56]
$\sigma_{\mathrm{y}}^{\mathrm{t}}$	Yield stress	Pa	1.0×10^{1}	[88]
λ^{t}	Lamé's first parameter for the tumor	Pa	1.333×10^{4}	[159]
μ^{t}	Shear modulus for the tumor	Pa	1.999×10^{4}	[159]
δ_1	Coefficient related to growth inhibition	$(-)$	7.138×10^{-1}	[120]
δ_2	Coefficient related to growth inhibition	Pa	1.541×10^{3}	[120]

where we have considered a value for τ_{p} of the order of one minute, consistently with the observations of Forgacs and colleagues [56]. The equations in the model were solved using the finite element software COMSOL Multiphysics® (COMSOL AB, Sweden).

In the second case, we consider the growth of an avascular tumor within a healthy tissue. As mentioned in the previous section, the soft host tissue is modeled as an elasto-visco-plastic solid where the elastic strain energy and the plastic flow rule are

characterized by the same constitutive relations of the tumor. However, an independent set of parameters is used for the healthy tissue, providing a different mechanical response. At the interfaces between the different domains, COMSOL applies automatically the conditions in (4.26). The geometry and boundary conditions of the problem are shown in Figure 4.7. Similar to the numerical experiments in [167], the

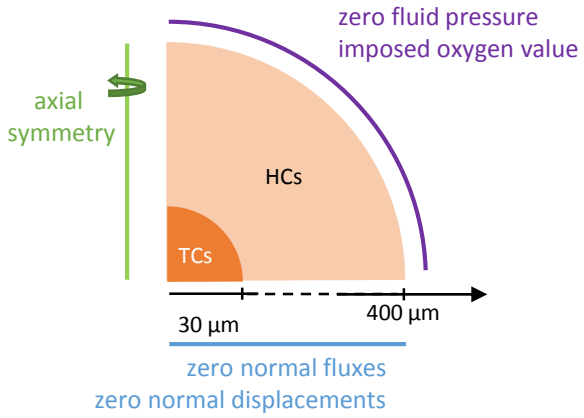

Figure 4.7: Geometry of the problem and boundary conditions for a tumor growing in a soft host tissue.

tumor and the host tissue are modeled as a sphere segment imposing cylindrical symmetry. The tumor occupies the region closer to the sphere center, with an initial radius of 30 μm. From there, the host tissue extends until the outer boundary of the computational domain, with an external radius of 400 μm. We consider an initial solid volume fraction equal to 0.7 throughout the domain. The initial conditions for the problem read:

$$g = 1, \quad \omega^{\mathrm{p}} = 1, \quad \text{in } \mathcal{T}_0, \tag{4.77}$$

$$\omega^{\mathrm{N}} = \omega^{\mathrm{N}}_{\mathrm{env}}, \quad p^{\mathrm{f}} = 0, \quad \boldsymbol{B}_{\mathrm{p}} = \boldsymbol{I}, \quad \text{in } \mathcal{T}_0 \sqcup \mathcal{H}_0. \tag{4.78}$$

Regarding the boundary conditions, the nutrient mass fraction and the interstitial fluid pressure on the outer boundary are set equal to $\omega^{\mathrm{N}}_{\mathrm{env}}$ and zero, respectively. To take into account the presence of a host tissue, we select a value for $\omega^{\mathrm{N}}_{\mathrm{env}}$ that corresponds to the average dissolved oxygen in the plasma of a healthy individual [167]. Moreover, in this second case the growth coefficient $\gamma^{\mathrm{p}}_{\mathrm{fp}}$ and the critical value of oxygen $\omega^{\mathrm{N}}_{\mathrm{cr}}$ take different values from before. On the other boundaries, zero flux is imposed for the nutrient and the fluid due to symmetry. The parameters pertaining to the healthy tissue are given in Table 4.3, whereas all the other parameters are the

Table 4.3: Parameters used for the case of a tumor growing in a soft host tissue.

Symbol	Parameter	Unit	Value	Reference
λ^{h}	Lamé's first parameter for the soft host tissue	Pa	3.336×10^3	[131]
μ^{h}	Shear modulus for the soft host tissue	Pa	5.0×10^3	[131]
$\sigma_{\mathrm{y}}^{\mathrm{h}}$	Yield stress for the soft host tissue[a]	Pa	1.0×10^3	-
λ_{p}	Coefficient related to cell reorganization time	$1/(\mathrm{Pa} \cdot \mathrm{s})$	8.334×10^{-8}	-
$\gamma_{\mathrm{fp}}^{\mathrm{p}}$	Coefficient related to growth	$\mathrm{kg}/(\mathrm{m}^3 \cdot \mathrm{s})$	8.022×10^{-3}	[62]
$\omega_{\mathrm{cr}}^{\mathrm{N}}$	Critical level of nutrient	$(-)$	1.0×10^{-6}	-
$\omega_{\mathrm{env}}^{\mathrm{N}}$	Environmental level of nutrient	$(-)$	4.2×10^{-6}	[167]

[a] Value assumed when plastic rearrangement in the soft host tissue is taken into account.

same as in Table 4.2. We assume that cellular bonds are more stable for a tumor grown in a host tissue than as a spheroid, and impose a larger time for cell rearrangement and a higher value for the healthy tissue yield stress.

As a last case, we analyze the growth of a tumor in proximity to a blood capillary and two different host tissues. The blood vessel constitutes the only source of nutrient, influencing the development and spatial configuration of the tumor. A tissue with the mechanical properties of a bone occupies a portion of the domain, whereas a soft host tissue fills the rest of the geometry. We consider the ideal geometry of Figure 4.8.a, where the capillary is close to a spherical tumor. The capillary has a diameter of 8 μm and the tumor starts with an initial diameter of 40 μm. This geometry has two planes of symmetry, allowing to discretize only one quarter of the actual domain. Figure 4.8.a shows the size of the other compartments of the problem. We enable plastic deformations to develop in the soft host tissue, as well as in the tumor, and fix the value of the yield stress of the soft host tissue as $\sigma_{\mathrm{y}}^{\mathrm{h}} = 10^3$ Pa. We assume a higher value for the cell reorganization time than in the previous case, leading to a lower value for λ_{p}. The initial conditions of the problem are stated below:

$$g = 1, \quad \omega^{\mathrm{p}} = 1, \quad \text{in } \mathcal{T}_0, \tag{4.79}$$

$$\boldsymbol{B}_{\mathrm{p}} = \boldsymbol{I}, \quad \text{in } \mathcal{T}_0 \sqcup \mathcal{H}_0, \tag{4.80}$$

$$\omega^{\mathrm{N}} = \omega_{\mathrm{cap}}^{\mathrm{N}}, \quad p^{\mathrm{f}} = 0, \quad \text{in } K_t. \tag{4.81}$$

Here $\omega_{\mathrm{cap}}^{\mathrm{N}}$ is the mass fraction of the nutrient supplied by the capillary. The boundary conditions for the problem are reported in Figure 4.8.b. In particular, the oxygen mass fraction is fixed on the cylindrical surfaces of the capillary, where we set it equal to $\omega_{\mathrm{cap}}^{\mathrm{N}}$. On the remaining lateral surfaces we impose zero oxygen flux. Because of

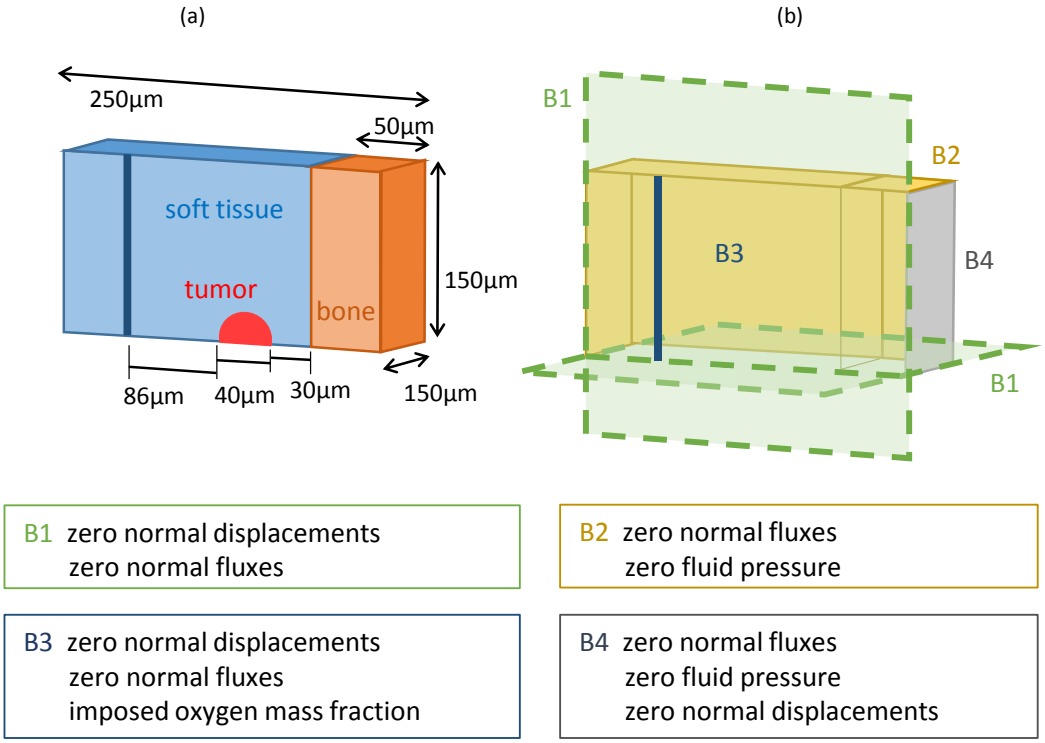

Figure 4.8: Geometry and boundary conditions for a tumor growing in a heterogeneous environment.

symmetry properties of the problem, our simulations consider only one quarter of the overall geometry, and we need to impose symmetry boundary conditions for the pressure and for the displacements on the surface $B1 \cap K_0$ of Fig. 4.8.

The additional parameters for this case, including the mechanical response of the bone tissue, are summarized in Table 4.4. For the latter, we assume a pure

Table 4.4: Additional parameters for the three-dimensional tumor model.

Symbol	Parameter	Unit	Value	Reference
λ^{b}	Lamé's first parameter for the bone tissue	Pa	5.769×10^{9}	[105, 94]
μ^{b}	Shear modulus for the bone tissue	Pa	3.846×10^{9}	[105, 94]
ε^{b}	Bone porosity	$(-)$	6.0×10^{-1}	[105, 94]
k^{b}	Bone hydraulic conductivity	$\mathrm{m}^2/(\mathrm{Pa} \cdot \mathrm{s})$	3.0×10^{-15}	[105, 94]
R_0	Tumor initial diameter	μm	40	-
$\omega^{\mathrm{N}}_{\mathrm{cap}}$	Capillary oxygen mass fraction	$(-)$	4.2×10^{-6}	[167]
$\omega^{\mathrm{N}}_{\mathrm{cr}}$	Critical oxygen mass fraction	$(-)$	3.0×10^{-6}	-
$\gamma^{\mathrm{p}}_{\mathrm{fp}}$	Coefficient related to growth	$\mathrm{kg}/(\mathrm{m}^3 \cdot \mathrm{s})$	1.0×10^{-2}	-
λ_{p}	Coefficient related to cell reorganization time	$1/(\mathrm{Pa} \cdot \mathrm{s})$	1.389×10^{-8}	-

hyperelastic behavior with a strain energy density of the Saint Venant-Kirchhoff type.

The remaining parameter values are taken equal to those in Table 4.2 and Table 4.3.

4.4.2 Results

4.4.2.1 Growth of a tumor spheroid in vitro

In this section we report the results for a tumor spheroid growing suspended in the culture medium. The radius of the spheroid as a function of time is plotted in Figure 4.9.a. Here, the solid line is the result of a numerical simulation where we employed

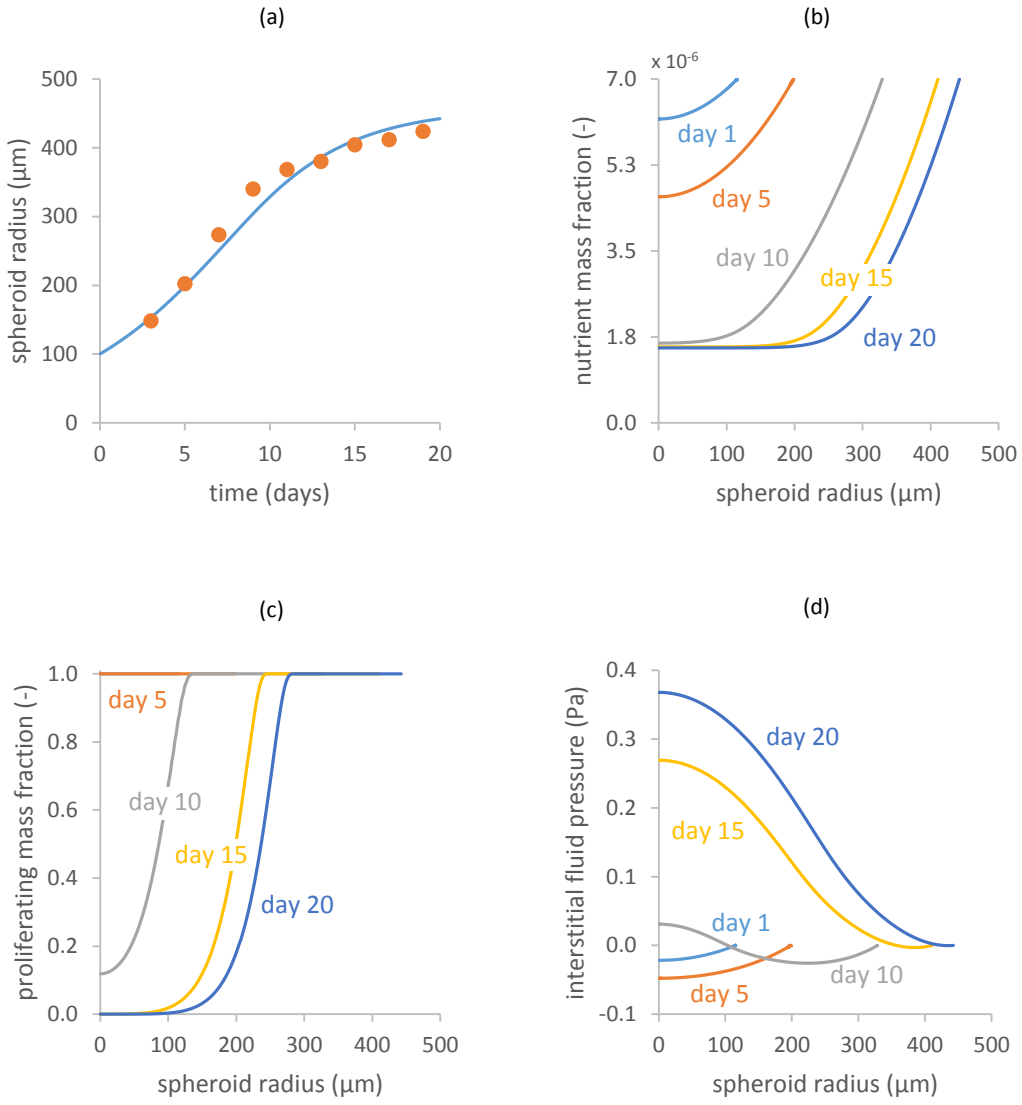

Figure 4.9: Model results for a tumor spheroid (I).

the parameters in Table 4.2, whereas the dotted markers are experimental data taken

from [120]. There is a good agreement with the experimental data, for each of the growth stages of the spheroid. In Figures 4.9b-4.9d, we report the evolution of a quantity over the radius of the spheroid for different times during the simulation. In particular, Figure 4.9.b refers to the mass fraction of oxygen inside the spheroid. Note, at later times, the formation of a nutrient gradient from the spheroid boundary towards its interior. The mass fraction of proliferating tumor cells is shown in Figure 4.9.c. As the spheroid grows, cell death by necrosis appears at the tumor center, evidenced by zero value of the mass fraction. After 20 days from the beginning of the simulation, a necrotic core is clearly visible. Figure 4.9.d shows the evolution of the interstitial fluid pressure inside the spheroid. During the first days the tumor increases its radius and, to satisfy the closure relation in (4.10), the interstitial fluid flows towards the center of the spheroid. As a consequence, the interstitial fluid pressure decreases within the spheroid center. At later times the interstitial fluid pressure rises inside the tumor, following cell death by lysis. Figure 4.10 shows a second set of results. In Figure 4.10.a, the growth stretch ratio g is plotted at different times. This quantity represents the spherical growth term in the multiplicative decomposition of the deformation gradient. As the tumor mass grows, g increases over the spheroid radius, assuming larger values at the spheroid boundary (where the nutrient level is higher). Note that, after a few days, the value of g decreases within the spheroid center. This is due to a reduction of tumor volume by cell death, and is included in the lysis term of Γ^{s} in equation (4.7). The evolution of the trace of $\boldsymbol{B}_{\mathrm{p}}$ is reported in Figure 4.10.b. This quantity measures the plastic distortions occurring in the tumor, which in our framework translate into cell rearrangement. We note that cell rearrangement occurs over the whole spheroid domain, with a peak in the spheroid interior that will be clarified in Figure 4.11. Then, Figure 4.10.c shows the variation of the trace of Cauchy stress inside the tumor. As the tumor grows, the portion at the boundary experiences compressive stresses, since $\mathrm{tr}(\boldsymbol{\sigma}^{\mathrm{s}}_{\mathrm{eff}})$ is negative. The situation changes at the tumor interior, where the tissue is subjected to traction and $\mathrm{tr}(\boldsymbol{\sigma}^{\mathrm{s}}_{\mathrm{eff}})$ is positive. Finally, Figure 4.10.d shows the effective stress of von Mises in the domain. As shown in equation (4.68), we used this measure of stress to mark the onset of plastic flow. From the graph it is possible to observe that the von Mises stress is constant for the most part of the simulation, maintaining the threshold level imposed by the yield stress. However, after 10 days from the beginning of the simulation, the stress exhibits a peak that is gradually relaxed at later times. This stress peak occurs at the same time as the formation of a necrotic population inside the spheroid, as displayed in Figure 4.11. Here, the mass fraction of proliferating cells and the von Mises stress

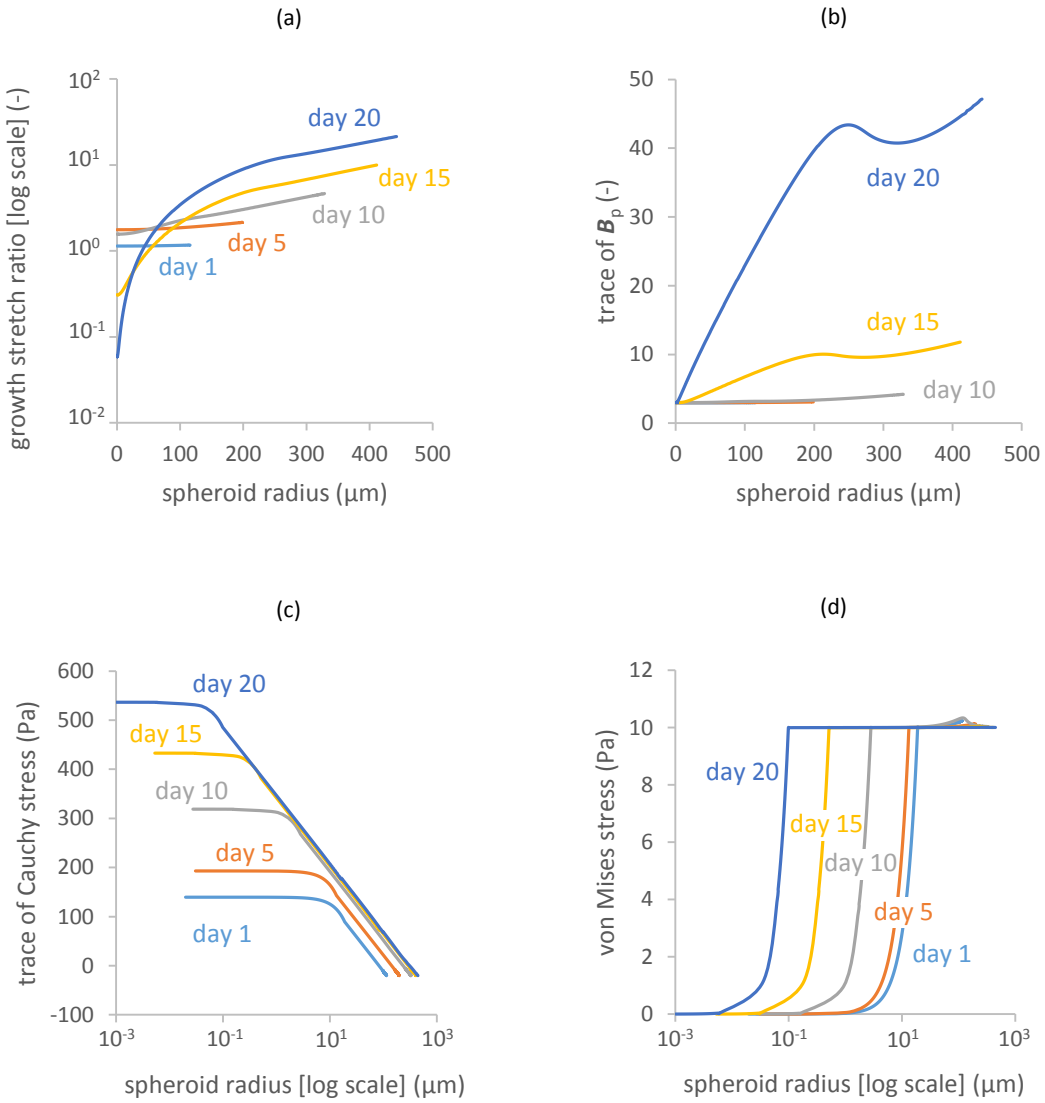

Figure 4.10: Model results for a tumor spheroid (II).

are displayed over the radius of the spheroid at day 5 (Figure 4.11.a), 10 (Figure 4.11.b) and 15 (Figure 4.11.c). At day 5, the spheroid is still entirely composed of proliferating cells, and the von Mises stress is relaxing to the yield value. At day 10, however, the oxygen threshold level falls below the critical threshold and a necrotic population is formed at the spheroid core. Interestingly, the peak in von Mises stress is at the same radial position of the transition between proliferating and necrotic cells. The last snapshot, at day 15, shows an almost completely relaxed state of stress, even if the transition between proliferating and necrotic cells is still present. A possible

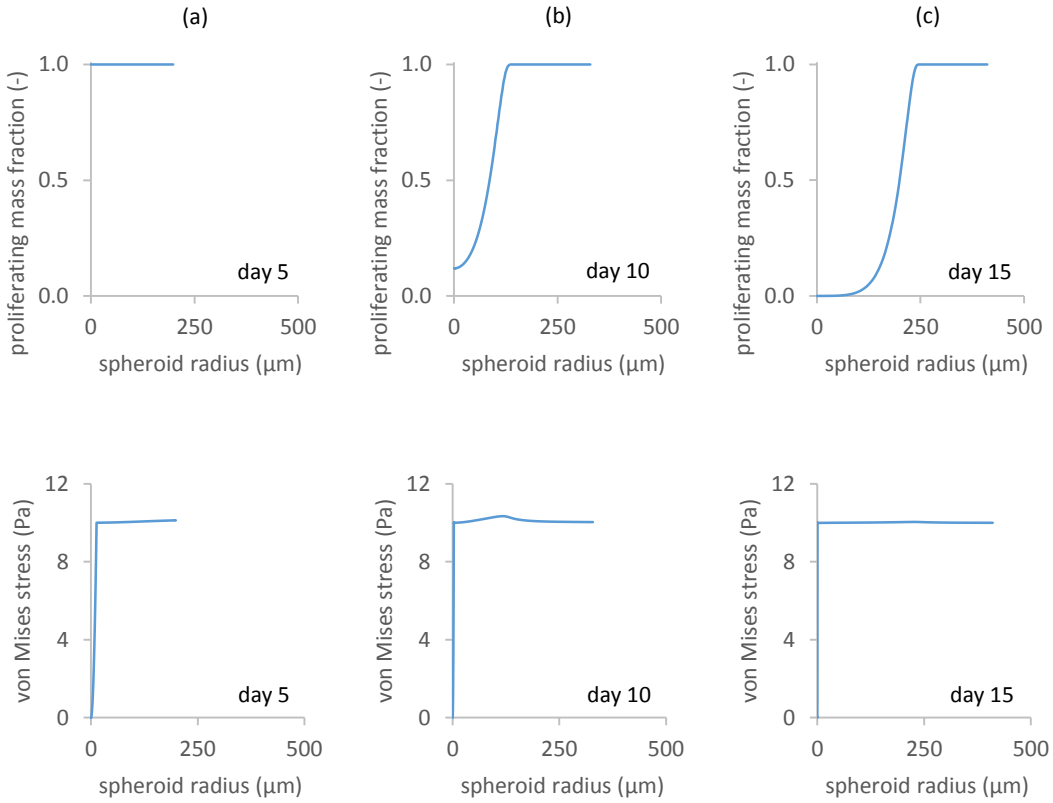

Figure 4.11: Proliferating cell mass fraction and von Mises stress in the tumor spheroid at different times.

explanation of this phenomenon could reside in the growth term of equation (4.63). Indeed, the growth stretch ratio decreases in the necrotic region, whereas it increases for the portion of the spheroid where the cells are proliferating. According to the picture portrayed by the multiplicative decomposition of the deformation gradient, the elastic deformations evolve to accommodate the growth-induced stresses and result in the peak occurring in the von Mises stress. This peak is later relaxed by cell rearrangement, showing the local increase in $\boldsymbol{B}_{\mathrm{p}}$ mentioned in Figure 4.10.b. This result seems interesting, since models based on the multiplicative decomposition of the deformation gradient account in general for only one growing species. Further investigations are required to analyze this mechanical response and the possible links to the underlying biology.

4.4.2.2 Growth of a tumor in a healthy tissue

To begin our analysis, we first test the model for the case in which plastic rearrangement is turned off in the soft host tissue. These results are shown in Figure 4.12. In

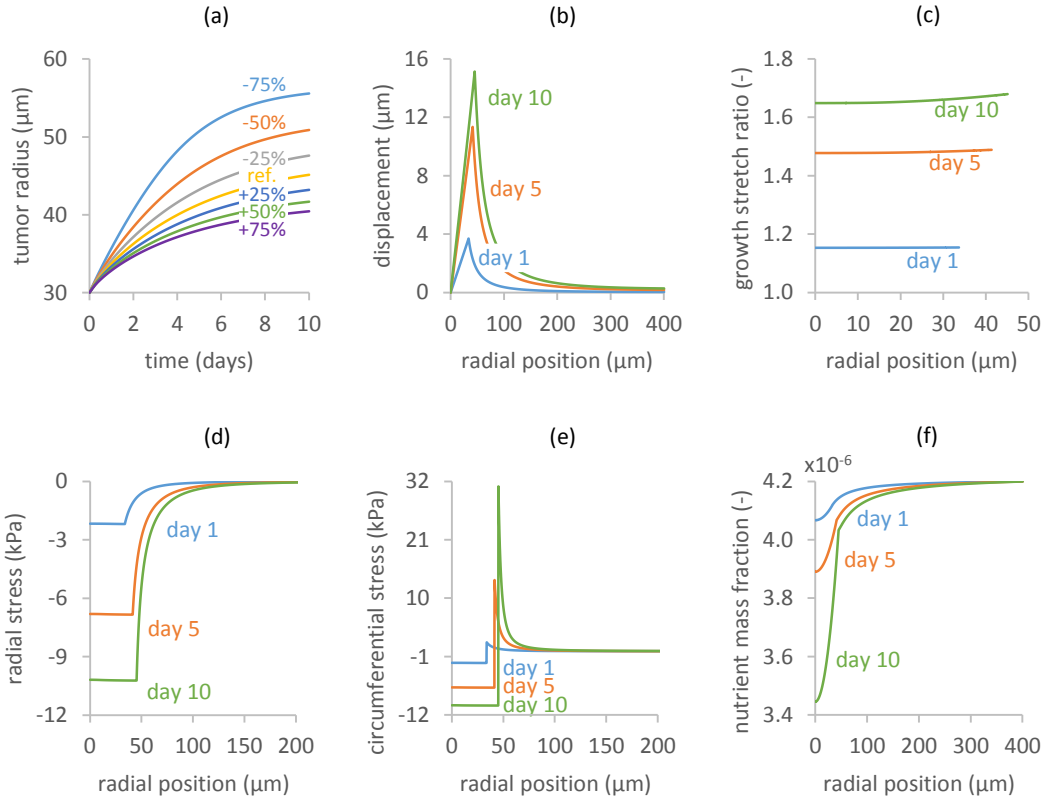

Figure 4.12: Results for a tumor growing in a host tissue (I).

particular, Figure 4.12.a represents the evolution of the tumor radius when the tumor is embedded into host tissues of different stiffness. The line marked with "ref." refers to the reference case of a soft host tissue with the mechanical parameters of Table 4.3. The other lines represent a variation of the parameters μ^{h} and λ^{h} of the -75, -50, -25, +25, +50 and +75% with respect to the reference value. As the stiffness of the healthy tissue increases, the final radius of the tumor is reduced. This behavior is similar to the experimental observations of Helmlinger and coworkers [83], where tumor spheroids are grown in gels of different compliances. The other panels of Figure 4.12 show the evolution of other quantities over the radius of the domain at different times during the simulation. The parameters of Table 4.3 were used for the healthy tissue, considering the case of no remodeling in the latter. The radial component of the displacement is shown in Figure 4.12.b. The point of maximum displacement is at the tumor-host boundary, with a value increasing with time. In accordance to this, the growth stretch ratio (displayed in Figure 4.12.c) is greater towards the tumor boundary, where a higher concentration of nutrient is available for growth. Then, Figures 4.12.d and 4.12.e report the variations in the radial and

circumferential stresses, respectively. Note that the two stress components are both compressive and almost uniform in the tumor interior, while at the interface with the healthy tissue radial stress diminishes and circumferential stress turns to tensile. This result agrees with previous mathematical models investigating the evolution of stress during tumor growth [159, 161, 186]. From the plots it is possible to observe that, even if the yield stress in the tumor is of 10 Pa, the absolute magnitudes of radial and compressive stresses are around a few kPa. This is due to the type of mechanical loading applied on the tumor, which is mainly hydrostatic. Since the flow rule depends on the deviatoric components of the stress, only small plastic deformations are detectable within the tumor domain. Note that the compressive stress applied on the tumor boundary influences also the evolution of the growth stretch ratio in the tumor. In fact, J_e decreases within the tumor as the tissue is compressed. From equation (4.62), the solid volume fraction in the tumor increases and the porosity decreases accordingly. Since the growth stretch ratio depends on Γ^s and this latter term is linear with respect to porosity (see equation (4.58)), this results in a reduction of tumor growth. Finally, the evolution of the oxygen mass fraction is shown in Figure 4.12.f. As the tumor grows, oxygen gradients develop from the periphery to the tumor center. At later times, not reached by the simulation, the oxygen level is expected to fall under the critical threshold, giving rise to a necrotic cell population. The effect of plastic remodeling in the soft host tissue is analyzed in Figure 4.13. Dashed lines

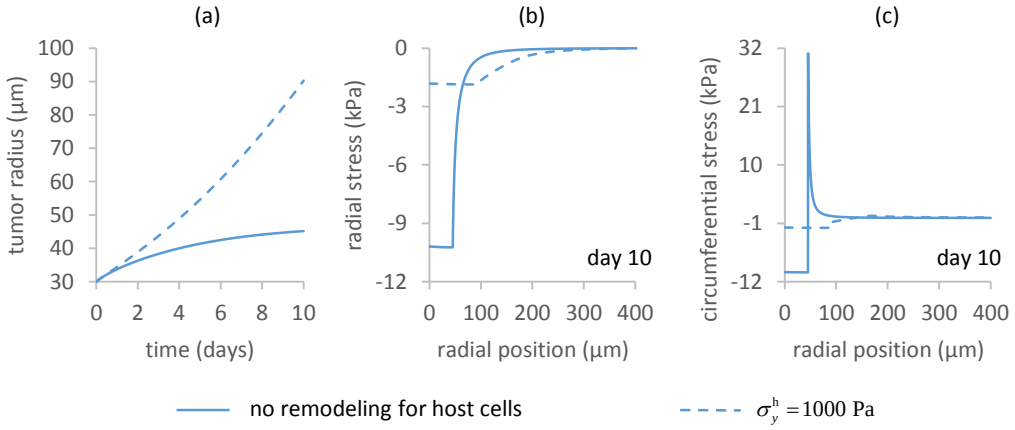

Figure 4.13: Results for a tumor growing in a host tissue (II).

represent the case where plastic deformation is enabled in the healthy tissue, whereas solid lines refer to the reference case of Figure 4.12, where remodeling is neglected. For this analysis, we fixed the yield stress in the soft host tissue to be equal to 10^3 Pa

and used for the parameters the values in Table 4.3. The effects of plastic remodeling on the evolution of the tumor radius are shown in Figure 4.13.a. When compared to the reference case, the tumor grows faster and to a larger extent, reaching a final radius of about 90 μm. This behavior may be explained by considering the effect of stress relaxation induced by plasticity. Indeed, the magnitude of the stresses in the soft host tissue is significantly reduced when compared to the reference case. This is shown in Figure 4.13.b and Figure 4.13.c, where the radial and circumferential stresses are plotted over the radius of the domain at the last time-step of the simulation. The steep transitions in the stress between the tumor and soft host tissue are considerably smoothed out and the absolute value of the stress is greatly reduced. Lower mechanical stresses on the tumor boundary constitute a weaker mechanical barrier that may be less able to constrain tumor growth, leading to larger tumor sizes and host tissue displacements. In addition, as mechanical stress influences cell proliferation through the term in equation (4.58), smaller compressive stresses provide a minor degree of growth inhibition.

4.4.2.3 Tumor growth in the presence of different host tissues

In this section, we investigate the growth of an avascular tumor in a heterogeneous environment. Figure 4.14.a shows the total displacements at day 7 from the beginning of the simulation. As the mechanical environment around the tumor is not the same everywhere, the growth of the latter results to be asymmetric. Due to its larger stiffness, the presence of the bone tissue limits the growth of the tumor mass along one direction. Figure 4.14.b displays the value of the growth stretch ratio over the tumor domain at day 7. Note that the higher values are obtained along the tumor side closer to the capillary surfaces, where there is the maximum value for the nutrient mass fraction. In addition, lower values are displayed over the tumor side that is close to the bone tissue, consistently with Figure 4.14.a. The nutrient mass fraction at day 7 is shown if Figure 4.14.c. The lowest values are attained at the tumor center, where nutrient consumption is more pronounced. Finally, Figure 4.14.d shows the trace of $\boldsymbol{B}_{\mathrm{p}}$ at day 7 over the tissue external to the tumor. The area close to the tumor boundary is subjected to the higher plastic remodeling. As the tumor expands, the healthy tissue is displaced from its original position and the host cells need to rearrange their relative bonds to accommodate the new configuration. The asymmetric tumor growth pattern is highlighted in Figure 4.15, where we display the lateral displacement of the tumor points shown in the inset. The two curves gradually diverge, showing a different evolution over time of the growth rate for the points.

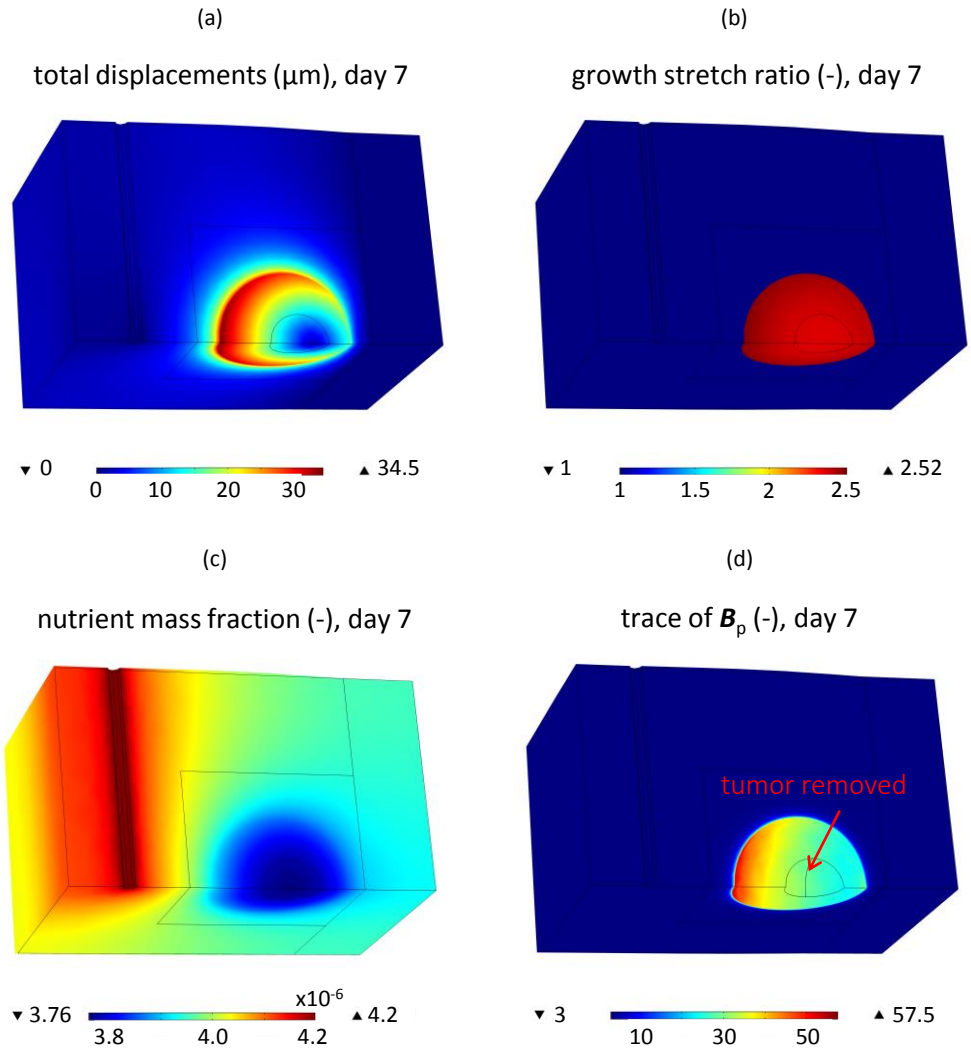

Figure 4.14: Results for a tumor growing in a heterogeneous environment.

4.5 Conclusions

In the present Chapter, a mathematical model for avascular tumor growth is presented. The modeling framework is based on porous media mechanics and the concept of evolving natural configurations, extending previous works in the literature. We start by considering a test case for tissue compression, examining the effect of plastic remodeling on the specimen mechanical response. Then, we consider the case of a growing tumor spheroid, where proliferating tumor cells undergo necrosis if subjected to low levels of nutrient. We analyze the evolution of different quantities, such as the growth stretch ratio, oxygen mass fraction and mechanical stresses, over the spheroid radius for different times. After that, we evaluate the effect of stress relax-

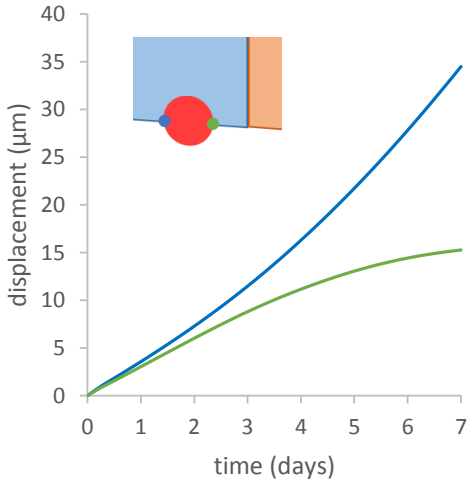

Figure 4.15: Growth curve of two different points in the tumor.

ation induced by cell reorganization in the spheroid. Interestingly, when proliferating cells become necrotic, we observe a peak in the von Mises equivalent stress, followed by a progressive relaxation induced by the plastic contribution to the deformation gradient. Then, we study the growth of a spherical tumor embedded in a healthy tissue. We consider the effects of different mechanical properties of the latter on the tumor. In particular, we vary the external tissue stiffness and we consider both the case of no remodeling and evolving plastic distortions in the host tissue. We analyze the effect of these features on the tumor radius and on the radial and circumferential stresses inside the domain. We observe the influence of plastic reorganization on the host tissue, and we note that the tumor grows larger in a host tissue where remodeling is enabled. Finally, we consider the case of a tumor grown in a host tissue made of two distinct compartments, i.e. a healthy soft tissue and a bone. The different mechanical properties of the two tissues affect significantly the growth of the tumor mass, which, starting from a spherical form, assumes an asymmetric shape at the end of the simulation. Since one of the two domains is stiffer than the other, and since the cancer cells proliferate more towards the region of least mechanical resistance, the tumor extends more in the softer host tissue.

Several simplifying assumptions are considered in the study, and the work is certainly open to further improvements. The modeling framework is simplified with respect to the more general model of [166], where tumor cells and host cells are treated as fluids. In fact, the present model does not allow to take into account migration of cells through the ECM [165], possible detachment of the cells from the

ECM and from other cell populations, different stiffness of the cell population with respect to the ECM with which they are here lumped, build-up of cortical tension between healthy and tumor tissues, and possible invasion of the tumor tissue by the healthy tissue or vice versa, mediated by these cortical tensions. It allows, however, for displacement of the host tissue by the tumor and also investigation of possible fingering.

For the future, we are planning to develop the model proposed here by taking into account different phenomena. In particular, the adhesion mechanisms between the cells and the ECM should be investigated in more detail. This will probably lead to a modification of the plastic flow rule, including the effect of different adhesion molecules, such as catherins and integrins. Moreover, cells belonging to different cellular populations should display distinct adhesive characteristics, contributing to a modified form of the yield stress. Model development requires experiments that are able to provide better estimates for the model parameters. Furthermore, new sets of data in terms of quantities that can be compared to the output of the model equations are needed. Part of the future experimental work should also be devoted to supply measures of the yield stress, with experiments like those in [88, 56, 119]. To this regard, it would be extremely interesting to investigate the mechanical response of spheroids subjected to both compressive and shear stresses, also interfering with the adhesion molecules by using different drugs. Describing more thoroughly the interactions between the tumor and its external (biochemical and mechanical) microenvironment should offer valuable insights into the understanding of the disease progression, with the final aim of helping the design of new therapeutic treatments.

Conclusions

In this work we presented different frameworks to deal with mathematical modeling of growing tumors. Our discussion focused on two main topics, namely the development of a mathematical model to describe tumor spheroid experiments, and a theoretical framework that is able to account for cellular adhesion mechanisms in tissue mechanics. In both cases, we extended results in the existing literature on the corresponding topics, including phenomena that lead to new equations.

Starting with the model for tumor spheroids, we validated our set of equations with experimental data from spheroids growing freely in the culture medium and then subjected to a mechanical compressive load. Then, we proposed a new constitutive relation for growth inhibition due to mechanical stress that describes the growth curves better than the existing expressions in literature. After that, we analyzed the model through a parametric study. Our results confirmed that model parameters related to growth and death processes significantly influence the final radius reached by the tumor. Finally, we introduced equations describing the transport and consumption of a chemotherapeutic agent in the spheroids. We found a good qualitative agreement between model results and experiments reported in literature, in terms of spheroid volume reduction and limited drug diffusion inside the tumor. Interestingly, our results suggest that the efficacy of drugs targeting cell proliferation may decrease for spheroids subjected to mechanical compression.

In the second part of the discussion, we implemented a constitutive law for the mechanical response of soft tissues and tested different cases. As a first example, we studied the unconfined compression of a tissue specimen, and we evaluated the effects of plastic remodeling on the tissue mechanical response. Then, we showed results for three cases of biological interest, namely the growth of a spherical tumor in culture medium, in a host tissue, and in a three-dimensional physiological configuration characterized by a heterogeneous environment. We analyzed the dependence of tumor development on the mechanical properties of the neighboring tissues, with particular focus on cell reorganization and its role in stress relaxation.

For the future, we plan to include more nutrients and growth factors in our modeling framework. This should allow to take into account important interactions between the tumor components and their chemo-mechanical surroundings. Also, there is a urgent need for experimental works that investigate the cellular bases underlying the compression experiments. Experiments are also needed to clarify the role of the external environment on the performance of therapeutic agents in tumors. We would like to give our contribution on these issues, in a manner similar to the work that we did with tumor spheroids. Another possible development is the inclusion in the constitutive relation of different adhesion mechanisms between cells and ECM. This will lead to the derivation of a new plastic flow rule, that will improve our description of the tumor system. Also for this second case, we are currently looking for collaborators to design experiments that will address the mechanical response of cell aggregates and its impact on tumor evolution.

We believe that this is a promising time for biomechanics and, in particular, for cancer physics. Current tumor models include important biological features of cancer progression, and emerging modeling techniques are showing encouraging results for clinical applications. It is becoming increasingly clear that cancer systems are too complex to be investigated just on biological grounds, and this should promote the dialog between mathematical and biomedical communities. Integration of approaches from physical sciences and cancer biology may lead to new discoveries in tumor development, with the final aim of suggesting effective strategies for cancer treatment.

Appendix A

Derivation of the model equations

We derive the material form of the equations (4.63)-(4.66).

Starting from (4.4), for the mass balance equation of the solid phase we write:

$$\mathcal{D}^{\mathrm{s}}\left(\varepsilon^{\mathrm{s}}\rho^{\mathrm{s}}\right)+\varepsilon^{\mathrm{s}}\rho^{\mathrm{s}}\mathrm{div}\left(\boldsymbol{v}^{\mathrm{s}}\right)=\Gamma^{\mathrm{s}}, \tag{A.1}$$

where $\mathcal{D}^{\mathrm{s}}\left(\cdot\right)=\partial_t\left(\cdot\right)+\boldsymbol{v}^{\mathrm{s}}\cdot\mathrm{grad}\left(\cdot\right)$ denotes the material derivative of the argument. From the identity $\dot{J}=J\mathrm{div}\left(\boldsymbol{v}^{\mathrm{s}}\right)$ we can write in the reference frame:

$$\dot{\overline{\varepsilon^{\mathrm{s}}\rho^{\mathrm{s}}}}+\varepsilon^{\mathrm{s}}\rho^{\mathrm{s}}\frac{\dot{J}}{J}=\Gamma^{\mathrm{s}}, \tag{A.2}$$

$$\dot{\overline{J\varepsilon^{\mathrm{s}}\rho^{\mathrm{s}}}}=\dot{\overline{J_{\mathrm{e}}\varepsilon^{\mathrm{s}}\rho^{\mathrm{s}}}}J_{\mathrm{g}}+J_{\mathrm{e}}\varepsilon^{\mathrm{s}}\rho^{\mathrm{s}}\dot{J}_g=\dot{\overline{J_{\mathrm{e}}\varepsilon^{\mathrm{s}}\rho^{\mathrm{s}}}}J_{\mathrm{g}}+3J\varepsilon^{\mathrm{s}}\rho^{\mathrm{s}}\frac{\dot{g}}{g}=J\Gamma^{\mathrm{s}}, \tag{A.3}$$

with $\dot{J}_{\mathrm{g}}=J_{\mathrm{g}}\mathrm{tr}\left(\dot{\boldsymbol{F}}_{\mathrm{g}}\boldsymbol{F}_{\mathrm{g}}^{-1}\right)=3J_{\mathrm{g}}\,\dot{g}/g$. If we impose that the rate of change of mass contributes entirely to the growth term, then we have:

$$\varepsilon^{\mathrm{s}}\rho^{\mathrm{s}}J_{\mathrm{e}}=\rho_0^{\mathrm{s}}=\mathrm{const.} \tag{A.4}$$

and equation (A.3) gives:

$$\frac{\dot{g}}{g}=\frac{1}{3}\frac{\Gamma^{\mathrm{s}}}{\varepsilon^{\mathrm{s}}\rho^{\mathrm{s}}}, \tag{A.5}$$

whereas equation (A.4) gives an expression for ε^{s}:

$$\varepsilon^{\mathrm{s}}=\frac{\rho_0^{\mathrm{s}}}{\rho^{\mathrm{s}}J_{\mathrm{e}}}=\frac{g^3\rho_0^{\mathrm{s}}}{\rho^{\mathrm{s}}J}, \tag{A.6}$$

and we also have that:

$$\varepsilon_{\nu}^{\mathrm{s}}=\varepsilon^{\mathrm{s}}J_{\mathrm{e}}=\frac{\rho_0^{\mathrm{s}}}{\rho^{\mathrm{s}}}. \tag{A.7}$$

Note that, in general, ρ^{s} can depend on the mass fraction of the constituents, i.e. $\rho^{\mathrm{s}}=\rho^{\mathrm{s}}\left(\omega^{\mathrm{p}},\omega^{\mathrm{n}}\right)$.

The mass balance equation for the proliferating cells reads

$$\mathcal{D}^{\mathrm{s}}\left(\varepsilon^{\mathrm{s}}\rho^{\mathrm{s}}\omega^{\mathrm{p}}\right)+\varepsilon^{\mathrm{s}}\rho^{\mathrm{s}}\omega^{\mathrm{p}}\mathrm{div}\left(\boldsymbol{v}^{\mathrm{s}}\right)=\Gamma_{\mathrm{p}}^{\mathrm{p}\to\mathrm{n}}+\Gamma_{\mathrm{p}}^{\mathrm{f}\to\mathrm{p}}, \tag{A.8}$$

$$\dot{\overline{\varepsilon^{\mathrm{s}}\rho^{\mathrm{s}}\omega^{\mathrm{p}}J}}=J\Gamma^{\mathrm{s}}\omega^{\mathrm{p}}+J\varepsilon^{\mathrm{s}}\rho^{\mathrm{s}}\dot{\omega}^{\mathrm{p}}=J\left(\Gamma_{\mathrm{p}}^{\mathrm{p}\to\mathrm{n}}+\Gamma_{\mathrm{p}}^{\mathrm{f}\to\mathrm{p}}\right), \tag{A.9}$$

$$\dot{\omega}^{\mathrm{p}}=\frac{J}{\rho_0^{\mathrm{s}}g^3}\left(\Gamma_{\mathrm{p}}^{\mathrm{p}\to\mathrm{n}}+\Gamma_{\mathrm{p}}^{\mathrm{f}\to\mathrm{p}}-\omega^{\mathrm{p}}\Gamma^{\mathrm{s}}\right)=\frac{1}{\varepsilon^{\mathrm{s}}\rho^{\mathrm{s}}}\left(\Gamma_{\mathrm{p}}^{\mathrm{p}\to\mathrm{n}}+\Gamma_{\mathrm{p}}^{\mathrm{f}\to\mathrm{p}}-\omega^{\mathrm{p}}\Gamma^{\mathrm{s}}\right), \tag{A.10}$$

in which equations (A.4) and (A.5) are used. Similarly, for the necrotic portion of the cells we can write:

$$\dot{\omega}^{\mathrm{n}}=\frac{J}{\rho_0^{\mathrm{s}}g^3}\left(\Gamma_{\mathrm{n}}^{\mathrm{n}\to\mathrm{f}}+\Gamma_{\mathrm{n}}^{\mathrm{p}\to\mathrm{n}}-\omega^{\mathrm{n}}\Gamma^{\mathrm{s}}\right). \tag{A.11}$$

The mass balance equation for the whole solid-fluid system is obtained by summing up the two mass balance equations for the solid and the fluid phase, which read

$$\partial_t\varepsilon^{\mathrm{s}}+\mathrm{div}\left(\varepsilon^{\mathrm{s}}\boldsymbol{v}^{\mathrm{s}}\right)+\frac{\varepsilon^{\mathrm{s}}}{\rho^{\mathrm{s}}}\mathcal{D}^{\mathrm{s}}\rho^{\mathrm{s}}=\frac{\Gamma^{\mathrm{s}}}{\rho^{\mathrm{s}}}, \tag{A.12}$$

$$\partial_t\varepsilon^{\mathrm{f}}+\mathrm{div}\left(\varepsilon^{\mathrm{f}}\boldsymbol{v}^{\mathrm{f}}\right)+\frac{\varepsilon^{\mathrm{f}}}{\rho^{\mathrm{f}}}\mathcal{D}^{\mathrm{f}}\rho^{\mathrm{f}}=-\frac{\Gamma^{\mathrm{s}}}{\rho^{\mathrm{f}}}, \tag{A.13}$$

respectively. Summing equation (A.12) and (A.13) gives:

$$\mathrm{div}\left(\boldsymbol{q}\right)+\mathrm{div}\left(\boldsymbol{v}^{\mathrm{s}}\right)+\varepsilon^{\mathrm{f}}\beta^{\mathrm{f}}+\varepsilon^{\mathrm{s}}\beta^{\mathrm{s}}=\left(\frac{1}{\rho^{\mathrm{s}}}-\frac{1}{\rho^{\mathrm{f}}}\right)\Gamma^{\mathrm{s}}, \tag{A.14}$$

in which $\beta^{\mathrm{j}}=\mathcal{D}^{\mathrm{j}}\rho^{\mathrm{j}}/\rho^{\mathrm{j}},\ \mathrm{j}=\mathrm{f},\mathrm{s}$ represent the compressibility of the j-th phase, and $\boldsymbol{q}=\varepsilon^{\mathrm{f}}\left(\boldsymbol{v}^{\mathrm{f}}-\boldsymbol{v}^{\mathrm{s}}\right)$. Note that

$$\varepsilon^{\mathrm{f}}\beta^{\mathrm{f}}=\frac{\varepsilon^{\mathrm{f}}}{\rho^{\mathrm{f}}}\left[\mathcal{D}^{\mathrm{s}}\rho^{\mathrm{f}}+\left(\boldsymbol{v}^{\mathrm{f}}-\boldsymbol{v}^{\mathrm{s}}\right)\cdot\mathrm{grad}\,\rho^{\mathrm{f}}\right]=\varepsilon^{\mathrm{f}}\frac{\mathcal{D}^{\mathrm{s}}\rho^{\mathrm{f}}}{\rho^{\mathrm{f}}}+\frac{\mathrm{grad}\,\rho^{\mathrm{f}}\cdot\boldsymbol{q}}{\rho^{\mathrm{f}}}. \tag{A.15}$$

By employing (A.15) and applying a Piola Transformation of equation (A.14) we obtain

$$\begin{aligned}\mathrm{Div}\left(\boldsymbol{Q}\right)+\dot{J}+J\left(1-\varepsilon^{\mathrm{s}}\right)\frac{\dot{\rho}^{\mathrm{f}}}{\rho^{\mathrm{f}}}+\frac{1}{\rho^{\mathrm{f}}}\boldsymbol{Q}\cdot\mathrm{Grad}\,\rho^{\mathrm{f}}+J\varepsilon^{\mathrm{s}}\frac{\dot{\rho}^{\mathrm{s}}}{\rho^{\mathrm{s}}}&\\ =J\left(\frac{1}{\rho^{\mathrm{s}}}-\frac{1}{\rho^{\mathrm{f}}}\right)\Gamma^{\mathrm{s}},&\end{aligned} \tag{A.16}$$

where we defined $\boldsymbol{Q}=J\boldsymbol{F}^{-1}\boldsymbol{q}$. Note that if the densities of the phases are assumed to be constant and equal to each other the expression above can be simplified into:

$$\mathrm{Div}\left(\boldsymbol{Q}\right)+\dot{J}=0, \tag{A.17}$$

with $\boldsymbol{Q}$ given constitutively as:

$$\boldsymbol{Q} = -J\boldsymbol{F}^{-1}\boldsymbol{k}\boldsymbol{F}^{-T}\mathrm{Grad}\ p^{\mathrm{f}}. \tag{A.18}$$

Here $\boldsymbol{k}$ is the hydraulic conductivity tensor of the solid.

For the nutrient species we rewrite the mass balance equation as:

$$\mathcal{D}^{\mathrm{s}}\left(\varepsilon^{\mathrm{f}}\rho^{\mathrm{f}}\omega^{\mathrm{N}}\right) + \varepsilon^{\mathrm{f}}\rho^{\mathrm{f}}\omega^{\mathrm{N}}\mathrm{div}\left(\boldsymbol{v}^{\mathrm{s}}\right) + \mathrm{div}\left[\varepsilon^{\mathrm{f}}\rho^{\mathrm{f}}\omega^{\mathrm{N}}\left(\boldsymbol{v}^{\mathrm{f}} - \boldsymbol{v}^{\mathrm{s}}\right) + \boldsymbol{J}^{\mathrm{N}}\right] = \Gamma_{\mathrm{N}}^{\mathrm{N}\to\mathrm{p}}, \tag{A.19}$$

where $\boldsymbol{J}^{\mathrm{N}} = -\varepsilon^{\mathrm{f}}\rho^{\mathrm{f}}\boldsymbol{D}^{\mathrm{N}}\mathrm{grad}\,\omega^{\mathrm{N}}$. The term $\boldsymbol{D}^{\mathrm{N}}$ is the diffusivity tensor of the nutrient dissolved into the interstitial fluid. This equation can be rewritten in the material frame as:

$$\dot{\overline{J\varepsilon^{\mathrm{f}}\rho^{\mathrm{f}}\omega^{\mathrm{N}}}} + \mathrm{Div}\left(\rho^{\mathrm{f}}\omega^{\mathrm{N}}\boldsymbol{Q} + \boldsymbol{\Psi}^{\mathrm{N}}\right) = J\Gamma_{\mathrm{N}}^{\mathrm{N}\to\mathrm{p}}, \tag{A.20}$$

where the material diffusive flux is written as $\boldsymbol{\Psi}^{\mathrm{N}} = -J\varepsilon^{\mathrm{f}}\rho^{\mathrm{f}}\boldsymbol{F}^{-1}\boldsymbol{D}^{\mathrm{N}}\boldsymbol{F}^{-T}\mathrm{Grad}\,\omega^{\mathrm{N}}$. By manipulating this equation, and knowing that

$$\mathcal{D}^{\mathrm{f}}\left(\varepsilon^{\mathrm{f}}\rho^{\mathrm{f}}\right) + \varepsilon^{\mathrm{f}}\rho^{\mathrm{f}}\mathrm{div}\left(\boldsymbol{v}^{\mathrm{f}}\right) = \Gamma^{\mathrm{f}}, \tag{A.21}$$

$$\mathcal{D}^{\mathrm{s}}\left(\varepsilon^{\mathrm{f}}\rho^{\mathrm{f}}\right) + \mathrm{div}\left(\rho^{\mathrm{f}}\varepsilon^{\mathrm{f}}\boldsymbol{q}\right) + \varepsilon^{\mathrm{f}}\rho^{\mathrm{f}}\mathrm{div}\left(\boldsymbol{v}^{\mathrm{s}}\right) = -\Gamma^{\mathrm{s}}, \tag{A.22}$$

$$\dot{\overline{J\varepsilon^{\mathrm{f}}\rho^{\mathrm{f}}}} + \mathrm{Div}\left(\rho^{\mathrm{f}}\boldsymbol{Q}\right) = -J\Gamma^{\mathrm{s}}, \tag{A.23}$$

we arrive at the final form of the nutrient mass balance equation, which reads

$$J\varepsilon^{\mathrm{f}}\rho^{\mathrm{f}}\dot{\omega}^{\mathrm{N}} + \rho^{\mathrm{f}}\boldsymbol{Q}\cdot\mathrm{Grad}\,\omega^{\mathrm{N}} + \mathrm{Div}\left(\boldsymbol{\Psi}^{\mathrm{N}}\right) = J\left(\Gamma_{\mathrm{N}}^{\mathrm{N}\to\mathrm{p}} + \omega^{\mathrm{N}}\Gamma^{\mathrm{s}}\right). \tag{A.24}$$

Bibliography

[1] M. Abercrombie and E. J. Ambrose. The surface properties of cancer cells: a review. *Cancer Research*, 22:525–48, 1962.

[2] B. Alberts, A. Johnson, J. Lewis, D. Morgan, M. Raff, K. Roberts, and P. Walter. *Molecular Biology of the Cell, Sixth Edition.* Taylor & Francis Group, 2014.

[3] P. M. Altrock, L. L. Liu, and F. Michor. The mathematics of cancer: integrating quantitative models. *Nature Reviews Cancer*, 15(12):730–745, 2015.

[4] D. Ambrosi and F. Mollica. On the mechanics of a growing tumor. *International Journal of Engineering Science*, 40(12):1297–1316, 2002.

[5] D. Ambrosi and F. Mollica. The role of stress in the growth of a multicell spheroid. *Journal of Mathematical Biology*, 48(5):477–499, 2004.

[6] D. Ambrosi and L. Preziosi. Cell adhesion mechanisms and stress relaxation in the mechanics of tumours. *Biomechanics and Modeling in Mechanobiology*, 8(5):397–413, 2009.

[7] D. Ambrosi, L. Preziosi, and G. Vitale. The interplay between stress and growth in solid tumors. *Mechanics Research Communications*, 42:87–91, 2012.

[8] S. Angeli and T. Stylianopoulos. Biphasic modeling of brain tumor biomechanics and response to radiation treatment. *Journal of Biomechanics*, 2016.

[9] A. Araujo, L. M. Cook, C. C. Lynch, and D. Basanta. An integrated computational model of the bone microenvironment in bone-metastatic prostate cancer. *Cancer Research*, 74(9):2391–2401, 2014.

[10] R. P. Araujo and D. L. S. McElwain. A history of the study of solid tumour growth: the contribution of mathematical modelling. *Bulletin of Mathematical Biology*, 66(5):1039–91, 2004.

[11] P. Armitage and R. Doll. The age distribution of cancer and a multi-stage theory of carcinogenesis. *British Journal of Cancer*, 8(1):1–12, 1954.

[12] D. Balding and D. L. S. McElwain. A mathematical model of tumour-induced capillary growth. *Journal of Theoretical Biology*, 114(1):53 – 73, 1985.

[13] W. Baumgartner, P. Hinterdorfer, W. Ness, A. Raab, D. Vestweber, H. Schindler, and D. Drenckhahn. Cadherin interaction probed by atomic force microscopy. *Proceedings of the National Academy of Sciences*, 97(8):4005–10, 2000.

[14] N. Bellomo, E. de Angelis, and L. Preziosi. Multiscale modeling and mathematical problems related to tumor evolution and medical therapy. *Journal of Theoretical Medicine*, 5(2):111–136, 2003.

[15] A. B. Bilby, L. R. T. Gardner, and A. N. Stroh. Continuous distributions of dislocations and the theory of plasticity. In *Proceedings of the XIth ICTAM*. Presses de l'Université of Bruxelles, 1957.

[16] V. Boekhorst, L. Preziosi, and P. Friedl. Plasticity of cell migration in vivo and in silico. *Annual Review of Cell and Developmental Biology*, 32(1), 2016.

[17] C. Bonnans, C. Jonathan, and W. Zena. Remodelling the extracellular matrix in development and disease. *Nature Reviews. Molecular Cell Biology*, 15(12):786–801, 2014.

[18] C. Bonnet-Gonnet, L. Belloni, and B. Cabane. Osmotic pressure of latex dispersions. *Langmuir*, 10(11):4012–4021, 1994.

[19] Y. Boucher, L. T. Baxter, and R. K. Jain. Interstitial pressure gradients in tissue-isolated and subcutaneous tumors: implications for therapy. *Cancer research*, 50(15):4478–84, aug 1990.

[20] A. Bouchoux, P. Cayemitte, J. Jardin, G. Gésan-Guiziou, and B. Cabane. Casein micelle dispersions under osmotic stress. *Biophysical Journal*, 96(2):693–706, 2009.

[21] C. J. W. Breward, H. M. Byrne, and C. E. Lewis. The role of cell-cell interactions in a two-phase model for avascular tumour growth. *Journal of Mathematical Biology*, 45(2):125–52, 2002.

[22] D. T. Butcher, T. Alliston, and V. M. Weaver. A tense situation: forcing tumour progression. *Nature Reviews Cancer*, 9(2):108–122, 2009.

[23] H. Byrne and L. Preziosi. Modelling solid tumour growth using the theory of mixtures. *Mathematical Medicine and Biology*, 20(4):341–66, 2003.

[24] H. M. Byrne. Dissecting cancer through mathematics: from the cell to the animal model. *Nature reviews. Cancer*, 10(3):221–30, 2010.

[25] H. M. Byrne and M. A. J. Chaplain. Mathematical models for tumour angiogenesis: numerical simulations and nonlinear wave solutions. *Bulletin of Mathematical Biology*, 57(3):461–486, 1995.

[26] H. M. Byrne, J. R. King, D. L. S. McElwain, and L. Preziosi. A two-phase model of solid tumour growth. *Applied Mathematics Letters*, 16(4):567–573, 2003.

[27] J. Carlsson. A proliferation gradient in three-dimensional colonies of cultured human glioma cells. *International Journal of Cancer*, 20(1):129–36, 1977.

[28] J. Carlsson and J. M. Yuhas. Liquid-overlay culture of cellular spheroids. *Recent Results in Cancer Research*, 95(Foa 4):1–23, 1984.

[29] P. Carmeliet and R. K. Jain. Angiogenesis in cancer and other diseases. *Nature*, 407(6801):249–57, 2000.

[30] J. J. Casciari, S. V. Sotirchos, and R. M. Sutherland. Mathematical modelling of microenvironment and growth in EMT6/Ro multicellular tumour spheroids. *Cell Proliferation*, 25(1):1–22, 1992.

[31] J. J. Casciari, S. V. Sotirchos, and R. M. Sutherland. Variations in tumor cell growth rates and metabolism with oxygen concentration, glucose concentration, and extracellular pH. *Journal of Cellular Physiology*, 151(2):386–94, 1992.

[32] M. A. J. Chaplain, L. Graziano, and L. Preziosi. Mathematical modelling of the loss of tissue compression responsiveness and its role in solid tumour development. *Mathematical Medicine and Biology*, 23(3):197–229, 2006.

[33] M. A. J. Chaplain, S. R. McDougall, and A. R. A. Anderson. Mathematical modeling of tumor-induced angiogenesis. *Annual Review of Biomedical Engineering*, 8:233–57, 2006.

[34] V. P. Chauhan and R. K. Jain. Strategies for advancing cancer nanomedicine. *Nature Materials*, 12(11):958–62, 2013.

[35] G. Cheng, J. Tse, R. K. Jain, and L. L. Munn. Micro-environmental mechanical stress controls tumor spheroid size and morphology by suppressing proliferation and inducing apoptosis in cancer cells. *PloS One*, 4(2):e4632, 2009.

[36] J. Chmielecki et al. Optimization of Dosing for EGFR-Mutant Non-Small Cell Lung Cancer with Evolutionary Cancer Modeling. *Science Translational Medicine*, 3(90):90ra59–90ra59, 2011.

[37] P. Ciarletta, D. Ambrosi, G. A. Maugin, and L. Preziosi. Mechano-transduction in tumour growth modelling. *The European Physical Journal E*, 36(3):23, 2013.

[38] P. Ciarletta, L. Preziosi, and G. A. Maugin. Mechanobiology of interfacial growth. *Journal of the Mechanics and Physics of Solids*, 61(3):852–872, 2013.

[39] M. L. Citron et al. Randomized Trial of Dose-Dense Versus Conventionally Scheduled and Sequential Versus Concurrent Combination Chemotherapy as Postoperative Adjuvant Treatment of Node-Positive Primary Breast Cancer: First Report of Intergroup Trial C9741/Cancer and Leukemia. *Journal of Clinical Oncology*, 21(8):1431–1439, 2003.

[40] A. Coldman and J. Goldie. A stochastic model for the origin and treatment of tumors containing drug-resistant cells. *Bulletin of Mathematical Biology*, 48(3-4):279–292, 1986.

[41] V. Cristini, J. Lowengrub, and Q. Nie. Nonlinear simulation of tumor growth. *Journal of Mathematical Biology*, 46(3):191–224, 2003.

[42] L. T. Curtis, C. G. England, M. Wu, J. Lowengrub, and H. B. Frieboes. An interdisciplinary computational/experimental approach to evaluate drug-loaded gold nanoparticle tumor cytotoxicity. *Nanomedicine*, 11(3):197–216, 2016.

[43] C. M. Dawidczyk, C. Kim, J. H. Park, L. M. Russell, K. H. Lee, M. G. Pomper, and P. C. Searson. State-of-the-art in design rules for drug delivery platforms: lessons learned from FDA-approved nanomedicines. *Journal of Controlled Release*, 187:133–44, 2014.

[44] K. E. de Visser, A. Eichten, and L. M. Coussens. Paradoxical roles of the immune system during cancer development. *Nature Reviews. Cancer*, 6(1):24–37, 2006.

[45] T. S. Deisboeck, L. Zhang, J. Yoon, and J. Costa. In silico cancer modeling: is it ready for prime time? *Nature Clinical Practice. Oncology*, 6(1):34–42, 2009.

[46] M. Delarue, F. Montel, D. Vignjevic, J. Prost, J. Joanny, and G. Cappello. Compressive stress inhibits proliferation in tumor spheroids through a volume limitation. *Biophysical Journal*, 107(8):1821–8, 2014.

[47] A. Desmaison, C. Frongia, K. Grenier, B. Ducommun, and V. Lobjois. Mechanical stress impairs mitosis progression in multi-cellular tumor spheroids. *PloS One*, 8(12):e80447, 2013.

[48] C. Dietrich, K. Wallenfang, F. Oesch, and R. Wieser. Differences in the mechanisms of growth control in contact-inhibited and serum-deprived human fibroblasts. *Oncogene*, 15(22):2743–7, 1997.

[49] M. J. Dorie, R. F. Kallman, D. F. Rapacchietta, D. van Antwerp, and Y. R. Huang. Migration and internalization of cells and polystyrene microspheres in tumor cell spheroids. *Experimental Cell Research*, 141(1):201–209, sep 1982.

[50] J. Dusheck. Oncology: getting physical. *Nature*, 491(7425):S50–S51, 2012.

[51] W. Ehlers, B. Markert, and O. Röhrle. Computational continuum biomechanics with application to swelling media and growth phenomena. *GAMM-Mitteilungen*, 32(2):135–156, 2009.

[52] M. Epstein and G. A. Maugin. Thermomechanics of volumetric growth in uniform bodies. *International Journal of Plasticity*, 16(7):951–978, 2000.

[53] E. Fennema, N. Rivron, J. Rouwkema, C. van Blitterswijk, and J. de Boer. Spheroid culture as a tool for creating 3D complex tissues. *Trends in Biotechnology*, 31(2):108–15, 2013.

[54] Fernández-Sánchez et al. Mechanical induction of the tumorigenic β-catenin pathway by tumour growth pressure. *Nature*, 523(7558):92–95, 2015.

[55] J. Folkman and M. Hochberg. Self-regulation of growth in three dimensions. *The Journal of Experimental Medicine*, 138(4):745–53, 1973.

[56] G. Forgacs, R. A. Foty, Y. Shafrir, and M. S. Steinberg. Viscoelastic properties of living embryonic tissues: a quantitative study. *Biophysical journal*, 74(5):2227–34, 1998.

[57] V. Frank et al. Frequent mechanical stress suppresses proliferation of mesenchymal stem cells from human bone marrow without loss of multipotency. *Scientific Reports*, 6:24264, 2016.

[58] S. J. Franks, H. M. Byrne, H. S. Mudhar, J. C. E. Underwood, and C. E. Lewis. Mathematical modelling of comedo ductal carcinoma in situ of the breast. *Mathematical Medicine and Biology*, 20(3):277–308, 2003.

[59] J. P. Freyer and R. M. Sutherland. Regulation of growth saturation and development of necrosis in EMT6/Ro multicellular spheroids by the glucose and oxygen supply. *Cancer Research*, 46(7):3504–12, 1986.

[60] H. B. Frieboes et al. Prediction of drug response in breast cancer using integrative experimental/computational modeling. *Cancer Research*, 69(10):4484–4492, 2009.

[61] H. B. Frieboes, F. Jin, Y. Chuang, S. M. Wise, J. S. Lowengrub, and V. Cristini. Three-dimensional multispecies nonlinear tumor growthII: Tumor invasion and angiogenesis. *Journal of Theoretical Biology*, 264(4):1254–1278, 2010.

[62] H. B. Frieboes, X. Zheng, C. Sun, B. Tromberg, R. Gatenby, and V. Cristini. An integrated computational/experimental model of tumor invasion. *Cancer Research*, 66(3):1597–604, 2006.

[63] J. Friedrichs, K. R. Legate, R. Schubert, M. Bharadwaj, C. Werner, D. J. Müller, and M. Benoit. A practical guide to quantify cell adhesion using single-cell force spectroscopy. *Methods*, 60(2):169–78, 2013.

[64] J. Galle, L. Preziosi, and A. Tosin. Contact inhibition of growth described using a multiphase model and an individual cell based model. *Applied Mathematics Letters*, 22(10):1483–1490, oct 2009.

[65] N. Gaspar et al. Acquired resistance to 17-allylamino-17-demethoxygeldanamycin (17-AAG, tanespimycin) in glioblastoma cells. *Cancer Research*, 69(5):1966–75, 2009.

[66] C. Giverso and L. Preziosi. Modelling the compression and reorganization of cell aggregates. *Mathematical Medicine and Biology*, 29(2):181–204, 2012.

[67] C. Giverso, M. Scianna, and A. Grillo. Growing avascular tumours as elasto-plastic bodies by the theory of evolving natural configurations. *Mechanics Research Communications*, 68:31–39, 2015.

[68] X. Gong, C. Lin, J. Cheng, J. Su, H. Zhao, T. Liu, X. Wen, and P. Zhao. Generation of multicellular tumor spheroids with microwell-based agarose scaffolds for drug testing. *Plos One*, 10(6):e0130348, 2015.

[69] T. T. Goodman, J. Chen, K. Matveev, and S. H. Pun. Spatio-temporal modeling of nanoparticle delivery to multicellular tumor spheroids. *Biotechnology and Bioengineering*, 101(2):388–399, 2008.

[70] R. Grantab, S. Sivananthan, and I. F. Tannock. The penetration of anticancer drugs through tumor tissue as a function of cellular adhesion and packing density of tumor cells. *Cancer Research*, 66(2):1033–9, 2006.

[71] W. G. Gray and C. T. Miller. Thermodynamically constrained averaging theory approach for modeling flow and transport phenomena in porous medium systems: 1. Motivation and overview. *Advances in Water Resources*, 28(2):161–180, 2005.

[72] W. G. Gray and C. T. Miller. *Introduction to the Thermodynamically Constrained Averaging Theory for Porous Medium Systems*. Advances in Geophysical and Environmental Mechanics and Mathematics. Springer International Publishing, 1 edition, 2014.

[73] H. P. Greenspan. Models for the growth of a solid tumor by diffusion. *Studies in Applied Mathematics*, 51(4):317–340, 1972.

[74] H. P. Greenspan. On the growth and stability of cell cultures and solid tumors. *Journal of Theoretical Biology*, 56(1):229–42, 1976.

[75] A. Grillo, R. Prohl, and G. Wittum. A generalised algorithm for anelastic processes in elastoplasticity and biomechanics. *Mathematics and Mechanics of Solids*, 2015, doi: 10.1177/1081286515598661.

[76] A. Grillo, R. Prohl, and G. Wittum. A poroplastic model of structural reorganisation in porous media of biomechanical interest. *Continuum Mechanics and Thermodynamics*, 28(1-2):579–601, 2016.

[77] D. A. Haber and V. E. Velculescu. Blood-based analyses of cancer: circulating tumor cells and circulating tumor DNA. *Cancer Discovery*, 4(6):650–61, 2014.

[78] S. I. Hajdu. A note from history: the first tumor pathologist. *Annals of clinical and laboratory science*, 34(3):355–6, 2004.

[79] D. Hanahan and R. A. Weinberg. The hallmarks of cancer. *Cell*, 100(1):57–70, 2000.

[80] D. Hanahan and R. A. Weinberg. Hallmarks of cancer: the next generation. *Cell*, 144(5):646–74, 2011.

[81] J. Helenius, C. Heisenberg, H. E. Gaub, and D. J. Muller. Single-cell force spectroscopy. *Journal of Cell Science*, 121(11):1785–91, 2008.

[82] E. Heller and E. Fuchs. Tissue patterning and cellular mechanics. *The Journal of Cell Biology*, 211(2):219–31, 2015.

[83] G. Helmlinger, P A Netti, H C Lichtenbeld, R J Melder, and R K Jain. Solid stress inhibits the growth of multicellular tumor spheroids. *Nature Biotechnology*, 15(8):778–83, 1997.

[84] L. Hengst, V. Dulic, J. M. Slingerland, E. Lees, and S. I. Reed. A cell cycle-regulated inhibitor of cyclin-dependent kinases. *Proceedings of the National Academy of Sciences*, 91(12):5291–5, 1994.

[85] M. H. Holmes and V. C. Mow. The nonlinear characteristics of soft gels and hydrated connective tissues in ultrafiltration. *Journal of Biomechanics*, 23(11):1145–56, 1990.

[86] S. S. Hossain, S. F. A. Hossainy, Y. Bazilevs, V. M. Calo, and T. J. R. Hughes. Mathematical modeling of coupled drug and drug-encapsulated nanoparticle transport in patient-specific coronary artery walls. *Computational Mechanics*, 49(2):213–242, 2012.

[87] J. D. Humphrey and K. R. Rajagopal. A constrained mixture model for growth and remodeling of soft tissues. *Mathematical Models and Methods in Applied Sciences*, 12(03):407–430, 2002.

[88] A. Iordan, A. Duperray, and C. Verdier. Fractal approach to the rheology of concentrated cell suspensions. *Physical Review E*, 77:011911, 2008.

[89] R. K. Jain. Determinants of tumor blood flow: a review. *Cancer Research*, 48(10):2641–58, 1988.

[90] R. K. Jain and L. T. Baxter. Mechanisms of heterogeneous distribution of monoclonal antibodies and other macromolecules in tumors: significance of elevated interstitial pressure. *Cancer Research*, 48(24 I):7022–7032, 1988.

[91] R. K. Jain, J. D. Martin, and T. Stylianopoulos. The role of mechanical forces in tumor growth and therapy. *Annual Review of Biomedical Engineering*, 16:321–46, 2014.

[92] R. K. Jain and T. Stylianopoulos. Delivering nanomedicine to solid tumors. *Nature Reviews. Clinical Oncology*, 7(11):653–64, 2010.

[93] L. J. Kaufman, C. P. Brangwynne, K. E. Kasza, E. Filippidi, V. D. Gordon, T. S. Deisboeck, and D. A. Weitz. Glioma expansion in collagen I matrices: analyzing collagen concentration-dependent growth and motility patterns. *Biophysical Journal*, 89(1):635–650, 2005.

[94] D. J. Kelly and P. J. Prendergast. Mechano-regulation of stem cell differentiation and tissue regeneration in osteochondral defects. *Journal of Biomechanics*, 38(7):1413–22, 2005.

[95] M. Kim, R. J. Gillies, and K. A. Rejniak. Current advances in mathematical modeling of anti-cancer drug penetration into tumor tissues. *Frontiers in Oncology*, 3(November):278, 2013.

[96] T. Kim, C. W. Mount, W. R. Gombotz, and S. H. Pun. The delivery of doxorubicin to 3-D multicellular spheroids and tumors in a murine xenograft model using tumor-penetrating triblock polymeric micelles. *Biomaterials*, 31(28):7386–97, 2010.

[97] Y. Kim, M. A. Stolarska, and H. G. Othmer. A hybrid model for tumor spheroid growth in vitro i: theoretical development and early results. *Mathematical Models and Methods in Applied Sciences*, 17(supp01):1773–1798, 2007.

[98] Y. Kim, M. A. Stolarska, and H. G. Othmer. The role of the microenvironment in tumor growth and invasion. *Progress in Biophysics and Molecular Biology*, 106(2):353–79, 2011.

[99] J. P. Kirkpatrick and L. B. Marks. Modeling killing and repopulation kinetics of subclinical cancer: direct calculations from clinical data. *International Journal of Radiation Oncology*Biology*Physics*, 58(2):641 – 654, 2004.

[100] M. Knowles and P. Selby. *Introduction to the Cellular and Molecular Biology of Cancer*. Oxford bioscience. OUP Oxford, 2005.

[101] A. G. Knudson. Mutation and cancer: statistical study of retinoblastoma. *Proceedings of the National Academy of Sciences of the United States of America*, 68(4):820–823, 1971.

[102] P. Koumoutsakos, I. Pivkin, and F. Milde. The fluid mechanics of cancer and its therapy. *Annual Review of Fluid Mechanics*, 45(1):325–355, 2013.

[103] E. Kröner. Allgemeine Kontinuumstheorie der Versetzungen und Eigenspannungen. *Archive for Rational Mechanics and Analysis*, 4:273, 1959.

[104] L. A. Kunz-Schughart, M. Kreutz, and R. Knuechel. Multicellular spheroids: a three-dimensional in vitro culture system to study tumour biology. *International Journal of Experimental Pathology*, 79(1):1–23, 1998.

[105] D. Lacroix and P. J. Prendergast. A mechano-regulation model for tissue differentiation during fracture healing: analysis of gap size and loading. *Journal of Biomechanics*, 35(9):1163–71, 2002.

[106] K. Leder, K. Pitter, Q. Laplant, D. Hambardzumyan, B. D. Ross, T. A. Chan, E. C. Holland, and F. Michor. Mathematical modeling of PDGF-driven glioblastoma reveals optimized radiation dosing schedules. *Cell*, 156(3):603–16, 2014.

[107] D. A. Lee, M. M. Knight, J. J. Campbell, and D. L. Bader. Stem cell mechanobiology. *Journal of Cellular Biochemistry*, 112(1):1–9, 2011.

[108] E. H. Lee. Elastic-plastic deformation at finite strains. *ASME Journal of Applied Mechanics*, 36:1–6, 1969.

[109] H. A. Levine, B. D. Sleeman, and M. Nilsen-Hamilton. A mathematical model for the roles of pericytes and macrophages in the initiation of angiogenesis. I. The role of protease inhibitors in preventing angiogenesis. *Mathematical Biosciences*, 168(1):77–115, 2000.

[110] H. A. Levine, A. L. Tucker, and M. Nilsen-Hamilton. A Mathematical Model for the Role of Cell Signal Transduction in the Initiation and Inhibition of Angiogenesis. *Growth Factors*, 20(4):155–175, 2003.

[111] R. W. Lewis and B. A. Schrefler. *The Finite Element Method in the Static and Dynamic Deformation and Consolidation of Porous Media*. Numerical methods in engineering. John Wiley, 1998.

[112] D. Loessner, J. A. Flegg, H. M. Byrne, J. A. Clements, and D. W. Hutmacher. Growth of confined cancer spheroids: a combined experimental and mathematical modelling approach. *Integrative Biology*, 5(3):597, 2013.

[113] D. Longo, A. Fauci, D. Kasper, S. Hauser, J. Jameson, and J. Loscalzo. *Harrison's Principles of Internal Medicine, 18th Edition*. McGraw-Hill Education, 2011.

[114] J. S. Lowengrub, H. B. Frieboes, F. Jin, Y-L. Chuang, X. Li, P. Macklin, S. M. Wise, and V. Cristini. Nonlinear modelling of cancer: bridging the gap between cells and tumours. *Nonlinearity*, 23(1):R1–R9, 2010.

[115] C. K. Luk, L. Veinot-Drebot, E. Tjan, and I. F. Tannock. Effect of transient hypoxia on sensitivity to doxorubicin in human and murine cell lines. *Journal of the National Cancer Institute*, 82(8):684–92, 1990.

[116] P. Macklin. *Toward Computational Oncology: Nonlinear Simulation of Centimeter-Scale Tumor Growth in Complex, Heterogeneous Tissues*. Ph.D. dissertation, University of California, Irvine Department of Mathematics, June 2007.

[117] S. Majid Hassanizadeh. Derivation of basic equations of mass transport in porous media, Part 2. Generalized Darcy's and Fick's laws. *Advances in Water Resources*, 9(4):207–222, 1986.

[118] A. B. Mariotto, R. K. Yabroff, Y. Shao, E. J. Feuer, and M. L. Brown. Projections of the cost of cancer care in the united states: 20102020. *Journal of the National Cancer Institute*, 103(2):117–128, 2011.

[119] P. Marmottant et al. The role of fluctuations and stress on the effective viscosity of cell aggregates. *Proceedings of the National Academy of Sciences*, 106(41):17271–17275, 2009.

[120] P. Mascheroni, C. Stigliano, M. Carfagna, D. P. Boso, L. Preziosi, P. Decuzzi, and B. A. Schrefler. Predicting the growth of glioblastoma multiforme spheroids using a multiphase porous media model. *Biomechanics and Modeling in Mechanobiology*, 15(5):1215–28, 2016.

[121] G. A. Maugin and M. Epstein. Geometrical material structure of elastoplasticity. *International Journal of Plasticity*, 14(1-3):109–115, 1998.

[122] H. McAneney and O'Rourke S. F. C. Investigation of various growth mechanisms of solid tumour growth within the linear-quadratic model for radiotherapy. *Physics in Medicine and Biology*, 52(4):1039, 2007.

[123] S. R. McDougall, A. R. A. Anderson, and M. A. J. Chaplain. Mathematical modelling of dynamic adaptive tumour-induced angiogenesis: clinical implications and therapeutic targeting strategies. *Journal of Theoretical Biology*, 241(3):564–89, 2006.

[124] F. Michor and K. Beal. Improving cancer treatment via mathematical modeling: surmounting the challenges is worth the effort. *Cell*, 163(5):1059–1063, 2015.

[125] F. Michor, J. Liphardt, M. Ferrari, and J. Widom. What does physics have to do with cancer? *Nature reviews. Cancer*, 11(9):657–70, 2011.

[126] M. V. Mićunović. *Thermomechanics of Viscoplasticity Fundamentals and Applications*. Springer-Verlag New York, 2009.

[127] A. S. Mikhail, S. Eetezadi, and C. Allen. Multicellular tumor spheroids for evaluation of cytotoxicity and tumor growth inhibitory effects of nanomedicines in vitro: a comparison of docetaxel-loaded block copolymer micelles and Taxotere®. *PloS one*, 8(4):e62630, 2013.

[128] F. Montel, M. Delarue, J. Elgeti, L. Malaquin, M. Basan, T. Risler, B. Cabane, D. Vignjevic, J. Prost, G. Cappello, and J. Joanny. Stress clamp experiments on multicellular tumor spheroids. *Physical Review Letters*, 107(18):188102, 2011.

[129] F. Montel, M. Delarue, J. Elgeti, D. Vignjevic, G. Cappello, and J. Prost. Isotropic stress reduces cell proliferation in tumor spheroids. *New Journal of Physics*, 14(5):055008, 2012.

[130] J. Moreira and A. Deutsch. Cellular automaton models of tumor development: a critical review. *Advances in Complex Systems*, 5(02n03):247–267, 2002.

[131] F. Mpekris, S. Angeli, A. P. Pirentis, and T. Stylianopoulos. Stress-mediated progression of solid tumors: effect of mechanical stress on tissue oxygenation, cancer cell proliferation, and drug delivery. *Biomechanics and Modeling in Mechanobiology*, 14(6):1391–402, 2015.

[132] W. Mueller-Klieser. Tumor biology and experimental therapeutics. *Critical Reviews in Oncology/Hematology*, 36(2-3):123–39, 2000.

[133] W. Mueller-Klieser, J. P. Freyer, and R. M. Sutherland. Influence of glucose and oxygen supply conditions on the oxygenation of multicellular spheroids. *British Journal of Cancer*, 53(3):345–53, 1986.

[134] W. F. Mueller-Klieser and R. M. Sutherland. Oxygen tensions in multicell spheroids of two cell lines. *British Journal of Cancer*, 45(2):256–64, 1982.

[135] C. M. Nelson and M. J. Bissel. Of extracellular matrix, scaffolds, and signaling: tissue architecture regulates development, homeostasis, and cancer. *Annual Review of Cell and Developmental Biology*, 22(1):287–309, 2006.

[136] P. A. Netti, D. A. Berk, M. A. Swartz, A. J. Grodzinsky, and R. K. Jain. Role of extracellular matrix assembly in interstitial transport in solid tumors. *Cancer Research*, 60(9):2497–503, 2000.

[137] L. Norton and R. Simon. Growth curve of an experimental solid tumor following radiotherapy. *Journal of the National Cancer Institute*, 58(6):1735–41, 1977.

[138] M. E. Orme and M. A. J. Chaplain. Two-dimensional models of tumour angjogenesis and anti-angiogenesis strategies. *IMA Journal of Mathematics Applied in Medicine & Biology*, 14(3):189–205, 1997.

[139] S. Paget. The distribution of secondary growths in cancer of the breast. *The Lancet*, 133(3421):571 – 573, 1889.

[140] J. Panovska, H. M. Byrne, and P. K. Maini. A theoretical study of the response of vascular tumours to different types of chemotherapy. *Mathematical and Computer Modelling*, 47(5-6):560–579, 2008.

[141] K. Park. Facing the truth about nanotechnology in drug delivery. *ACS Nano*, 7(9):7442–7447, 2013.

[142] H. Peinado, S. Lavotshkin, and D. Lyden. The secreted factors responsible for pre-metastatic niche formation: old sayings and new thoughts. *Seminars in Cancer Biology*, 21(2):139–46, 2011.

[143] G. F. Pinder and W. G. Gray. *Essentials of Multiphase Flow in Porous Media*. Wiley, 2008.

[144] M. D. Planas-Silva and R. A. Weinberg. The restriction point and control of cell proliferation. *Current Opinion in Cell Biology*, 9(6):768–72, 1997.

[145] K. Polyak, J. Y. Kato, M. J. Solomon, C. J. Sherr, J. Massague, J. M. Roberts, and A. Koff. p27Kip1, a cyclin-Cdk inhibitor, links transforming growth factor-beta and contact inhibition to cell cycle arrest. *Genes & development*, 8(1):9–22, 1994.

[146] L. Preziosi. *Cancer Modelling and Simulation*. Chapman & Hall/CRC Mathematical and Computational Biology. CRC Press, 2003.

[147] L. Preziosi, D. Ambrosi, and C. Verdier. An elasto-visco-plastic model of cell aggregates. *Journal of Theoretical Biology*, 262(1):35–47, 2010.

[148] L. Preziosi and A. Tosin. Multiphase and multiscale trends in cancer modelling. *Mathematical Modelling of Natural Phenomena*, 4(3):1–11, 2009.

[149] L. Preziosi and A. Tosin. Multiphase modelling of tumour growth and extracellular matrix interaction: mathematical tools and applications. *Journal of Mathematical Biology*, 58(4-5):625–56, 2009.

[150] L. Preziosi and G. Vitale. A multiphase model of tumor and tissue growth including cell adhesion and plastic reorganization. *Mathematical Models and Methods in Applied Sciences*, 21(09):1901–1932, 2011.

[151] P. Puech, A. Taubenberger, F. Ulrich, M. Krieg, D. J. Muller, and C. Heisenberg. Measuring cell adhesion forces of primary gastrulating cells from zebrafish using atomic force microscopy. *Journal of Cell Science*, 118(Pt 18):4199–206, 2005.

[152] V. Quaranta, K. A. Rejniak, P. Gerlee, and A. R. A. Anderson. Invasion emerges from cancer cell adaptation to competitive microenvironments: quantitative predictions from multiscale mathematical models. *Seminars in Cancer Biology*, 18:338–348, 2008.

[153] V. Quaranta, A. M. Weaver, P. T. Cummings, and A. R. A. Anderson. Mathematical modeling of cancer: the future of prognosis and treatment. *Clinica Chimica Acta*, 357(2):173–9, 2005.

[154] S. Retsas. *Palaeo-oncology: The Antiquity of Cancer*. Farrand, 1986.

[155] T. Risler. Focus on the physics of cancer. *New Journal of Physics*, 17(5):055011, 2015.

[156] R. Rockne, E. C. Alvord, J. K. Rockhill, and K. R. Swanson. A mathematical model for brain tumor response to radiation therapy. *Journal of Mathematical Biology*, 58(4):561–578, 2008.

[157] E. K. Rodriguez, A. Hoger, and A. D. McCulloch. Stress-dependent finite growth in soft elastic tissues. *Journal of Biomechanics*, 27(4):455–67, 1994.

[158] T. Roose, S. J. Chapman, and P. K. Maini. Mathematical models of avascular tumor growth. *SIAM Review*, 49(2):179–208, 2007.

[159] T. Roose, P. A. Netti, L. L. Munn, Y. Boucher, and R. K. Jain. Solid stress generated by spheroid growth estimated using a linear poroelasticity model. *Microvascular Research*, 66(3):204–12, 2003.

[160] R. Santagiuliana, M. Ferrari, and B. A. Schrefler. Simulation of angiogenesis in a multiphase tumor growth model. *Computer Methods in Applied Mechanics and Engineering*, 304:197–216, 2016.

[161] M. Sarntinoranont, F. Rooney, and M. Ferrari. Interstitial stress and fluid pressure within a growing tumor. *Annals of Biomedical Engineering*, 31(3):327–35, 2003.

[162] M. Scianna, C. G. Bell, and L. Preziosi. A review of mathematical models for the formation of vascular networks. *Journal of Theoretical Biology*, 333:174–209, 2013.

[163] G. Sciumè, D. P. Boso, W. G. Gray, C. Cobelli, and B. A. Schrefler. A two-phase model of plantar tissue: a step toward prediction of diabetic foot ulceration. *International Journal for Numerical Methods in Biomedical Engineering*, 30(11):1153–1169, 2014.

[164] G. Sciumè, W. G. Gray, M. Ferrari, P. Decuzzi, and B. A. Schrefler. On computational modeling in tumor growth. *Archives of Computational Methods in Engineering*, 20(4):327–352, 2013.

[165] G. Sciumè, W. G. Gray, F. Hussain, M. Ferrari, P. Decuzzi, and B. A. Schrefler. Three phase flow dynamics in tumor growth. *Computational Mechanics*, 53(3):465–484, 2013.

[166] G. Sciumè, R. Santagiuliana, M. Ferrari, P. Decuzzi, and B. A. Schrefler. A tumor growth model with deformable ECM. *Physical Biology*, 11(6):65004, 2014.

[167] G. Sciumè, S. Shelton, W. G. Gray, C. T. Miller, F. Hussain, M. Ferrari, P. Decuzzi, and B. A. Schrefler. A multiphase model for three-dimensional tumor growth. *New Journal of Physics*, 15(1):015005, 2013.

[168] N. A. Seebacher, D. R. Richardson, and P. J. Jansson. Glucose modulation induces reactive oxygen species and increases P-glycoprotein-mediated multidrug resistance to chemotherapeutics. *British Journal of Pharmacology*, 172(10):2557–2572, 2015.

[169] J. C. Simo and T. J. R. Hughes. *Computational Inelasticity*. Interdisciplinary Applied Mathematics. Springer-Verlag New York, 1998.

[170] R. Skalak. Growth as a finite displacement field. In *Proceedings of the IUTAM Symposium on Finite Elasticity*, pages 347–355. Springer Netherlands, 1981.

[171] B. St Croix, V. A. Flørenes, J. W. Rak, M. Flanagan, N. Bhattacharya, J. M. Slingerland, and R. S. Kerbel. Impact of the cyclin-dependent kinase inhibitor p27Kip1 on resistance of tumor cells to anticancer agents. *Nature Medicine*, 2(11):1204–10, 1996.

[172] B. St Croix, C. Sheehan, J. W. Rak, V. A. Flørenes, J. M. Slingerland, and R. S. Kerbel. E-Cadherin-dependent growth suppression is mediated by the cyclin-dependent kinase inhibitor p27(KIP1). *The Journal of Cell Biology*, 142(2):557–71, 1998.

[173] Bernard Stewart and Christopher P. Wild, editors. *World Cancer Report 2014*. International Agency for Research on Cancer, WHO, 2014.

[174] T. Stiehl, N. Baran, A. D. Ho, and A. Marciniak-Czochra. Cell division patterns in acute myeloid leukemia stem-like cells determine clinical course: a model to predict patient survival. *Cancer Research*, 75(6):940–949, 2015.

[175] C. Stigliano, J. Key, M. Ramirez, S. Aryal, and P. Decuzzi. Radiolabeled polymeric nanoconstructs loaded with docetaxel and curcumin for cancer combinatorial therapy and nuclear imaging. *Advanced Functional Materials*, 25(22):3371–3379, 2015.

[176] C. L. Stokes and D. A. Lauffenburger. Analysis of the roles of microvessel endothelial cell random motility and chemotaxis in angiogenesis. *Journal of Theoretical Biology*, 152(3):377 – 403, 1991.

[177] T. Stylianopoulos et al. Causes, consequences, and remedies for growth-induced solid stress in murine and human tumors. *Proceedings of the National Academy of Sciences*, 109(38):15101–15108, 2012.

[178] T. Stylianopoulos, J. D. Martin, M. Snuderl, F. Mpekris, S. R. Jain, and R. K. Jain. Coevolution of solid stress and interstitial fluid pressure in tumors during progression: implications for vascular collapse. *Cancer Research*, 73(13):3833–41, 2013.

[179] R. Sutherland, J. Carlsson, R. Durand, and J. Yuhas. Spheroids in Cancer Research. *Cancer Research*, 41(July):2980–2984, 1981.

[180] R. M. Sutherland. Cell and environment interactions in tumor microregions: the multicell spheroid model. *Science*, 240(4849):177–84, 1988.

[181] R. M. Sutherland, J. A. McCredie, and W. R. Inch. Growth of multicell spheroids in tissue culture as a model of nodular carcinomas. *Journal of the National Cancer Institute*, 46(1):113–20, 1971.

[182] A. Szabó and R. M. H. Merks. Cellular potts modeling of tumor growth, tumor invasion, and tumor evolution. *Frontiers in Oncology*, 3(87):1–12, 2013.

[183] L. A. Taber. Biomechanics of growth, remodeling, and morphogenesis. *Applied Mechanics Reviews*, 48(8):487, 1995.

[184] O. Trédan, C. M. Galmarini, K. Patel, and I. F. Tannock. Drug resistance and the solid tumor microenvironment. *Journal of the National Cancer Institute*, 99(19):1441–54, 2007.

[185] M. Vinci, S. Gowan, F. Boxall, L. Patterson, M. Zimmermann, W. Court, C. Lomas, M. Mendiola, D. Hardisson, and S. A. Eccles. Advances in establishment and analysis of three-dimensional tumor spheroid-based functional assays for target validation and drug evaluation. *BMC biology*, 10(1):29, 2012.

[186] C. Voutouri, F. Mpekris, P. Papageorgis, A. D. Odysseos, and T. Stylianopoulos. Role of constitutive behavior and tumor-host mechanical interactions in the state of stress and growth of solid tumors. *PloS One*, 9(8):e104717, 2014.

[187] X. Wang, X. Zhen, J. Wang, J. Zhang, W. Wu, and X. Jiang. Doxorubicin delivery to 3D multicellular spheroids and tumors based on boronic acid-rich chitosan nanoparticles. *Biomaterials*, 34(19):4667–79, 2013.

[188] O. Warburg, K. Posener, and E. Negelein. Über den stoffwechsel der tumoren. *Biochemische Zeitschrift*, 152:319–344, 1924.

[189] J. P. Ward and J. R. King. Mathematical modelling of avascular-tumour growth. *IMA Journal of Mathematics Applied in Medicine and Biology*, 14(1):39–69, 1997.

[190] J. P. Ward and J. R. King. Mathematical modelling of drug transport in tumour multicell spheroids and monolayer cultures. *Mathematical Biosciences*, 181(2):177–207, 2003.

[191] B. D. Weinberg, R. B. Patel, A. A. Exner, G. M. Saidel, and J. Gao. Modeling doxorubicin transport to improve intratumoral drug delivery to RF ablated tumors. *Journal of Controlled Release*, 124(1-2):11–9, 2007.

[192] R. A. Weinberg. *The Biology of Cancer*. Taylor & Francis Group, 2014.

[193] T. E. Wheldon, J. Kirk, and J. S. Orr. Optimal radiotherapy of tumour cells following exponential-quadratic survival curves and exponential repopulation kinetics. *The British Journal of Radiology*, 50(597):681–682, 1977.

[194] W. R. Wilson and M. P. Hay. Targeting hypoxia in cancer therapy. *Nature Reviews. Cancer*, 11(6):393–410, 2011.

[195] S. M. Wise, J. S. Lowengrub, H. B. Frieboes, and V. Cristini. Three-dimensional multispecies nonlinear tumor growth - I Model and numerical method. *Journal of Theoretical Biology*, 253(3):524–43, 2008.

[196] B. G. Wouters and J. M. Brown. Cells at intermediate oxygen levels can be more important than the "hypoxic fraction" in determining tumor response to fractionated radiotherapy. *Radiation Research*, 147(5):541–550, 1997.

[197] H. Xing et al. Effect of the cyclin-dependent kinases inhibitor p27 on resistance of ovarian cancer multicellular spheroids to anticancer chemotherapy. *Journal of Cancer Research and Clinical Oncology*, 131(8):511–519, 2005.

[198] H. Zahreddine and K. L. B. Borden. Mechanisms and insights into drug resistance in cancer. *Frontiers in Pharmacology*, 4:28, 2013.

Acknowledgements

Desidero ricordare tutti coloro che mi hanno aiutato nella stesura della tesi con suggerimenti, critiche ed osservazioni: a loro va la mia gratitudine.

Ringrazio anzitutto la professoressa Daniela Boso e il professor Bernhard Schrefler, entrambi miei relatori: senza il loro supporto e la loro guida questa tesi non esisterebbe.

Proseguo con i valutatori esterni, la professoressa Anna Pandolfi e il professor Davide Ambrosi. Li ringrazio per i loro commenti e le loro correzioni.

Un ringraziamento particolare va ai professori e ai colleghi con cui ho collaborato nel corso del lavoro. In particolare, ringrazio i professori Paolo Decuzzi, Luigi Preziosi e Alfio Grillo e le dottoresse Cinzia Stigliano e Melania Carfagna.

Desidero ringraziare i colleghi e gli amici del dipartimento, in particolare il dottor Mattia Pizzocaro, per il loro supporto e i continui confronti sulla tesi.

Vorrei infine ringraziare le persone a me più care: i miei amici, la mia fidanzata e la mia famiglia.